Biologically inspired glass/polyepoxide interphase with improved mechanical properties

DISSERTATION

Zur Erlangung des akademischen Grades des Doktors der Naturwissenschaften (Dr. rer. nat.)

Eingereicht im Fachbereich Biologie, Chemie, Pharmazie

der Freien Universität Berlin

vorgelegt von

M.Sc. Sebastian Czarnecki

aus Berlin

Die vorliegende Doktorarbeit wurde im Zeitraum vom 01.03.2016 bis 31.07.2019 an der Bundesanstalt für Materialforschung und -prüfung (BAM) in der Abteilung 6.6 Nanotribologie und Nanostrukturierung von Oberflächen unter der Anleitung von Dr. Annabelle Bertin, Univ.-Prof. Dr. Heinz Sturm und Univ.-Prof. Dr. Rainer Haag angefertigt.

1. Gutachter:	Univ.-Prof. Dr. Heinz Sturm
2. Gutachter:	Univ.-Prof. Dr. Rainer Haag
Disputation am	11.11.2019

Acknowledgements

First and foremost, I would like to thank Univ.-Prof. Dr. Heinz Sturm and Univ.-Prof. Dr. Rainer Haag for their scientific support during my doctoral thesis. Moreover, I would like to thank all members of the department 6 for their great support and fruitful discussions over the last three years.

I thank Dr. Annabelle Bertin for introducing me into the field of hybrid inorganic/organic materials and their applications in material science.

Particularly, I would like to thank Dr. Korinna Altmann (BAM 6.6) for introducing me into the IRRAS technique and for XPS measurements (BAM 6.6). I thank Mario Sahre (BAM 6.7) and Dr. Dorothee Silbernagl (BAM 6.6) for AFM measurements, Gundula Hidde (BAM 6.7) for contact angle measurements as well as Dr. Gerhard Kalinka (BAM 5.3) and Lothar Buchta (BAM 5.3) for introducing me in the Zwick 1454 tensile testing machine. Special thanks go to Marlies Gräwert (MPIKG) and the NMR Core Facility at the FU Berlin for the innumerous number of measured GPC and NMR samples.

Furthemore, I would like to thank Dr. Theoni K. Georgiou for the research stay at the Imperial College in London. It was a great pleasure for me to meet you and your group.

I would like to thank Dr. Ievgeniia Topolniak and Dr. Torsten Rossow for proof-reading my doctoral thesis.

In addition, I would like to acknowledge my undergraduate and graduate students who were working under my supervision, namely: B.Sc. Jan Potthoff, B.Sc. Thi Mai Phuong Tran and M.Sc. Daniel Braatz.

Lastly, I thank my parents Elzbieta Czarnecki and Tadeusz Czeslaw Czarnecki, my brothers Maciej Czarnecki and Przemyslaw Czarnecki as well as my girlfriend Sina-Vanessa and my son Julius Frederik for their boundless support and faith in my person.

Contents

List of abbreviations and symbols

δ	Chemical shift
τ_{max}	Interfacial tensile strength
Γ	Surface coverage
σ	Grafting density
σ_s	Surface free energy
AcOH	Acetic acid
AFM	Atomic force microscopy
ATRP	Atom transfer radical polymerization
b	Block
BCP	Block copolymer
CDPB	2-Cyano-2-propyl benzodithioate
CDTSPA	4-Cyano-4-[(dodecylsulfanylthiocarbonyl)sulfanyl]pentanoic acid
CLRP	Controlled living radical polymerization
CTA	Chain transfer agent
$[CTA]_0$	Initial chain transfer agent concentration
DCM	Dichlormethane
DHP	3,4-Dihydropyran
DSC	Differential scanning calorimetry
Đ	Dispersity
DP	Degree of polymerization
GCP	Gradient copolymer
g	Gram
grad	Gradient
GPC	Gel permeation chromatography
HEMA	2-hydroxyethyl methacrylate
IPSMA	3-(triisopropoxysilyl)propyl methacrylate
IR-ATR	Infrared attentuated total reflection spectrosopy
IRRAS	Infrared adsorption reflection spectroscopy
mg	Miligram
mL	Mililiter
MMA	Methyl methacrylate
mmol	Milimol

mol	Mol
MWD	Molecular weight distribution
M_w	Weight-average molecular weight
M_n	Number-average molecular weight
M_z	Z-average molecular weight
$[M]_0$	Initial monomer concentration
NMP	Nitroxide-mediated radical polymerization
NMR	Nuclear magnetic resonance
P	Homopolymer
PMMA	Poly(methyl methacrylate)
PPTS	Pyridinium *p*-toluenesulfonate
PTSA	*p*-Toluenesulfonic acid
RAFT	Reversible addition-fragmentation chain transfer
SCP	Statistical copolymer
stat	Statistical
TESPMA	3-(triethoxysilyl)propyl methacrylate
TGA	Thermogravimetric analysis
THP-HEMA	2-((tetrahydro-2H-pyran-2-yl)oxy)ethyl methacrylate
THF	Tetrahydrofurane
TMSPMA	3-(trimethoxysilyl)propyl methacrylate
XPS	X-ray photoelectron spectroscopy

1 Introduction

Monolithic materials such as metals, ceramic materials or polymeric materials have been used since the beginning of human civilization, due to their wide range of application and simple fabrication. Nevertheless, since the industrial revolution great efforts have been made in the development of new techniques to process and fabricate materials. These new techniques allowed the preparation of materials that consist of a reinforcement, which is embedded in or bonded to a matrix at a macro- and microscopic level with distinct interfaces or boundaries between them. Such materials are termed as composites and have been used in the field of engineering and technology over a broad range of applications such as aeronautical, automotive, aircraft appliances or sports equipment such as shoes, rackets and golf clubs.[1-4]

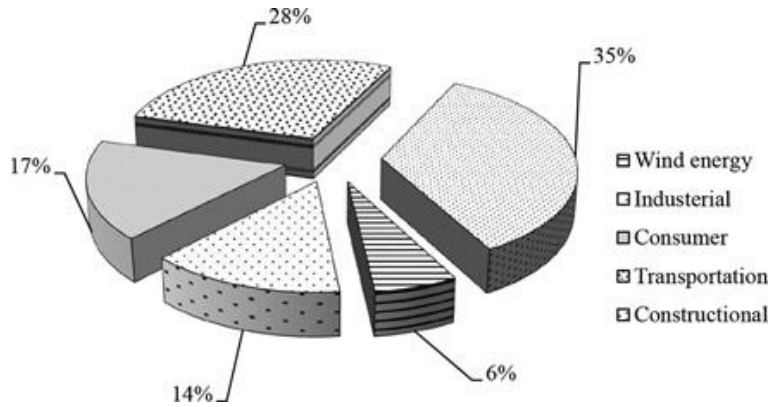

Figure 1. Market percentage of glass fiber composites in different applications. Reprinted with permission from ref. [1]. Copyright © 2017 Taylor & Francis.

Composites combine the material properties of both the reinforcement (e.g. glass-fiber, carbon-fiber, Kenaf fiber) and the matrix (e.g. polyester, polyepoxide, polyurethane) to optimize and improve the overall material properties due to synergistic effects. In addition, glass-fiber composites aroused great attention in the last decades in various fields, as displayed in Figure 1, because of their superior mechanical properties. The mechanical properties of glass fiber composites are mainly governed by three facts: I) Intrinsic mechanical properties of the glass-fiber and polymer matrix. II) Dispersion of the glass-fiber within the polymeric matrix. III) Interfacial adhesion between the glass-fiber and polymer matrix. A lack of strong interfacial adhesion between the glass-fiber and polymer matrix can tremendously compromise the reinforcement effect of the glass fiber. Due to this fact, a strong interfacial adhesion between glass-fiber and polymer matrix is crucial to afford a composite material with superior mechanical properties. [5] To maximize

interfacial interactions between glass fibers and matrix it is important to consider the chemical nature of the glass fiber surface as well as the chemical nature of the used polymer matrix. Thus, the surface of the glass fiber must be modified in respect to the used polymer matrix. A commonly employed technique to enhance the interfacial adhesion and compatibility of the constituent materials are glass fiber surface modifications by using coatings. [6, 7] Typically, such surface modifications are accomplished by using low molecular weight silane coupling agents (silylation), in which the polar functionalities of the coupling agent act as “molecular bridges” at the interface between reinforcement and polymer matrix. [8] A more sophisticated approach employs polymeric precursors as adhesives, which enables the preparation of more complex interphase microstructures such as gradient microstructures. Feller *et. al.* [9] used silane modified polypropylene (PP) copolymers as polymeric adhesives in order to improve the mechanical properties of glass fiber/PP composite materials, due to chemical attachment of the silane functionalities to the glass fibers and interpenetration of the dangling PP chains into the PP matrix. In contrast to Feller’s approach, Trey and co-workers [10] employed thiol-ene “click” chemistry to develop a novel UV-curable thermoset matrix. Similar to this, Kuttner *et. al.* [11] developed a UV-light induced photopolymerization by using sulfhydrated glass fibers and subsequent surface-induced photopolymerization of vinyl-based monomers. This approach was further extended to the fabrication diblock copolymers on the glass fiber surfaces, giving rise to more complex interphase architectures. [12] According to the investigations of Kuttner and co-workers, the interfacial adhesion was mainly governed by the chain density of the grafted copolymers at the glass fiber/polyepoxide interface/interphase. Oréfice *et. al.* [13] demonstrated that chemically grafted hyperbranched polymer-siloxane structures can greatly improve the interfacial toughness of glass/polymer composites. In general, the interfacial toughening is achieved by a sufficient stress transfer from the polymer matrix to the fiber. For this reason, a rather “soft” interphase is desirable in order to ensure an efficient stress transfer.

1.1 Biologically inspired composite materials

Glass fiber composite materials are characterized by a high stiffness and high strength with the downsides having rather poor fracture and low impact energy absorption characteristics. Due to these downsides, the utilization of glass fiber composites in such applications, which require these material characteristics, are rather limited. Many materials that can be found in nature are composite materials. These naturally occurring composite materials are characterized a high stiffness and high strength without having

the same downsides as glass fiber-based composites. Natural fiber composites such as antler or bone show high toughness due to a unique interface design, fiber orientation pattern as well as hierarchal structuring. [14-16] Another fiber composite material encountered in nature are plant cell walls, in which stiff millimeter wide cellulose fibers are embedded in a soft polymer matrix. [17-19] The mechanical performance of plant cell walls is greatly affected by the design of the cellulose/polymer matrix interphase. [20] Herein, the structural composition of the glass/polymer matrix interphase is inspired by the tendon-to-bone insertion site. The tendon-to-bone insertion site connects two highly ordered hierarchical tissues with different biomechanical properties through a millimeter-wide area (insertion). The macroscopic morphology and microscopic composition of the tendon-to-bone insertion site are illustrated in Figure 2.

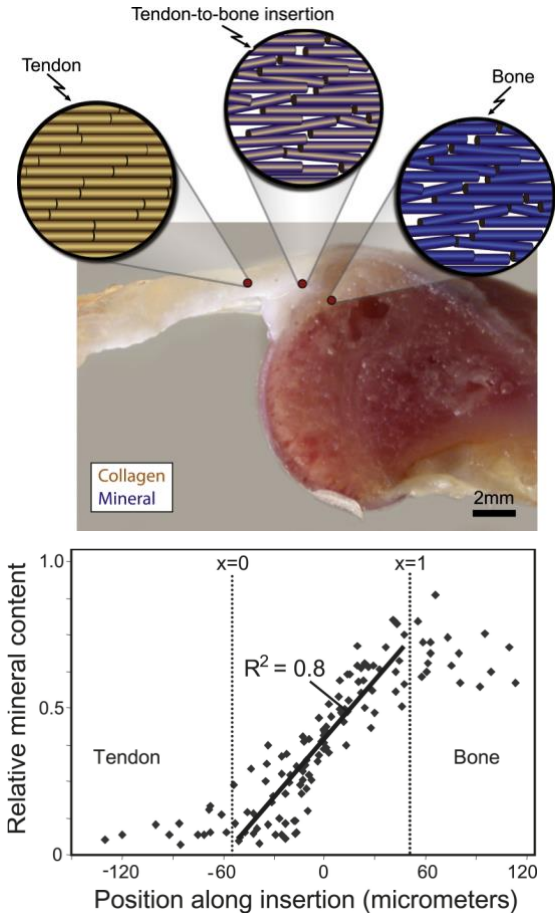

Figure 2. Morphology of the tendon-to-bone insertion as well as schematic representation of the microscopic structure of “soft” tissue (collagen), “hard” tissue (bone) and the tendon-to-bone insertion (top). Relative concentration of mineral along the tendon-to-bone insertion site (bottom). Reprnted with permission from ref. [21]. Copyright © 2009 Elsevier.

The linear gradual composition of the interphase between the tendon and the bone results in changes in the mechanical properties along the insertion site. This design principle of connecting a “soft” tissue (tendon) with a “hard” tissue (bone) via a graded functional area results in a minimized stress concentration along the insertion site and effective dissipation of mechanical stress. [21-23] To mimic the tendon-to-bone insertion site so-called hybrid inorganic/organic copolymers with a gradient-like composition are employed. Hybrid inorganic/organic gradient copolymers are composed of "hard" inorganic segments and "soft" organic segments similar to the composition of the tendon-to-bone insertion site with "hard" bone tissue segments and "soft" tendon tissue segments. These hybrid inorganic/organic copolymers with gradient-like composition are chemically attached to the glass surface as well as polymer matrix and thus, increase the interfacial adhesion between the glass-fiber and polymer matrix. The gradient-like composition mimics the gradual composition of the bone-tendon interphase, owing to minimize the stress concentration at the glass-fiber polymer matrix interphase. Due to previously published reports, in which the introduction of a polymer-based interphase results in an increase of the interfacial adhesion between both phases, it is believed to afford glass fiber composite materials with improved mechanical properties.

1.2 Hybrid inorganic/organic copolymers as precursors for functional materials

Hybrid inorganic/organic materials attracted considerable attention since the last century, due to their versatility and their potential application in the field of biomedicine and material science. [22, 23] One the most commonly used hybrid inorganic/organic materials are silicon-based materials. These materials are composed of inorganic silicon-based precursors such as tetraethyl orthosilicate (TEOS) or acrylic derivatives from this species and organic precursors such as 2-hydroxyethyl methacrylate (HEMA). Due to the advances in polymer synthesis, so-called hybrid silicon-based inorganic/organic copolymers with sol-gel active Si–OR moieties and well-defined microstructures have become promising polymeric precursors for functional hybrid materials. These hybrid inorganic/organic copolymers are composed of inorganic silicon-based (meth)acrylic or (meth)acrylamidic monomers with gelable Si–OR moieties such as 3-(trimethoxysilyl)propyl methacrylate (TMSPMA) and organic functional monomers such as stearyl methacrylate (SMA) or *N*-isopropylacrylamide (NIPAM), as illustrated in Figure 3. Since the arising of hybrid silicon-based inorganic/organic copolymers with sol-gel active

Si-OR, tremendous efforts were made to synthesize such copolymers with block and statistical microstructures in order to afford chemical and mechanical stable (nano)objects, (nano)materials and coatings with tailor-made properties and characteristics. [24, 25] The materials characteristics and properties are mainly governed by three factors: I) The chemical nature of both the inorganic and organic monomer. II) The chemical composition of the precursor polymer (e.g. block, gradient). III) The precursor processing.

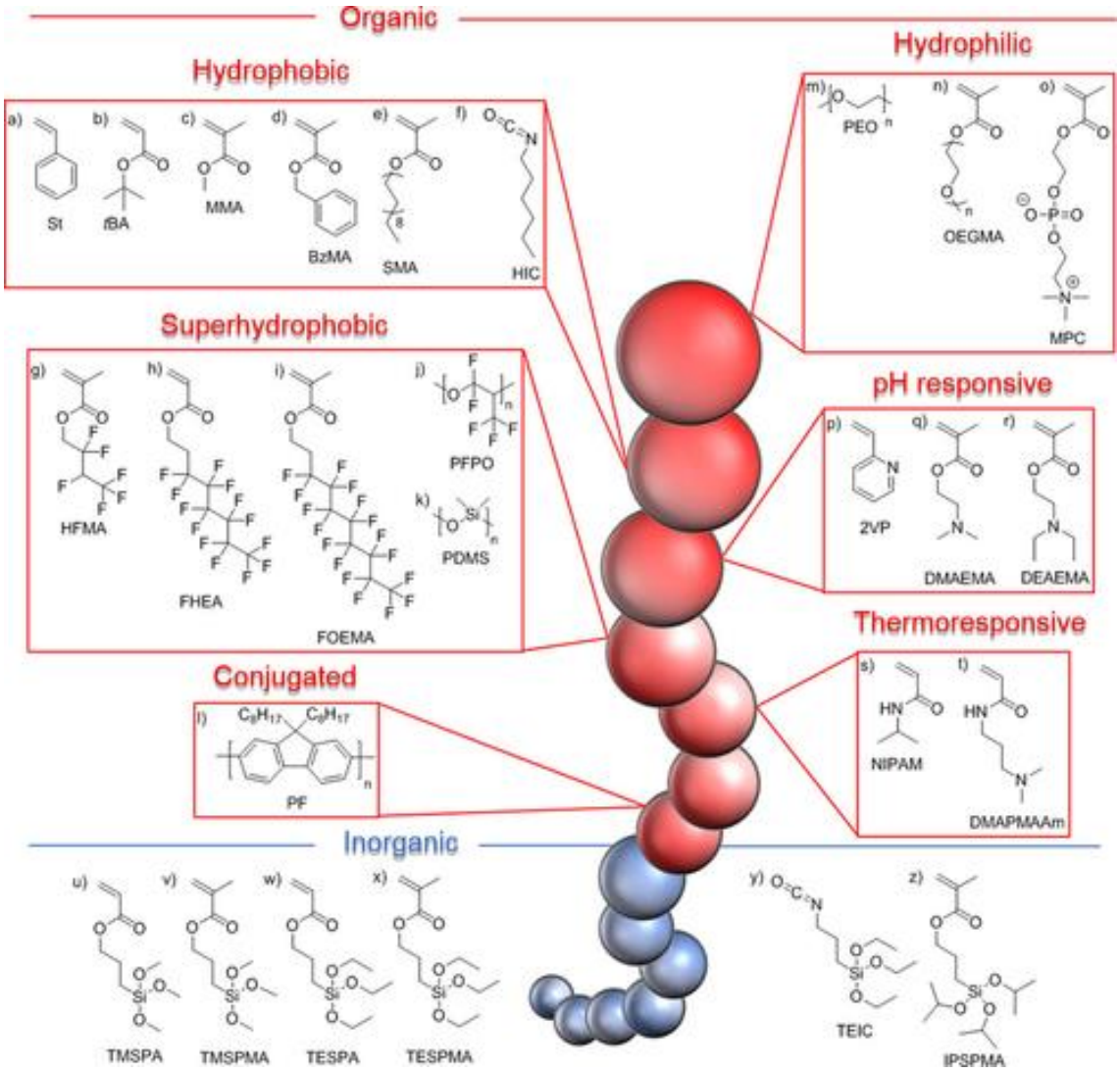

Figure 3. Overview of hybrid inorganic/organic copolymers for the preparation of functional materials. Reprinted with permission from ref. [24]. Copyright © 2018 WILEY-VCH Verlag GmbH & Co. KGaA.

Since the sol-gel process is a well-established and well-understood process, the finding of new hybrid materials with unique properties and characteristics is highly dependent on the used precursor. Owing to fabricate new materials with unique characteristics, it is desirable to use polymeric precursors with more sophisticated structures such as gradient or block

copolymer precursors. Thus, this chapter focuses on the synthesis of such hybrid inorganic/organic block copolymers as well as statistical/gradient copolymers.

1.2.1 Hybrid inorganic/organic block copolymers

1.2.1.1 Common hydrophobic monomers for self-assembly in bulk and in solution

Common hydrophobic monomers such as styrene (St), *tert*-butyl acrylate (tBA), methyl methacrylate (MMA) or benzyl methacrylate (BzMA) can be used in combination with a silane-based block to form self-assembled structures in bulk and in solution (organic solvents) due to the incompatibility of the blocks. NMP was used by the group of Beyou for the synthesis of 3-(triethoxysilyl) propyl acrylate (TESPA) and styrene based linear diblock copolymers PTESPA$_{91}$-*b*-PS$_{34,88,175,317}$, [26] PTESPA$_{113}$-*b*-PS$_{489}$, PS$_{272}$-*b*-PTESPA$_{130,224,290,336,}$ [27] and triblock copolymers PTESPA$_{113}$-*b*-PS$_{82,158,330,489}$-*b*-PTESPA$_{82\text{-}120,}$ [28] and PS$_{272}$-*b*-PTESPA$_{130,224,290,336}$-*b*-PS$_{260\text{-}293}$. [29] All copolymers were synthesized in a stepwise procedure. Diblock copolymers PTESPA$_{91}$-*b*-PS$_{34,88,175,317}$ were synthesized by polymerization of TESPA in bulk at 115 °C with an alkoxyamine initiator styryl-*N*-tert-butyl-1-diethylphosphono-2,2-dimethylpropyl nitroxide (styryl-DEPN), followed by polymerization of styrene from the macroinitiator in toluene at 115 °C; while triblock copolymers PS-*b*-PTESPA-*b*-PS were synthesized from a PS-DEPN macroinitiator. Similar copolymers, PTESPMA-*b*-PS, based on 3-(triethoxysilyl) propyl methacrylate (TESPMA) instead of TESPA and with a PS block of higher molecular weight (DP up to 1150) had been previously synthesized by the group of Chen. They reported the synthesis of PTESPMA$_{88}$-*b*-PS$_{408}$, PTESPMA$_{78}$-*b*-PS$_{348}$, PTESPMA$_{71}$-*b*-PS$_{780}$, PTESPMA$_{66}$-*b*-PS$_{758}$, PTESPMA$_{46}$-*b*-PS$_{1009}$, PTESPMA$_{46}$-*b*-PS$_{1669}$ and PTESPMA$_{38}$-*b*-PS$_{187\text{-}1150}$ [30] and with PTESPMA blocks of even higher molecular weights (PTESPMA$_{38K}$-*b*-PS$_{65,93,152}$ and PTESPMA$_{48K}$-*b*-PS$_{42,111}$) via RAFT polymerizations mediated by cumyl dithiobenzoate (CDB).The diblock copolymers were obtained by sequential polymerization in bulk of TESPMA at 60 °C, followed by styrene at 90 °C. More refined architectures based on styrene and a silicon-based monomer (3-(trimethoxysilyl) propyl methacrylate, TMSPMA) could be obtained by ATRP. Indeed, Lin and co-workers used β-cyclodextrin modified with 21 bromo moieties (21-Br β-CD) as initiator to prepare star-like β-CD-(PTMSPMA)$_{21}$ or β-CD-(PS$_{43}$-*b*-PTMSPMA$_{84}$)$_{21}$ and β-CD-(PS$_{59}$-*b*-PTMSPMA$_{3,6,15,80}$)$_{21}$ copolymers with 21 branches and a molar mass up to 346.1 kDa. [31] Well-defined copolymers with dispersities ranging from 1.10 to 1.36 were obtained by the sequential polymerization of the monomers using CuBr/*N*,*N*,*N'*,*N''*,*N''*-pentamethyldiethylenetriamine (PMDETA)-mediated ATRP. Anionic polymerization was used by Park *et. al*. for the

synthesis of linear diblock copolymers based on styrene and an isocyanate gellable monomer, poly(styrene)-*b*-poly[3-(triethoxysilyl) propylisocyanate] (PS-*b*-PTEIC), via sequential anionic polymerization in THF at –78 °C by employing *n*-butyl lithium (*n*BuLi) as base (M_w/M_n ≈1.2, M_n of PTEIC of 23 kDa, M_n of PS 39 or 200 kDa. [32-34] PS-*b*-PTEIC consists of a flexible PS coil and a rigid rod-like helical PTEIC block, thus presenting a supplementary degree of ordering compared to other diblock copolymers, which can be useful in self-assembly.

Copolymers of monomers with sol-gel active substituents and methyl methacrylate (MMA) were synthesized by GTP, ATRP and RAFT. The group of Mellon prepared PMMA-*b*-PTMSPMA using 2-cyanoprop2-yl dithiobenzoate (CDPB)-mediated RAFT polymerization of TMSPMA and MMA in 1,4-dioxane (60-80 °C) that led to high conversions (90%). [35] The block copolymers were obtained either by a one pot procedure or in a two-step reaction by first isolating PMMA and using it as macroinitiator. More recently, Georgiou *et. al.* prepared TMSPMA and MMA based linear diblock copolymers in a one-pot synthesis, via GTP in THF at 20 °C using 1-methoxy-1-(trimethylsiloxy)-2-methyl propene (MTS) as initiator. They obtained copolymers with low degree of polymerization (≈20 for each block) and low dispersity of 1.05, as can be expected from this polymerization method. [36] Finally, Gao *et. al.* reported the synthesis of PMMA-*b*-PTMSPMA copolymers of higher molar mass (M_n ≈39 kDa) from either ethyl 2-bromoisobutyrate (EBiB) or a fluorinated initiator by two sequential CuCl/PMDETA mediated ATRP in cyclohexanone: first MMA was polymerized at 90 °C, followed by TMSPMA at 110 °C. [37] Fukuda. *et. al.* reported the synthesis of PMMA-*b*-P(MMA-*r*-TMSPMA) in a one-pot ATRP polymerization. First the polymerization of MMA was initiated by ethyl 2-bromoisobutyrate (EBiB) in toluene at 70 °C in presence of CuCl and sparteine. After 24 h, TMSPMA was added to the mixture of PMMA-Cl and residual MMA to afford the desired copolymer. [38]

The group of Liu synthesized linear diblock copolymers containing *tert*-butyl acrylate (*t*BA) and a sol-gel active monomer. Poly[3-(triisopropyloxysilyl)propyl methacrylate]-*b*-poly(*tert*-butyl acrylate) (PIPSPMA$_{10}$-*b*-P*t*BA$_{70}$) was obtained via anionic polymerization in THF at –78 °C by employing *sec*-butyl lithium as base. [39, 40] Li *et. al.* synthesized hybrid di- and triblock copolymers composed of styrene, TMSPMA and *tert*-butyl acrylate (*t*BA) of higher molecular weight in bulk via 2-cyano-2-propyl dithiobenzoate (CPDB)-mediated RAFT. [41] PS$_{205}$-*b*-P(*t*BA$_{45\text{-}352}$-*co*-TMSPMA$_{4\text{-}56}$) and PS$_{99}$-*b*-P(*t*BA$_{64,106}$-*co*-TMSPMA$_{23,24}$)-*b*-PS$_{99}$ were obtained with low dispersities (1.09-1.33) and after deprotection of the *tert*-butyl groups, these hybrid copolymers were used to prepare surfactant-mimicking structures.

Thickett *et. al.* [42, 43] reported the PISA of benzyl methacrylate (BzMA)-based diblock copolymers via RAFT starting from alkoxysilane functional methacrylic macroRAFT agents, as depicted in Scheme 1.

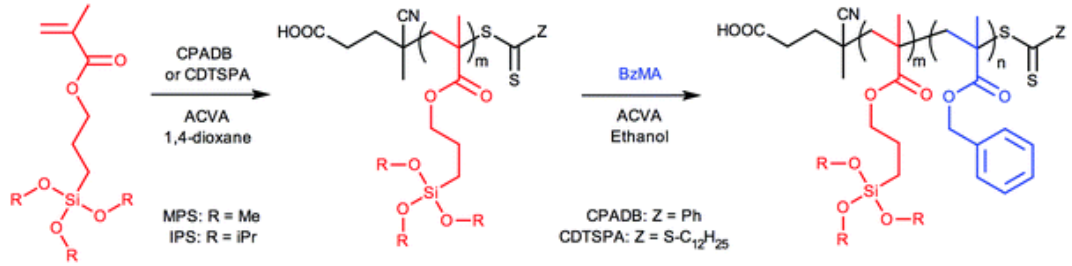

Scheme 1. Schematic presentation of the PISA process by using solvophilic block segments composed of TMSPMA and IPSMA and followed chain extension of BzMA in etnanol as the solvophobic block. Reprinted with permission from ref. [43]. Copyright © 2016 The Royal Society of Chemistry.

Structures such as vesicles and spheres based on PTMSPMA-*b*-PBzMA or a diblock containing a more stable monomer with sol-gel active substituent, namely 3-(triisopropoxysilyl)propyl methacrylate (IPSPMA), PIPSPMA-*b*-PBzMA, were obtained. Two chain transfer agents (CTA) were tested for the homopolymerization of TMSPMA and IPSPMA for targeted DP of 40 and 65: 4-cyanopentanoic acid dithiobenzoate (CPADB) and 4-cyano-4- [(dodecylsulfanylthiocarbonyl) sulfanyl] pentanoic acid (CDTSPA). [43] The trithiocarbonate-mediated RAFT homopolymerization of TMSPMA or IPSPMA yielded polymers with lower dispersities of 1.20-2.36 compared to the dithiobenzoate-mediated RAFT polymerizations (1.23-11.30). The authors explained it by intermolecular crosslinking of the sol-gel active moiety during the polymerization, which might be greatly influenced by the nature of the CTA chain end. They further extended this approach to the preparation of triblock, in which the solvophilic block segment was composed of PEGMA and TMSPMA. [44]

1.2.1.2 Monomers with long alkyl chains for polymer brushes

Stearyl methacrylate (SMA) and *n*-hexylisocyanate (HIC) are interesting monomers as they can form "brush-type" polymers, given their pendant long alkyl chain, especially the former. Linear as well as star-shaped block copolymers of stearyl methacrylate-based monomers with sol-gel active substituents were synthesized by ATRP or RAFT. These copolymers can form interesting self-assembled structures in solution [45, 46] as well as in bulk,[47] given the brush-like structure of the SMA block. Wang *et. al.* reported the preparation of relatively low molecular weight linear diblock copolymers based on SMA

and TMSPMA in anisole at 90 °C by CuCl/2,2'-bipyridine (bpy) mediated ATRP. [45] It afforded a $PSMA_{25}$-*b*-$PTMSPMA_3$ copolymer with low dispersity of 1.14. In a previous publication they reported a triblock copolymer $PTMSPMA_{15}$-*b*-$PSMA_{32}$-Fc-$PSMA_{32}$-*b*-$PTMSPMA_{15}$ which had been initiated from chloroacetylferrocene (Fc) with a similar polymerization procedure. [48] In a following publication, the same authors reported the synthesis of star block copolymers, S-($PSMA_{128}$-*b*-$PS_{9,56}$)$_4$ starting from a tetrafunctional initiator, pentaerythritol tetrakis(2-bromoisobutyrate). [46] The obtained star-shaped copolymers had higher dispersities compared to the linear ones, namely dispersities ranging from 1.76 to 1.79 but molar masses of up to 58.0 kDa. Finally, the group of Benicewicz prepared poly[3-(triethoxysilyl) propyl methacrylate]-*b*-poly(stearyl methacrylate) ($PTESPMA_{666}$-*b*-$PSMA_{553}$) of very high molecular weight in DMF at 60 °C by employing CPDB-mediated RAFT polymerization. [47] Poly(*n*-hexylisocyanate)-*b*-poly[3-(trimethoxysilyl) propyl methacrylate] ($PHIC_{125}$-*b*-$PTMSPMA_{6,12}$) were synthesized by Park *et. al.* by a combination of living anionic polymerization and ATRP. [49] As previously mentioned anionic polymerization of substituted isocyanates leads to a rod-like organic block that can be combined with a sol-gel reactive block. In this publication, HIC was polymerized with sodium bisphenylamide in THF at –98 °C and end-capped with 2-bromoisobutanoyl bromide. This allowed to initiate the ATRP of TMSPMA in presence of CuBr/PMDETA in toluene at 35 °C.

1.2.1.3 Perfluorinated monomers for superhydrophobicity

Fluorine-containing monomers such as hexafluorobutyl methacrylate (HFMA), 2-(perfluorohexyl) ethyl acrylate (FHEA) or 2-(perfluorooctyl)ethyl methacrylate (FOEMA), and polymers such as poly(perfluoropropylene oxide) (PFPO) or even poly(dimethylsiloxane) (PDMS) can be used for superhydrophobic coatings. In these cases, one has to use appropriate solvents to carry out the polymerization otherwise solubility issues could be encountered due to the presence of fluorine-containing monomers and polymers. The group of Liu synthesized various diblock copolymers containing 3-(triisopropyloxysilyl)propyl methacrylate (IPSPMA) as sol-gel active monomer and various fluorinated organic monomers. Namely, they obtained poly[3-(triisopropyloxysilyl) propyl methacrylate]-*b*-poly[2-(perfluorooctyl) ethyl methacrylate] ($PIPSPMA_{10}$-*b*-$PFOEMA_{10}$) via anionic polymerization of the monomers in THF at –78 °C. The polymerization was carried out in one-pot by sequential addition of IPSPMA and FOEMA after initiating the system with diphenylethene and *sec*-butyl lithium. [50] With a less stringent polymerization procedure, namely ATRP, the same authors extended this

polymer library to PIPSPMA-*b*-PFOEMA with higher DP (PIPSPMA$_{13}$-*b*-PFOEMA$_{30}$ and PIPSPMA$_{18}$-*b*-PFOEMA$_{22}$ [51] and PIPSPMA$_{12}$-*b*-PFOEMA$_{30}$, PIPSPMA$_{15}$-*b*-PFOEMA$_{31}$ and PIPSPMA$_{19}$-*b*-PFOEMA$_{23}$[52]) but still low dispersities of 1.10-1.14. In this case, PIPSPMA-*b*-PFOEMA was synthesized by ATRP of IPSPMA from EBiB in the presence of CuCl/bpy and $CuBr_2$ in trifluorotoluene at 80 °C, followed by polymerization of FOEMA from the preformed PIPSPMA-Cl macroinitiator under similar conditions. [51, 52] In addition, they synthesized poly[2-(perfluorohexyl)ethyl acrylate]-*b*-poly[3-(triisopropoxysilyl)propyl methacrylate] (PFHEA$_{21}$-*b*-PIPSMA$_{15}$), using CuBr/PMDETA-mediated ATRP in trifluorotoluene at 80 °C for the synthesis of the PFEMA macroinitiator, followed by ATRP of IPSPMA using the same conditions but bpy as ligand instead of PMDETA. [53] PFHEA$_{21}$-*b*-PIPSPMA$_{15}$ was obtained with dispersity of 1.61. Liu *et. al.* also synthesized block copolymers of PIPSPMA with a poly(perfluoropropylene oxide) block (PFPO), PIPSPMA$_7$-*b*-PFPO$_{14}$. [51] PIPSPMA$_7$-*b*-PFPO was synthesized from a commercial poly(perfluoropropylene oxide) modified with 2-hydroxyethyl 2-bromo-2-methylpropanoate to afford PFPO-Cl. This macroinitiator was then used for the polymerization of IPSPMA via ATRP with CuCl/bpy in a TFT/methoxy perfluorobutane mixture at 80 °C. [51] Other authors, Liu *et. al.,* used $CuBr_2$/bpy mediated ATRP in presence of Cu^0 in butanone at 90 °C to afford superhydrophobic poly(2,2,3,4,4,4-hexafluorobutyl methacrylate)-*b*-poly[3-(trimethoxysilyl) propyl methacrylate] (PHFMA-*b*-PTMSPMA) with various HFMA/TMSPMA ratio of ≈ 95:5, 90:10, 80:20. [54] It should also be mentioned that superhydrophobicity can also be achieved with silicon-based polymers such as commercial poly(dimethylsiloxane) (PDMS). For instance PDMS$_{76}$-*b*-PIPSPMA$_{10}$ was synthesized by the group of Liu to produce superhydrophobic fabrics. [55] ATRP of IPSPMA in presence of CuCl/bpy and $CuBr_2$ from a PDMS-Br macroinitiator in trifluorotoluene at 80 °C afforded a block copolymer PDMS$_{76}$-*b*-PIPSPMA$_{10}$ with low dispersity <1.1. Jen and co-workers synthesized linear triblock copolymers composed of 2,7-(9,9-di-*n*-hexylfluorene) (HF), PEGMA and TMSPMA to prepare rod-coil block copolymer brushes in solution. For this reason, they chain extended a HF based macroinitiator via CuBr/HMTETA mediated ATRP in anisole at 80 °C to afford PHF-*b*-PPEGMA$_{44,92}$-*b*-PTMSPMA$_{16,11}$ copolymers with molar masses of 13.2–18.6 kDa and dispersities of 1.32–1.52. [56]

1.2.1.4 Conjugated monomers for light emitting materials

The combination of fluorescent monomers with silane-based monomers can be used for the preparation of robust light emitting materials at the nanoscale. Liu and co-workers

synthesized PF-*b*-PTMSPMA copolymers by ATRP of TMSPMA with CuBr/1,1,4,7,10,10-hexamethyltriethylenetetramine (HMTETA) in *o*-dichlorobenzene at 90 °C using a polyfluorene (PF) macroinitiator with two pendant C_8H_{17} alkyl chains. [57] The PF macroinitiator had been synthesized using a Suzuki coupling of 9,9-dioctyl-2-bromo-7-4,4,5,5-tetramethyl-1,3,2-dioxaborolan-2-yl fluorene. The block copolymerization afforded linear diblock copolymers PF_{5K}-*b*-$PTMSPMA_{1.2,3.3,8.7\ kDa}$ with reasonable dispersities ranging from 1.16 to 1.80 and molar masses up to 20 kDa.

1.2.1.5 Monomers/polymers based on ethylene oxide motif for self-assembly

Hydrophilic organic block based on ethylene oxide motif such as poly(ethylene oxide) or oligoethylene oxide-based (meth)acrylates are usually used for biomedical applications to confer biocompatibility to (nano)materials or limit protein adsorption. Most of these copolymers have so far been synthesized via ATRP, which involves the use of copper complexes as catalyst. However, in biomedicine, the presence of copper is unwanted due to its inherent toxicity. Therefore, it seems more relevant to synthesize ethylene oxide motif-based copolymers for this kind of applications via RAFT, which does not involve a transition-metal catalyst. The group of Chen synthesized a series of linear amphiphilic diblock poly(ethylene oxide)-*b*-poly[3-(trimethoxysilyl) propyl methacrylate] (PEO-*b*-PTMSPMA) copolymers by employing CuBr/PMDETA mediated ATRP of TMSPMA in anisole at 50, 70 or 90 °C from various PEO-Br macroinitiators: PEO_{17}-*b*-$PTMSPMA_{200,}$ PEO_{45}-*b*-$PTMSPMA_{29,42,49,54,59,180}$ or PEO_{113}-*b*-$PTMSPMA_{46,206}$. [58-63] To obtain this macroinitiator, poly(ethylene oxide) methoxyether was functionalized at the chain-end with 2-bromo-2-methylpropionyl bromide to afford poly(ethylene oxide) 2-bromo-2-methylpropionate (PEO-Br). They further extended their ATRP procedure to prepare PEO and TESPMA based linear amphiphilic diblock PEO_{45}-*b*-$PTESPMA_{69,90,162}$, PEO_{113}-*b*-$PTESPMA_{64}$ and triblock copolymers $PTESPMA_{40}$-*b*-PEO_{45}-*b*-$PTESPMA_{40}$. [63, 64] With a similar procedure, the group of He obtained block copolymers with other DP, namely PEO_{45}-*b*-$PTMSPMA_{73,100,158}$. [65] PEO-*b*-PTMSPMA has also been synthesized via RAFT by another group.[66] A PEO macro-CTA with a *p*-fluorodithioester group was used as macroinitiator for TMSPMA and the polymerization was conducted in 1,4-dioxane at 70^°C to afford PEO_{5kDa}-*b*-$PTMSPMA_{10kDa}$ with dispersities lower than 1.4. Both the groups of Chen [58] and He [65] synthesized poly(ethylene oxide)-*b*-poly[3-(trimethoxysilyl) propyl methacrylate-*r*-methyl methacrylate] (PEO-*b*-P(TMSPMA-*r*-MMA)) copolymers with various feed ratios and dispersities ranging from 1.17 to 1.96. They used a similar procedure involving copolymerization of MMA and TMSPMA via ATRP starting from PEO-

Br macroinitiator in presence of CuBr/PMDETA in anisole at 55 or 70 °C. By using a lower copolymerization temperature (55 °C), the group of He obtained lower dispersities (1.17-1.26) for PEO-*b*-P(TMSPMA-*r*-MMA) of similar monomer ratio (PEO_{114}-*b*-$P(TMSPMA_{32-124}$-*r*-MMA_{55-423}) compared to the polymers obtained by Chen *et. al.* (PEO_{45}-*b*-$P(TMSPMA_{19-42}$-*r*-$MMA_{14-67})$). Yang *et. al.* prepared poly(ethylene oxide)-*b*-poly[3-(triethoxysilyl)propyl methacrylate]-*b*-polystyrene (PEO-*b*-PTESPMA-*b*-PS) triblock copolymers by a two-step RAFT polymerization. [67] In the first step, a PEO-CPADB was used as macroinitiator for polymerization of TESPMA in dioxane at 60 °C, which was subsequently chain extended with styrene by polymerization in dioxane at 90 °C to afford the corresponding triblock copolymer PEO_{45}-*b*-$PTESPMA_{35}$-*b*-$PS_{110,448}$.

The synthesis of polymers based on the ethylene oxide motif is not only limited to linear structures: macromolecular engineering has been used to produce miktoarm and H-shaped polymers based on such motifs. Infact, Ngai *et. al.* used a PEO-(Br)-*b*-PS macroinitiator to synthesize miktoarm μ-PEO_{45}-*b*-PS_{25-86}-*b*-$PIPSPMA_{25-35}$ triblock copolymers by bpy/CuBr mediated ATRP of IPSPMA in anisole at 80 °C. The diblock copolymer macroinitiator, namely PEO-(Br)-*b*-PS, was synthesized via the esterification of PEO-(OH)-*b*-PS with 2-bromoisobutyryl bromide in dichloromethane and the PEG-(OH)-*b*-PS diblock copolymers bearing hydroxyl group on the junction point had been previously synthesized by the click reaction between a PEO bearing an azide and hydroxyl group and an α-alkynyl-ω-diethylamino-polystyrene. The miktoarm μ-PEO_{45}-*b*-PS_{25-86}-*b*-$PIPSPMA_{25-35}$ triblock copolymers were obtained with relatively low dispersities of 1.22-1.27 and a molar mass of up to 22.5 kDa. [68] Pan and co-workers prepared H-shaped PEO-*b*-PTMSPMA copolymers by using a multifunctional Br_2-PEO-Br_2 macroinitiator. [69] They obtained well-defined H-shaped $(PTMSPMA_{98,154,182})_2$-*b*-PEO_{91}-*b*-$(PTMSPMA_{98,154,182})_2$ copolymers with dispersities of 1.05-1.17 and a molar mass of up to ≈50 kDa by employing CuBr/bpy mediated ATRP in methanol at room temperature. Not only PEO used as macroinitiator has been used for the synthesis of ethylene oxide motif-containing hybrid block copolymers but also oligoethylene oxide-based (meth)acrylates have been polymerized by several groups to obtain such copolymers. Zhang *et. al.* prepared poly[oligo(ethylene glycol)methyl methacrylate]-*b*-poly(glycidyl methacrylate)-*b*-poly[3-(methacryloxypropyl) trimethoxysilane] ($POEGMA_{26}$-*b*-$PGMA_{42}$-*b*-$PTMSPMA_{27}$) triblock copolymers by sequential RAFT polymerization of OEGMA, GMA and TMSPMA using CPADB as chain transfer agent in anisole at 70 °C. [70] This procedure afforded the corresponding triblock copolymer with low conversion of the TMSPMA block segment and a dispersity of 1.18. The group of Fukuda reported the synthesis of poly(methyl

methacrylate)-*b*-poly[oligo(ethylene glycol)methyl methacrylate]-*b*-poly[oligo(ethylene glycol)methyl methacrylate-*r*-3-(trimethoxysilyl) propyl methacrylate] ($PMMA_{82}$-*b*-$POEGMA_{28}$-*b*-$P(OEGMA_{0.53}$-*r*-$TMSPMA_{0.47})_{15}$). These linear amphiphilic triblock copolymers were obtained via sequential ATRP of MMA and OEGMA in diphenyl ether at 70 °C in presence of CuBr and sparteine, followed by addition of TMSPMA two hours after polymerization of the POEGMA block, leading to the third mixed block P(OEGMA-*r*-TMSPMA). [71] A huge step in macromolecular engineering was done by the group of Müller, who reported the synthesis of various cylindrical polymer brushes (CPB) based on a poly(2-bromoisobutyryloxyethylmethacrylate) (PBIEM) backbone of high DP (1,500 or 3,200) with PTMSPA-*b*-POEGMA brushes, namely $[PTMSPA_{21}$-*b*-$POEGMA_{58}]_{1,500}$, $[PTMSPA_{20}$-*b*-$POEGMA_{57}]_{3,200}$, $[PTMSPA_{41}$-*b*-$POEGMA_{68}]_{3,200}$ and $[PTMSPA_{72}$-*b*-$POEGMA_{95}]_{3,200}$. [72] The PBIEM obtained by anionic polymerization was used as multifunctional initiator of the CuBr/PMDETA mediated ATRP of TMSPA and OEGMA in benzene at 80 °C to yield the bottle brush-like hybrid inorganic/organic block copolymer. In a following publication, the authors synthesized a series of CPB with P*t*BA-*b*-PTMSPA-*b*-POEGMA brushes instead of PTMSPA-*b*-POEGMA brushes: $[PtBA_{75}$-*b*-$PTMSPA_{50\text{-}170}$-*b*-$POEGMA_{150\text{-}400}]_{3,200}$.[73] Thickett *et. al.* prepared PEGMA-*b*-PTMSPMA diblock solution with a targeted TMSPMA DP ranging from 80 to 600 under several reaction conditions by using a PEGMA based MacroCTA with a DP of 9, 18 and 36. [42]

1.2.1.6 Monomers based on phosphorylcholine for antibacterial properties

Zwitterionic materials exhibit antibacterial properties due to the reduction or elimination of non-specific adsorption at the solid/liquid interface. For this reason, diblock copolymers composed of poly(2-methacryloyloxyethyl phosphorylcholine) (PMPC) and PTMSPMA were synthesized by sequential ATRP polymerization of TMPSMA and MPC in ethanol at 60 °C in presence of CuBr and ligands such as PMDETA and bpy, respectively. [74] The length of the PMPC block was varied to afford $PMPC_{15,30,50,70,200}$-*b*-$PTMSPMA_{14}$.

1.2.1.7 pH responsive monomers for structures with pH responsive properties in aqueous media

pH responsive copolymers based on 2-vinylpyridine (2VP), 2-(dimethylamino)ethyl methacrylate (DMAEMA) or 2-(diethylamino)ethyl methacrylate (DEAEMA) can self-assemble depending on the solution pH and form various nanosized structures including core-shell micellar structures, hollow spheres and vesicles. They can also be used to produce pH-responsive hydrogels, microgels, and layer-by-layer (LbL) nanofilms, which

have potential as drug carriers or controlled releasing systems for instance. Moreover, P2VP is not only pH responsive but can also complex Au ions or Au nanoparticles (NP).
Chen and co-workers reported in a series of publications the synthesis of di- and tri- block copolymers based on poly(2-vinylpyridine) (P2VP) and TESPMA. For instance, the diblock $P2VP_{162}$-*b*-$PTESMA_{60}$ was synthesized by sequential bulk polymerization of TESPMA with CDB at 60 °C, followed by the polymerization of 2VP under the same conditions from the PTESPMA macroinitiator. [75] This procedure was further extended to synthesize linear $P2VP_{331}$-*b*-PS_{265}-*b*-$PTESPMA_{58}$ or $P2VP_{432}$-*b*-PS_{249}-*b*-$PTESPMA_{55}$ [76, 77] and $P2VP_{310}$-*b*-$PTESPMA_{58}$-*b*-PS_{322}[78] triblock copolymers.
Matyjaszewski *et. al*. reported the synthesis of linear pH-responsive poly[2-(dimethylamino)ethyl methacrylate]-*b*-poly[3-(trimethoxysilyl)propyl methacrylate] $PDMAEMA_{97}$-*b*-$PTMSPMA_{5,20,60}$ and $PDMAEMA_{53\text{-}197}$-*b*-$PTMSPMA_{40}$ diblock copolymers via ATRP. [79] These copolymers were synthesized in a two-step procedure starting with the polymerization of DMAEMA with 1,2-bis(bromoisobutyryloxy)ethane as initiator via CuCl/HMTETA-mediated ATRP in the presence of $CuCl_2$ in acetone at room temperature. From the PDMAEMA-Cl macroinitiator, TMSPMA was then polymerized with CuCl/PMDETA in anisole at 60 °C. A similar procedure was used for the preparation of PTMSPMA-*b*-PDMAEMA-*b*-PTMSPMA or PDMAEMA-*b*-PTMSPMA-*b*-PDMAEMA triblock copolymers except that the macroinitiator was bifunctional and would constitute the middle block in the final triblock. Chen and co-workers reported the synthesis of $PDMAEMA_{252\text{-}598}$-*b*-$PTESPMA_{55\text{-}162}$ copolymers of higher DP and longer PDMAEMA block via RAFT polymerization at 60 °C mediated by CDB in 1,4-dioxane or THF, for DMAEMA and TESPMA respectively. [80] Linear (2-(dialkylamino)ethyl methacrylate)-based hybrid copolymer architectures containing a third monomer/polymer of different nature (either PEO or PMMA) have also been reported. Du and Armes reported PEO-*b*-P(DEAEMA-*stat*-TMSPMA) containing 2-(diethylamino)ethyl methacrylate (DEAEMA). While PDMAEMA is a weak polybase, which is soluble at neutral pH or in acidic media due to protonation of the tertiary amine groups, PDEAEMA, although very similar structurally, is immiscible in water and completely insoluble at neutral pH. PEO_{43}-*b*-P($DEAEMA_{40}$-*stat*-$TMSPMA_{40}$) and PEO_{43}-*b*-P($DEAEMA_{60}$-*stat*-$TMSPMA_{10}$) were obtained by ATRP of DEAEMA and TMSPMA from a PEO-Br macroinitiator using CuBr/bpy as catalytic system. The statistical copolymerization was carried out in methanol at 20°C and the diblock copolymers were obtained with low dispersities of 1.13–1.15. [81] Zhang *et. al.* synthesized P(MMA-*co*-TMSPMA)-*b*-PDEAEMA block copolymers in DMF at 70 °C via CuBr/bpy copolymerization of MMA and TMSPMA with 2-bromoisobutyrate as initiator and CuBr/bpy as metal/ligand

system, followed by polymerization of DEAEMA with CuBr/tris(2-(dimethylamino)ethyl)amine (Me_6TREN). [82] P(MMA-*co*-TMSPMA)$_{27.1\ kDa}$-*b*-PDEAEMA$_{53.6\ kDa}$ was obtained with high dispersity of 1.85.

1.2.1.8 Thermoresponsive monomers for structures with temperature responsive properties in aqueous media

Thermoresponsive polymers are promising candidates for a range of biological applications, including controlled drug delivery, bioseparation, smart surfaces, and regulating enzyme activity. Most applications have relied on abrupt changes in aqueous solubility at either a lower critical solution temperature (LCST) or an upper critical solution temperature (UCST). The most commonly used thermoresponsive polymer is poly(*N*-isopropylacrylamide) (PNIPAM) that exhibit LCST behaviour, where the responsive polymer is soluble due to extensive hydrogen bonding interactions with the surrounding water molecules and upon heating, hydrogen bonding with water is disrupted, and intra- and intermolecular hydrogen bonding/hydrophobic interactions dominate, which results in a transition in solubility, also called "coil to globule transition". Liu *et. al.* reported the preparation of thermoresponsive poly(*N*-isopropylacrylamide)-*b*-poly[3-(trimethoxysilyl) propyl methacrylate] (PNIPAM-*b*-PTMSPMA) copolymers via RAFT polymerizations mediated by benzyl dithiobenzoate (BDTB). PNIPAM$_{48}$-*b*-PTMSPMA$_{60}$ and PNIPAM$_{300}$-*b*-PTMSPMA$_{52}$ were obtained by polymerization of NIPAM in 1,4-dioxane at 70 °C followed by TMSPMA also in 1,4-dioxane at 80 °C, reaching high molecular masses and dispersities ranging from 1.10 to 1.17. [83] More recently, Becer and Jones used a trithiocarbonate (butyl ether 2-(dodecylthiocarbonothioylthio)-2-methylpropionate) for RAFT polymerization of *N*-[3-(trimethoxysilyl) propyl] acrylamide (TMSPAAm) and NIPAM based diblock copolymers in THF at 60 °C. The yielded PNIPAM$_{81,162,371}$-*b*-PTMSPAAm$_{28}$ show good dispersities ranging from 1.10-1.19. [84] More refined structures were achieved via ATRP. Zhang *et. al.* synthesized P(MMA-*co*-TMSPMA)-*b*-PNIPAM block copolymers in DMF at 70 °C via CuBr/bpy copolymerization of MMA and TMSPMA with 2-bromoisobutyrate as initiator and CuBr/bpy as metal/ligand system, followed by polymerization of NIPAM with CuBr/Me_6TREN. [82] P(MMA-*co*-TMSPMA)$_{27.1kDa}$-*b*-PNIPAM$_{40kDa}$ was obtained with dispersity of 1.37. Similarly, Perrier et. al. [85] synthesized PEO$_{45}$-*b*-P(MMA$_{46}$-co-TMSPMA$_2$)-*b*-PNIPAM$_{429}$ triblock copolymers via CuCl/Me_6TREN mediated ATRP in a DMF/2-propanol mixture at 30 °C using a PEO-*b*-P(MMA-*co*-TMSPMA)-Br macroinitiator.

1.2.1.9 Organic block with dual response for stimuli-sensitive structures in aqueous media

Due to the versatility of RAFT as a polymerization technique, it has been used for the preparation of pH and temperature responsive hybrid organic-inorganic copolymers. Zhang and co-workers conducted successfully 2-(2-carboxylethylsulfanylthiocarbonylsufanyl) propionic acid (TTC)-mediated RAFT copolymerization of NIPAM and TMSPMA in DMF at 70 °C followed by the polymerization of DEAEMA from this macroinitiator in THF at 70 °C. They afforded thermoresponsive hybrid inorganic/organic block copolymers composed of NIPAM, DEAEMA and TMSPMA (P(NIPAM$_{235}$-*co*-TMSPMA$_5$)-*b*-PDMAEMA$_{362}$) with high conversions and dispersity of 1.38. [86] In the same group, P(NIPAM-*co*-TMSPMA)-*b*-PDMAPMAAm based on *N*-[3-(dimethylamino) propyl] methacrylamide (DMAPMAAm) was prepared under similar conditions, namely in THF at 70 °C by employing TTC-mediated RAFT polymerization. A copolymer P(NIPAM$_{188}$-*co*-TMSPMA$_4$)-*b*-PDMAPMAAm$_{92}$ with a high dispersity of 1.57 was obtained, showing that the conditions of polymerization should be optimized. [87] Boyer *et. al.* successfully synthesized P(DEGMA-*co*-OEGMA)-*b*-P(TMSPMA-*co*-VBA) by using 4-cyano-4- (phenylcarbonothioylthio)pentanoic acid (CPPA)-mediated RAFT polymerization with high converions and dispersities of 1.30. In the first step, they prepared a MacroCTA composed DEGMA and OEGMA in a molar ratio of 3/1 and 2.2/1 in acetonitrile at 70 °C, which was subsequently chain extended with TMSPMA and 3-vinylbenzaldehyde (VBA) in a molar ratio of 1/4 in toluene at 90 °C. [88, 89]

1.2.2 Hybrid inorganic/organic statistical copolymers

Random/statistical hybrid inorganic/organic copolymers composed of (meth)acrylic monomers with aliphatic moieties are promising precursor for the fabrication of hybrid bioactive scaffolds. [90] Recently, Jones and co-workers synthesized linear PMMA$_{480}$–*co*-PTMSPMA$_{48}$ (M_n = 59.5 kDa, $Đ$ = 1.12), randomly branched PMMA$_{480}$–*co*-PTMSPMA$_{48}$ (M_n = 11.8 kDa, $Đ$ = 2.27) and star-shaped PMMA$_{480}$–*co*-PTMSPMA$_{48}$ (M_n = 61.4 kDa, $Đ$ = 1.21) copolymers by using CDB-mediated RAFT polymerization in toluene at 70 °C [91, 92], as depicted in Scheme 2. For the preparation of randomly branched copolymers, TMSPMA and MMA were copolymerized in the presence of ethylene glycol dimethacrylate (EGDMA) as crosslinker in a molar ratio 0.7/100 (EGDMA/MMA), whereas the star-shaped copolymers were synthesized by using an “arm-first” approach. Herein, linear PMMA$_{480}$-*co*-PTMSPMA$_{48}$ was used as MacroCTA, which was subsequently core-crosslinked with EGDMA in a molar ratio of 8/1 (MacroCTA/EGDMA) by using FRP in toluene at 70 °C.

Similarly, Jones *et. al.* synthesized well-defined $PMMA_{120}$-*co*-$PTMSPMA_{12}$, $PBMA_{90}$-*co*-$PTMSPMA_{9}$ and PMA_{137}-*co*-$PTMSPMA_{13.7}$ with molar masses of 12.8–14.5 kDa and disperties ranging from 1.10 to 1.12 by using CDB-mediated RAFT polymerization in toluene at 70 °C. [93] Hong *et. al.* reported the fabrication of thermoresponsive Au-polymer hybrid microgels in solution by using P(MEO_2MA-*co*-OEGMA-*co*-TMSPMA) copolymers as precursors. [94] For this purpose, MEO_2MA, OEGMA and TMSPMA were copolymerized with three different molar ratios of 9/1/1, 8.5/1.5/1 and 8/2/1 via CDBPA-mediated RAFT polymerization in THF at 70 °C.

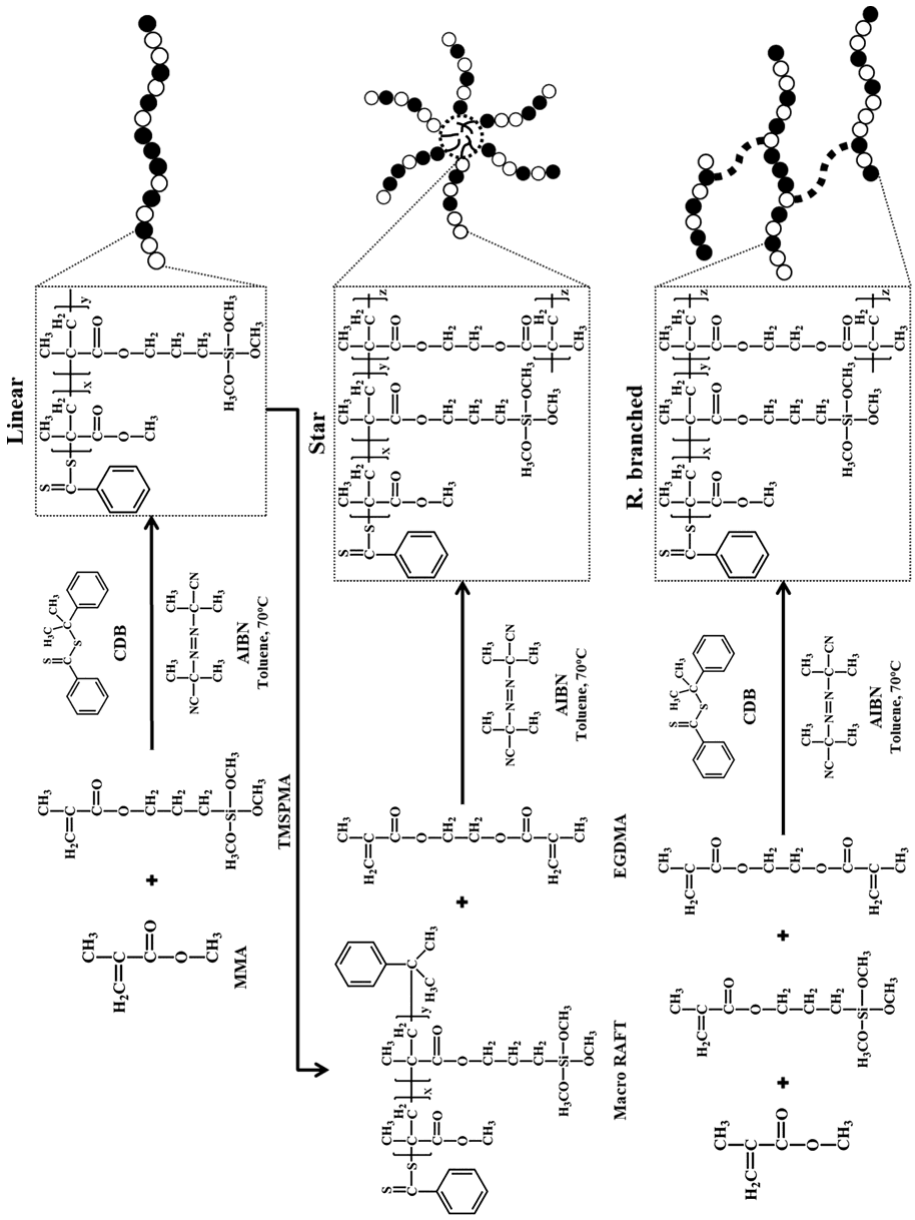

Scheme 2. CDB mediated RAFT polymerization of MMA and TMSPMA of three different architectures: linear (top), star (center) and randomly branched polymers (bottom). Reprinted with permission from ref. [92]. Copyright © 2016 American Chemical Society.

The CDBPA-mediated RAFT polymerization was terminated at conversions of 49–59% yielding well-defined copolymers with molar masses of 20.05–20.17 kDa and dispersities of 1.08–1.09. Robin and co-workers demonstrated the cotelomerization of TMSPMA and PFDA in acetonitrile at 80 °C. They synthesized short PTMSPMA$_{7.36}$-*stat*-PPFDA$_{0.64}$ with a molar mass of 2.2 kDa by using 2-mercaptoethanol as telogen agent and AIBN as initiator.[95, 96] The short copolymers were functionalized with 2-isocyanatoethyl methacrylate in order to afford macromonomers, which were subsequently grafted-*onto* silica nanoparticles. Roh *et. al.* synthesized comb-like amphiphilic graft copolymers composed of vinylidene fluoride (VDF), chlorotrifluoroethylene (CTFE), 4-styrene sulfonic acid (SSA) and TMSPMA by using CuCl/HMTETA mediated ATRP in DMSO at 90 °C. The comb-like graft copolymers were obtained after grafting SSA and TMSPMA from a P(VDF-*co*-CDTFE) macroinitiator in a molar ratio of 1/6/0.5 (macroinitiator/SSA/TMSPMA). [97]

To date, the synthesis of well-defined hybrid inorganic/organic copolymers is mainly focused on the preparation of block and statistical/random copolymers. Due to the inherent reactivity of the sol-gel active Si-OR motifs, the synthesis of more sophisticated microstructures such as gradient copolymers are exceptionally demanding and require a careful adjustment of the experimental conditions in order to minimize undesired side reactions.

2 Theory

2.1 Macromolecular engineering via reversible-deactivation radical polymerization

The advent of controlled polymerization techniques such as controlled living anionic polymerization (CLAP), group transfer polymerization (GTP) or reversible-deactivation radical polymerization (RDRP) techniques, including nitroxide-mediated radical polymerization (NMP), atom-transfer radical polymerization (ATRP) and reversible-addition and fragmentation chain transfer (RAFT) polymerization, lead to a new era in synthetic polymer chemistry. [98] Contrary to (co)polymers synthesized via free-radical polymerization (FRP) and other uncontrolled polymerization techniques, (co)polymers synthesized via controlled polymerization techniques exhibit well-defined structures with a narrow molecular weight distribution (MWD) of (co)polymer chain lengths (low dispersity). Furthermore, controlled polymerization techniques allow the preparation of copolymers with various composition including block, gradient or grafted copolymers and thus, are frequently used in macromolecular engineering. Due to their ease of operation RDRP techniques rapidly become one of the most used techniques in polymer synthesis. These techniques are based on a reversible deactivation of an active propagating radical species, as depicted in Scheme 1. An efficient deactivation can be achieved through reversible radical coupling of the active radical (NMP) [99], reversible catalytic deactivation (ATRP) [100, 101] and degenerate chain transfer (RAFT) [102], as illustrated in Scheme 3.

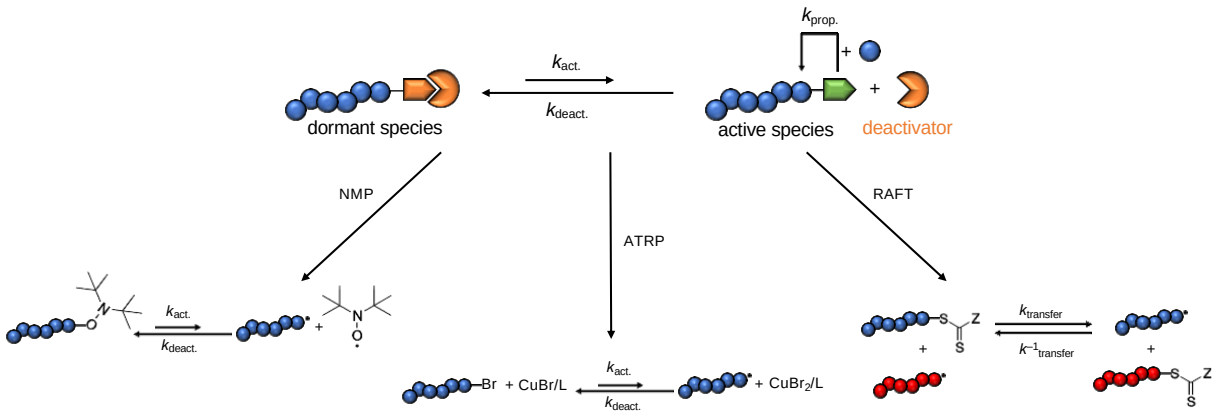

Scheme 3. Schematic representation of the basic principle of RDRP (top) and illustration of the reversible (de)activation step in NMP, ATRP and RAFT (bottom).

The differences and similarities of all three RDRP techniques are summarized in Table 1.

Table 1. General comparison of all three RDRP techniques.

	NMP	**ATRP**	**RAFT**
Monomers	styrene, acrylates & acrylamides	mainly monomers with activated double bonds	monomers with activated and non-activated double bonds
Conditions	high temperatures (>120 °C)	wide temperature range (–30 °C to 150 °C)	elevated temperatures (> 50 °C)
Additives	nitroxides	catalyst ligand alkyl halide	CTA radical source
Pros	+ no further additives	+ various initiation procedures available	+ wide range of polymerizable monomers
Cons	– narrow range of polymerizable monomers – requires high reaction temperatures	– removal of the metal catalyst requires tedious purification	– requires a radical source

Since, all three RDRP techniques are suited to synthesize copolymers with various morphologies and precise structure in a controlled fashion, in this project was chosen RAFT polymerization to prepare hybrid inorganic/organic block and gradient copolymers. The two major advantages of RAFT are the large range of polymerizable monomers compared to NMP as well as the lack of excessive purification compared to ATRP.

2.1.1 Mechanism of reversible addition-fragmentation chain transfer polymerization

RAFT polymerization was invented in 1998 by several scientists at the Commonwealth Scientific and Industrial Research Organization (CSIRO) in Australia. The popularity of RAFT polymerizations steadily increased since 1998, due to the great versatility and robust nature of RAFT and a large scope of applications in synthetic polymer chemistry. [103, 104] Thus, RAFT polymerization is nowadays one of the most frequently used RDRP technique to synthesize (co)polymers composed of various monomers, as well as with various compositions and architectures. The essential principle of RAFT is a degenerate chain transfer between an active radical species and a thiocarbonyl–thio compound, so-called chain-transfer agent (CTA), which is governed by two equilibria that are superimposed on the FRP processes initiation, propagation, and termination, as shown in Figure 4.

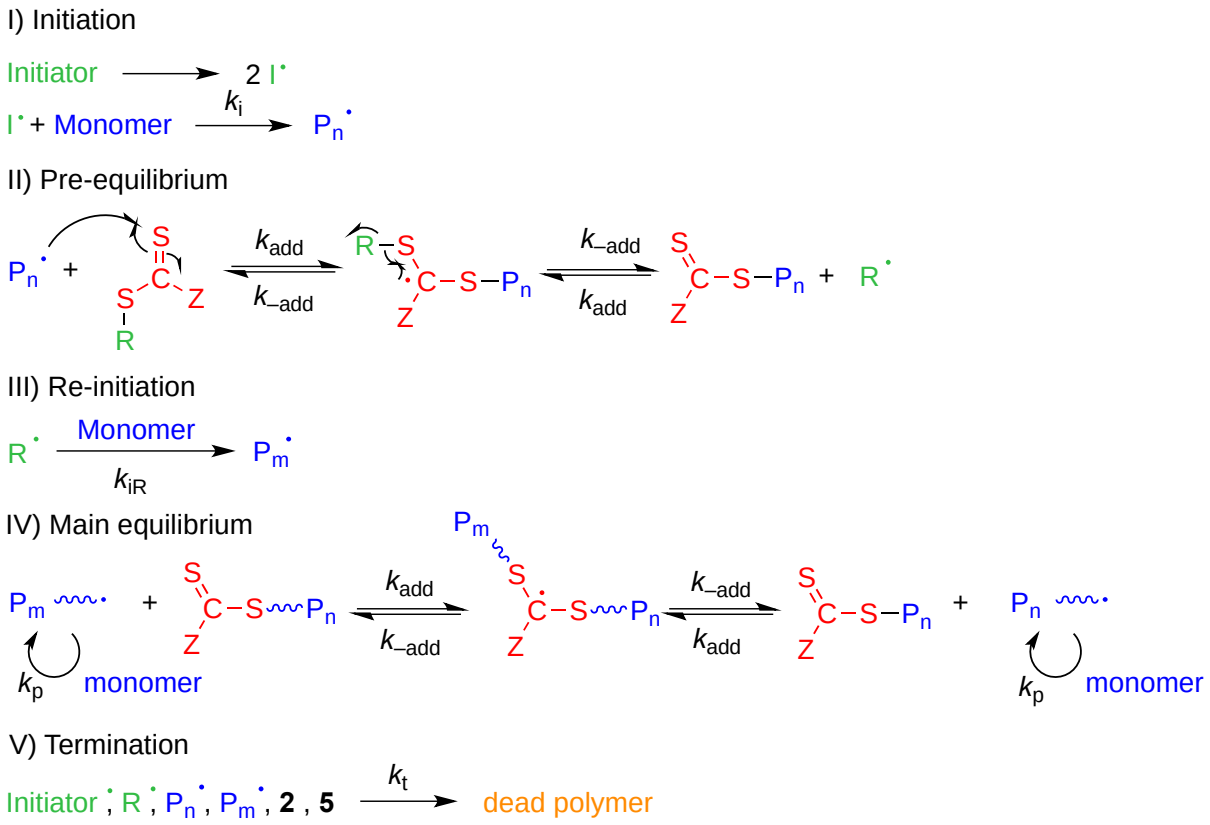

Figure 4. Mechanism of RAFT polymerization. Adapted with permission from ref. [103]. Copyright © 2015 American Chemical Society.

Contrary to other RDRP techniques, RAFT polymerizations require a radical source (e.g. AIBN) to initiate the polymerization and drive the RAFT process. Subsequently in a pre-equilibrium, adds a propagating radical ($P_{n\cdot}$) adds to the RAFT agent, generating a RAFT-polymer radical adduct which either can fragment in the forward direction or

in the backward direction. The forward fragmentation leads to the release of a radical leaving group R., which re-initiate the polymerization by adding monomer units and generate a dormant MacroCTA species. The MacroCTA species is considered as dormant species, since it can forward fragment to generate $P_{n.}$ as well as add more monomers due to radical coupling. The pre-equilibrium dominates the reaction kinetics until all CTA agent is consumed, which generally results in so-called induction periods or periods of slow initiation. Afterwards, the RAFT process is dominated by the main equilibrium, which is mainly affected by the nature of the CTA agent. The ratio between CTA and radical source should be at least two (or more) to ensure a reasonable high chain-end fidelity of the obtained polymer.However, a common misunderstanding of RAFT polymerization is to keep the initial initiator concentration ($[I]_0$) as high as possible to increase the overall rate of polymerization.[102] In fact, the rate of polymerization (R_p) is affected by the same parameters as in FRP and thus, can be manipulated by other parameters such as monomer concentration ([*M*]) , monomer propagation rate (k_p) and the decomposition rate of the radical source (k_d), as detailed in equation 1.

$$R_p(t) = k_p[M]\sqrt{\frac{f k_d [I]_0 e^{-k_d t}}{k_t}} \qquad (1)$$

where *f* is the initiator efficiency and k_t is the rate of termination. A controlled RAFT process relies on careful adjustment of the reaction parameters and balancing of the monomer reactivity and the reactivity of the used RAFT agent to achieve a high number of living chains (*L*, “livingness”), as depicted in equation 2.

$$L = \frac{[CTA]_0}{[CTA]_0 + 2f[I]_0(1 - e^{-k_d t})\left(1 - \frac{f_c}{2}\right)} \qquad (2)$$

where $[CTA]_0$ is the initial CTA concentration. The term 2*f* refers to the fact that one initiator molecule gives two radicals, whereas the term 1 – f_c/2 refers to the number of chains produced in radical–radical termination event with f_c as coupling factor (f_c = 1, 100% termination by bimolecular coupling and f_c = 0, 100% termination by bimolecular disproportionation). Further termination and retardation phenomena are ascribed in the

slow-fragmentation (SF) hypothesis and chain length dependent intermediate-radical-termination (IRT) hypothesis, which result in prolonged induction periods or early chain radical termination. Considering retardation in RAFT polymerizations is exceptional important and is especially pronounced in dithiobenzoate mediated RAFT polymerizations. [105-107] The careful design of the CTA is a crucial factor to perform a RAFT polymerization in a controlled fashion. [108] CTAs are thiocarbonyl-thio compounds that possess labile and easily homolytically cleavable S-R bonds and a stabilizing Z-group. Both features greatly affect the transfer rate $C_{Transfer} = k_{add}/k_{-add}$ of the CTA. Typical controlled RAFT polymerizations display transfer rates of $C_{Transfer}$ = 10-100 and thus, multiple transfer events occur before one monomer unit is added. RAFT agents with these desired transfer rates exhibit fast forward fragmentation of the intermediate radical and a fast re-initiation of the released R. species, which leads to a shortened induction period. Since the rate of propagation is not exclusively predetermined by the CTA, it is necessary to carefully evaluate the reactivity of the monomer. More-activated monomers (MAM) such as methacrylate or styrene require RAFT agents with a Z-group that activated the C=S bond. Whereas, less-activated monomers (LAM) such as vinyl acetate demand RAFT agents with Z groups that donate electron density to the C=S and thus, destabilize the intermediate radical to favour forward fragmentation. The monomer reactivity increases as followed: methacrylates ≤ methacrylamides < styrene < acrylates ≤ acrylamides < *N*-vinyl heteroaromatics < vinyl amides < vinyl esters. Thus, typically used CTA's to polymerize methacrylates are dithioesters with Z = R or to polymerize styrene/acrylates trithiocarbonates with Z = SR, as displayed in Figure 5.

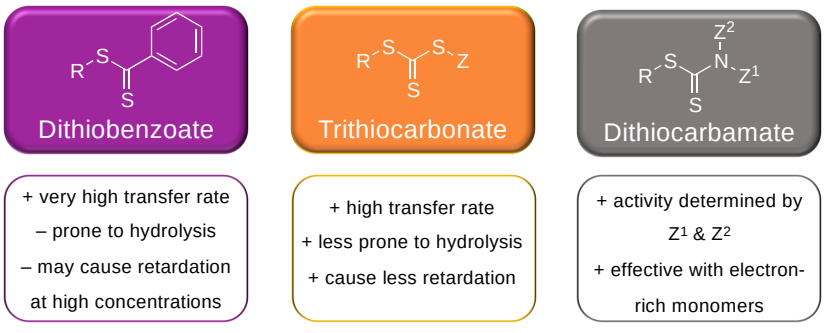

Figure 5. General structures of commonly used CTAs.

The Z group affect the rate of addition of propagating radicals as well as the rate of fragmentation of the intermediate radicals in the pre-equilibrium and main equilibrium.

A guideline for the selection of a proper Z group for a set of monomers is shown in Figure 6.

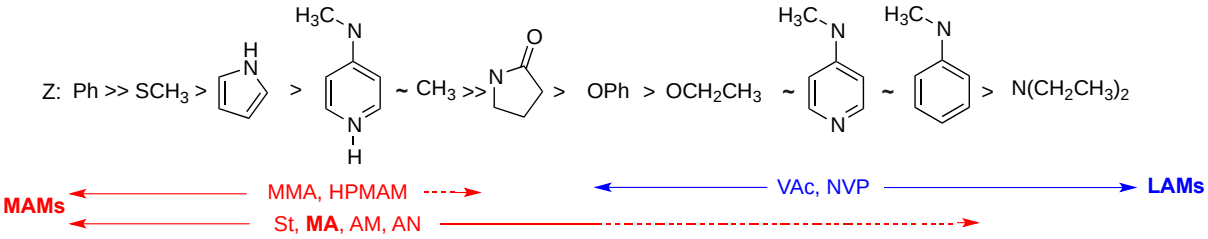

Figure 6. Guideline for the selection of the Z group of RAFT agents for various monomers. Adapted with permission from ref. [108].

The nature of the R group affects the rate of fragmentation of the intermediate radicals as well as an optimal choice of the R group enable the efficient re-initiation and inhibit retardation during the polymerization. A crucial factor governing these abilities, is the radical stability. The rate of fragmentation increases in the series primary < secondary < tertiary and is affected by stabilizing substituents, due to delocalization of the radical center. A general guideline for the selection of the R group is displayed in Figure 7.

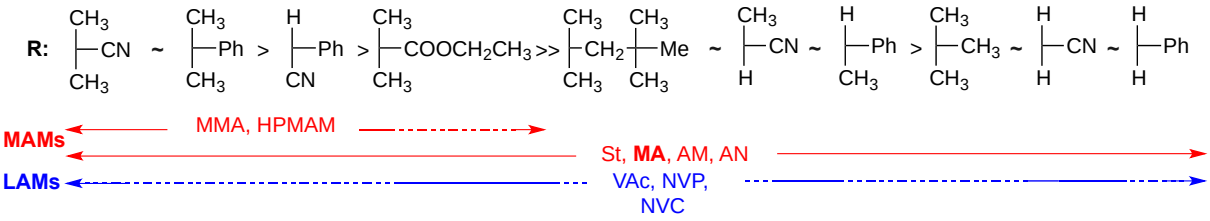

Figure 7. Guideline for the selection of the R group of RAFT agents for various monomers. Adapted with permission from ref. [108].

In summary, RAFT is a powerful technique to synthesize (co)polymers with a wide scope of application in synthetic polymer chemistry and has become one of the most intensively used RDRP technique in recent years, due to its ease of operation and versatility.

2.1.2 Copolymerization kinetics

Copolymers consist of two or more chemically distinct subunits (A, B, C …), wherein the copolymers are classified by the comonomer composition along the copolymer chain. In general, copolymers are classified into four classes according to their appearing composition.

(A) Alternating copolymer: Alternating copolymers exhibit a perfectly alternating arrangement of A and B comonomers.
(B) Block copolymer: Block copolymers are composed of two or more distinct block segments, which are covalently attached to each other.
(C) Gradient copolymer: Gradient copolymers exhibit a linear or non-linear gradual change in the comonomer composition along the copolymer chain.
(D) Random copolymers: Random copolymers show a non-ordered arrangement of A and B comonomers and thus, display no characteristic composition.

Assuming a copolymerization mixture composed of two monomers M_1 and M_2, four different reactions occur at the reactive chain end, as depicted in Scheme 4.

$$M_1 + M_1^* \xrightarrow{k_{11}} M_1M_1^*$$
$$M_1 + M_2^* \xrightarrow{k_{12}} M_1M_2^*$$
$$M_2 + M_1^* \xrightarrow{k_{21}} M_2M_1^*$$
$$M_2 + M_2^* \xrightarrow{k_{22}} M_2M_2^*$$

Scheme 4. Reactions occurring in a copolymerization mixture composed of two monomers M_1 and M_2.

Following Scheme 2, the reactivity ratios are defined as $r_1 = k_{11}/k_{12}$ and $r_2 = k_{22}/k_{21}$. The copolymerization kinetics are described as a change of the comonomer concentration [M_1] and [M_2] during the copolymerization as a function of the instantaneous ratio [M_1]/[M_2]. These observations are summarized in the so-called Mayo-Lewis equation or copolymer equation, as shown in equation 3. [109]

$$\frac{d\,[M_1]}{d[M_2]} = \frac{[M_1](r_1[M_1] + [M_2])}{[M_2]([M_1] + r_2[M_2])} \qquad (3)$$

According to Fineman and Ross, equation 3 can be converted into a linear form, to easily determine the corresponding reactivity ratios r_1 and r_2, as detailed in equation 4 and 5. [110]

$$\frac{[M_1]}{[M_2]}\frac{m_2}{m_1}\left(\frac{m_1}{m_2}-1\right) = r_1\frac{[M_1]^2}{[M_2]^2}\frac{m_2}{m_1} - r_2 \qquad (4)$$

$$\frac{[M_2]}{[M_1]}\left(\frac{m_1}{m_2}-1\right) = -r_2\frac{[M_2]^2}{[M_1]^2}\frac{m_1}{m_2} + r_1 \qquad (5)$$

This form of the copolymer equation yields a linear form by plotting $\frac{[M_1]^2}{[M_2]^2}\frac{m_2}{m_1}$ versus $\frac{[M_1]}{[M_2]}\frac{m_2}{m_1}\left(\frac{m_1}{m_2}-1\right)$ as well as $\frac{[M_2]^2}{[M_1]^2}\frac{m_1}{m_2}$ versus $\frac{[M_2]}{[M_1]}\left(\frac{m_1}{m_2}-1\right)$ with the slope corresponding to r_1 and the intercept corresponding to r_2 (and *vice versa*)**.** The Fineman-Ross method is exclusively valid for low conversions (≤15%), because it does not consider the reaction between a comonomer unit and a growing copolymer chain. To overcome this limitation, Kelen and Tüdos [111, 112] introduced an arbitrary constant α ($\alpha > 0$) and divided equation 2 and 3 by $\alpha + \frac{[M_1]^2}{[M_2]^2}\frac{m_2}{m_1}$, as shown in equation 6.

$$\frac{\frac{[M_1]}{[M_2]}\frac{m_2}{m_1}\left(\frac{m_1}{m_2}-1\right)}{\alpha + \frac{[M_1]^2}{[M_2]^2}\frac{m_2}{m_1}} = \frac{r_1\frac{[M_1]^2}{[M_2]^2}\frac{m_2}{m_1}}{\alpha + \frac{[M_1]^2}{[M_2]^2}\frac{m_2}{m_1}} - \frac{r_2}{\alpha + \frac{[M_1]^2}{[M_2]^2}\frac{m_2}{m_1}} \qquad (6)$$

Similar to the Fineman-Ross method, Kelen and Tüdos transformed equation 6 into a linear form, as detailed in equation 7.

$$\eta = r_1\xi - r_2\frac{1-\xi}{\alpha} \qquad (7)$$

with

$$\frac{\frac{[M_1]}{[M_2]}\frac{m_2}{m_1}\left(\frac{m_1}{m_2}-1\right)}{\alpha + \frac{[M_1]^2}{[M_2]^2}\frac{m_2}{m_1}} = \eta$$

and

$$\frac{r_1 \frac{[M_1]^2}{[M_2]^2}\frac{m_2}{m_1}}{\alpha + \frac{[M_1]^2}{[M_2]^2}\frac{m_2}{m_1}} = \xi$$

Plotting η versus ξ yields a straight line which gives $\frac{-r_2}{\alpha}$ as ordinate section ($\xi = 0$) r_1 as slope ($\xi = 1$). The arbitrary constant α is defined as the mean of the smallest and largest $\frac{[M_1]^2}{[M_2]^2}\frac{m_2}{m_1}$ value, as shown in equation 8, and results in a more uniform data distribution.

$$\alpha = \sqrt{\left(\frac{[M_1]^2}{[M_2]^2}\frac{m_2}{m_1}\right)_{min}}\sqrt{\left(\frac{[M_1]^2}{[M_2]^2}\frac{m_2}{m_1}\right)_{max}} \qquad (8)$$

However, the Kelen-Tüdos-Method (KTM) does not take into account a composition drift during polymerization, due to the different reactivities of the comonomers. To overcome this limitation, Kelen and Tüdos extended their approach to higher conversions (≤ 50%) and introduced three new parameters Z, G and H, as detailed below: [112]

$$Z = \frac{\log(1-\theta_x)}{\log(1-\theta_y)}$$

$$G = \left(\frac{F-1}{Z}\right)$$

$$H = \frac{F}{Z^2}$$

where θ_x and θ_y are the mole fractions of the comonomers. This so-called extended Kelen-Tüdos-Method (EKTM) allows to determine the reactivity ratios of a comonomer pair at higher conversions with small errors compared to the KTM. The reactivity ratios display preferences for propagation and thus, are frequently used to characterize the outcome of a copolymerization. In general, a high *r* value indicates a tendency to insert a monomer species to a propagating species of the same chemical nature, whereas a small *r* value indicates a tendency to insert a monomer species to a propagating species of different chemical nature. These tendencies give rise to five different observations, as listed below.

(A) $r_1 = r_2 \gg 1$: Since both monomers preferentially react with themselves, two homopolymers are formed.

(B) $r_1 = r_2 > 1$: The homopolymerization of M_1 is favored over the crosspolymerization with M_2 and results in a block copolymer.

(C) $r_1 = r_2 \approx 1$: Since both monomers exhibit the same reactivity, a random copolymer is formed, in which the initial comonomer feed correspond to the overall copolymer composition.

(D) $r_1 = r_2 \approx 0$: The crosspropagation of M_1 and M_2 is preferred yielding alternating copolymers.

(E) $r_1 \gg 1 \gg r_2$: In the initial stage of the copolymerization M_1 is preferentially incorporated into the copolymer chain, while the incorporation of M_2 into the copolymer chain becomes more favored by consumption of M_1 or addition of more M_2 yielding gradient copolymers.

2.1.3 Synthesis of (multi)block copolymers via RAFT polymerization

Block copolymers with well-defined composition, precise structure and two or more distinct block segments can be obtained by RAFT mediated polymerizations. Generally, two pathways are frequently employed to prepare (multi)block copolymers via RAFT polymerizations in solution and in bulk: [113] I) Sequential polymerization of each block in one pot. This approach requires high conversions (≥99%) after each synthesized block segment to prevent the formation of mixed block segments; II) Stepwise polymerization of each block by using a macroinitiator-approach. This approach requires a high chain-end fidelity of the employed macroinitiator to enable efficient re-initiation of the first block, as demonstrated in Figure 8.

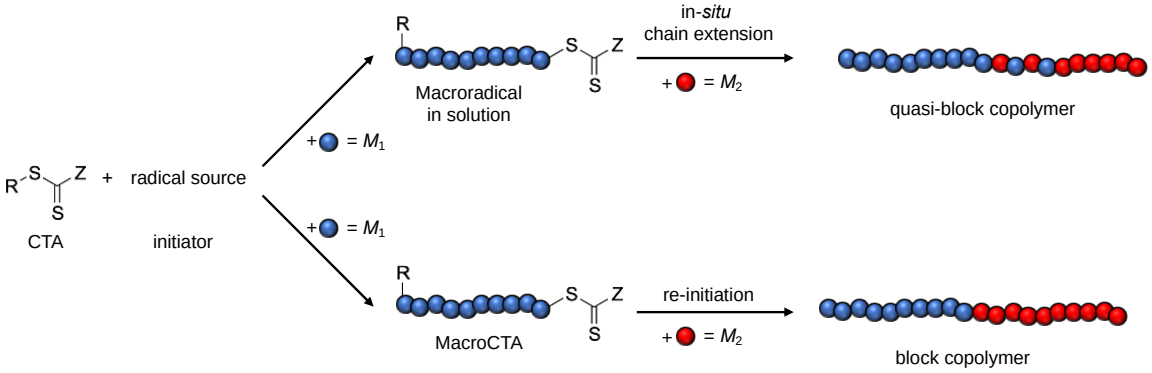

Figure 8. Synthesis of block copolymers via RAFT mediated polymerization.

The first approach yields so-called quasi-block copolymers with two distinct block segments that are interconnected through a mixed block segment. Advances in the field of RAFT and careful adjustment of the reaction parameters enabled the preparation of sequence-defined multiblock copolymers with well-defined structures and compositions by using a one-pot RAFT approach. [115-117] However, the most frequently used approach to synthesize diblock copolymers is the macroinitiator-approach, due to its ease of operation and reliability.

2.1.4 Synthesis of gradient copolymers via RAFT polymerization

In recent years, gradient copolymers attracted considerable attention, due their unique physicochemical properties. Nevertheless, the tedious synthesis of such gradient copolymers is still a tough task in the field of polymer synthesis and resulted in the development of more sophisticated approaches to synthesize these copolymers. [114] In general, two different approaches are employed to synthesize gradient copolymers namely the spontaneous gradient and the semi-batch (forced) gradient approach: [115]

A) Spontaneous gradient polymerization: The reaction of the monomers is polymerized to high conversions. There is no presence of either azeotropic points or ideal random copolymerization. The polymer composition changes due to the different reactivity of the monomers. This technique has three major limitations: I) It only applies to strictly non-random copolymerization systems. II) It also will fail in close vicinity to azeotropic points. III) It does not enable to afford polymers with complete control over the compositional gradient over the full copolymer chain.

B) Semi-batch (forced) gradient polymerization: Reactions that involve an initiation of a polymerization in a pure monomer or a monomer mixture and subsequent continuous feeding of monomer (or monomer mixture) during the full reaction time. This can lead to polymers with full control over the composition based on the addition rates and the compositions of the added monomers/mixtures.

The basic principle of the semi-batch forced gradient approach is displayed in Figure 9. In this approach, monomer B is continuously added to a mixture of monomer A (feeding) via a syringe-pump in order to alter the comonomer feed during the copolymerization. Following this approach, Steinhauer and co-workers synthesized well-defined gradient copolymers composed of two acrylic monomers while using RAFT mediated

polymerizations. [116, 117] They employed two acrylic monomers with ideal random copolymerization characteristics, in which the change of the comonomer feed in the solution is directly proportional to the change of the commoner composition within the polymer chain.

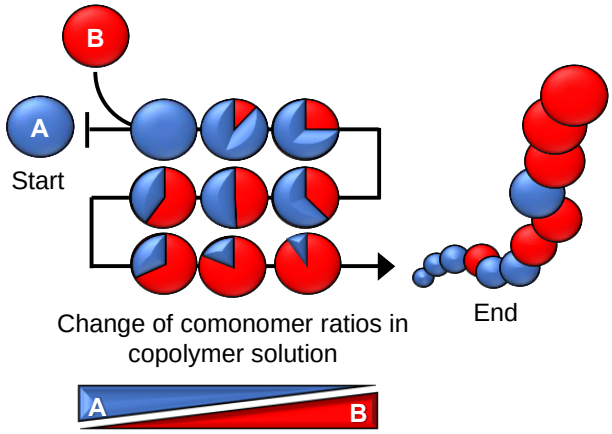

Figure 9. Schematic illustration of the semi-batch forced gradient approach.

Thus, the gradual change from comonomer A to B is directly proportional the feeding rate of comonomer B. An alteration from this technique, is the injection of a pre-defined amount of monomer B to a mixture of A (shot). This so-called multi-shot or many-shot approach gives gradient copolymers with a more block-like/tapered microstructure compared to the former feeding technique. [118]

2.2 Fabrication of thin polymer films via sol-gel grafting-*onto* approach

Hybrid inorganic/organic copolymers with gelable Si-OR motifs are commonly used to prepare polymer coatings via a sol-gel grafting-onto approach. [119] The basic principle of the sol-gel process relies on the preparation of colloidal particles that are dispersed in solution (sol), which form a 3-dimensional network due to condensation of reactive Si-OH groups (gel). The network formation is induced by the hydrolytic cleavage of the Si-OR motifs to form nucleophilic Si-OH motifs (sol formation). These motifs are reacting subsequently in a polycondensation to form a polysilsesquioxane network with Si–O–Si motifs, as shown in Scheme 5. The sol-gel chemistry of silica precursors is typically driven by an acid or base catalyst and tremendously affect the structure of the resulting gel, due to significant different relative rates of hydrolysis and condensation. Gels prepared via an acid catalysed process exhibit open weakly branched polymer-like structure due to a faster rate of hydrolysis compared to the rate of condensation. On the contrary, in base catalysed

sol-gel process the rate of condensation is faster than the rate of hydrolysis yielding a gel composed of compact colloidal particles. [120]

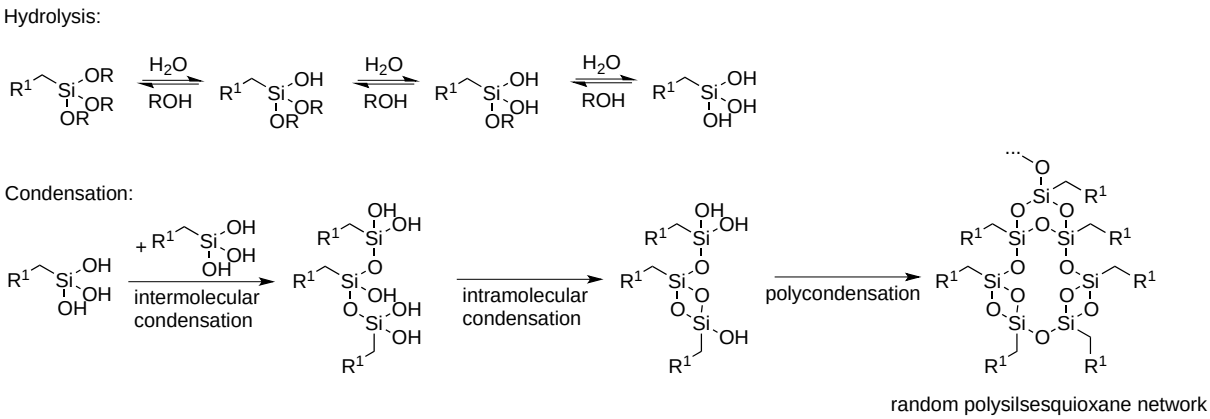

Scheme 5. Mechanism of the sol-gel process by using hybrid copolymers with gelable Si-OR motifs as precursor.

Due to the versatile applicability of the sol-gel process several techniques were developed to functionalize glass-surfaces via a grafting-onto approach, as demonstrated in Figure 10. These techniques are based on the iterative immersion of a sample in a sol (dip-coating), dispersion of a sol on a sample via rotation (spin-coating), and deposition of a sol on the sample by applying a current (electrodeposition). Since the iterative immersion of a sample requires high loadings of the polymer precursor and yields films with heterogeneous layer thickness, dip-coating is a non-suitable technique to prepare sol-gel coatings with homogeneous layer thickness. Electrodeposition is mainly applied for the coating of (thermo)conductive samples such as metals and thus, is not suitable for preparation of sol-gel coatings on glass samples. Owing to prepare sol-gel coatings with a homogeneous layer thickness on glass samples, spin-coating is the most suitable and reliable technique. In addition, spin-coating requires rather low loadings of the polymer precursor to prepare a coating in comparison to dip-coating. The film thickness of a spin-coated film is proportional to the inverse of the square of the angular velocity, and therefore an increase of the spinning rate results in a decreased film thickness (and *vice versa*). However, the precise layer thickness depends on the material concentration/viscosity, solvent evaporation rate as well as on the choice of the TASPMA precursor. Thin gel layer exhibits a higher tendency to shrink upon drying by using TASPMA precursors with bulky R-substituents. [120]

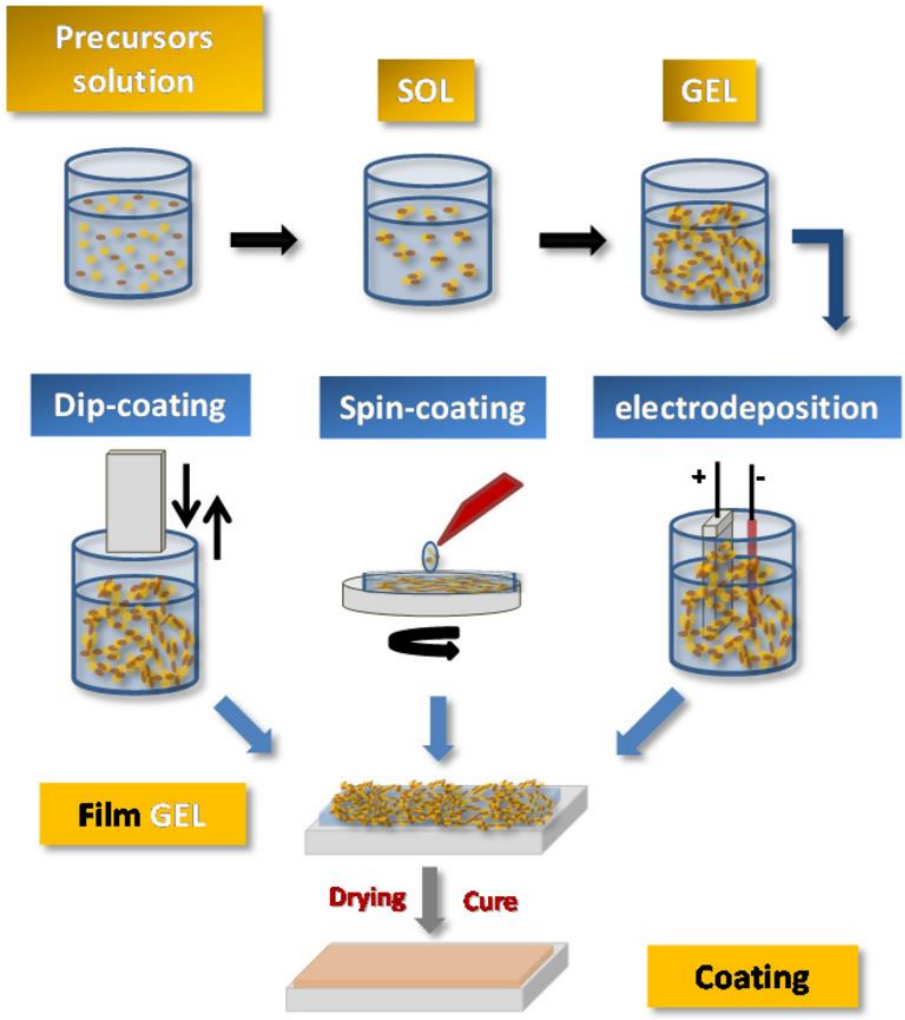

Figure 10. Processing routes to obtain sol-gel coatings. Reprinted with permission from ref. [119]. Copyright © 2016 MDPI.

2.3 Polymer characterization

2.3.1 Gel permeation chromatography

Gel permeation chromatography (GPC) or size exclusion chromatography (SEC) is a powerful tool to characterize synthetic polymers, biopolymers, proteins as well as nanoaggregates. The fundamental principle of GPC relies on the separation of a given polymer or polymer mixture in respect to their hydrodynamic volume. [121] The separation is directly related to the pore size of the porous packing material in the GPC column. Polymers with a smaller hydrodynamic volume can enter these pores more easily and thus, maintain a longer period of time within these pores than polymer with a large hydrodynamic volume. Therefore, each eluted polymer is characterized by a specific retention volume and retention time. A typical chromatogram displays a weight distribution of the polymer or polymer mixture as function of the retention volume, as demonstrated in

Figure 11A. Typically, GPC is used to determine the relative molecular weight and the dispersity (*Đ*) of a given polymer, as illustrated in Figure 11B. Since, GPC requires standards to determine M_w, M_n and M_z, linear polymer standards with narrow MWD such as polystyrene or polymethyl methacrylate are used in order to calibrate the system. An appropriate and careful calibration is crucial to afford reliable and accurate results.

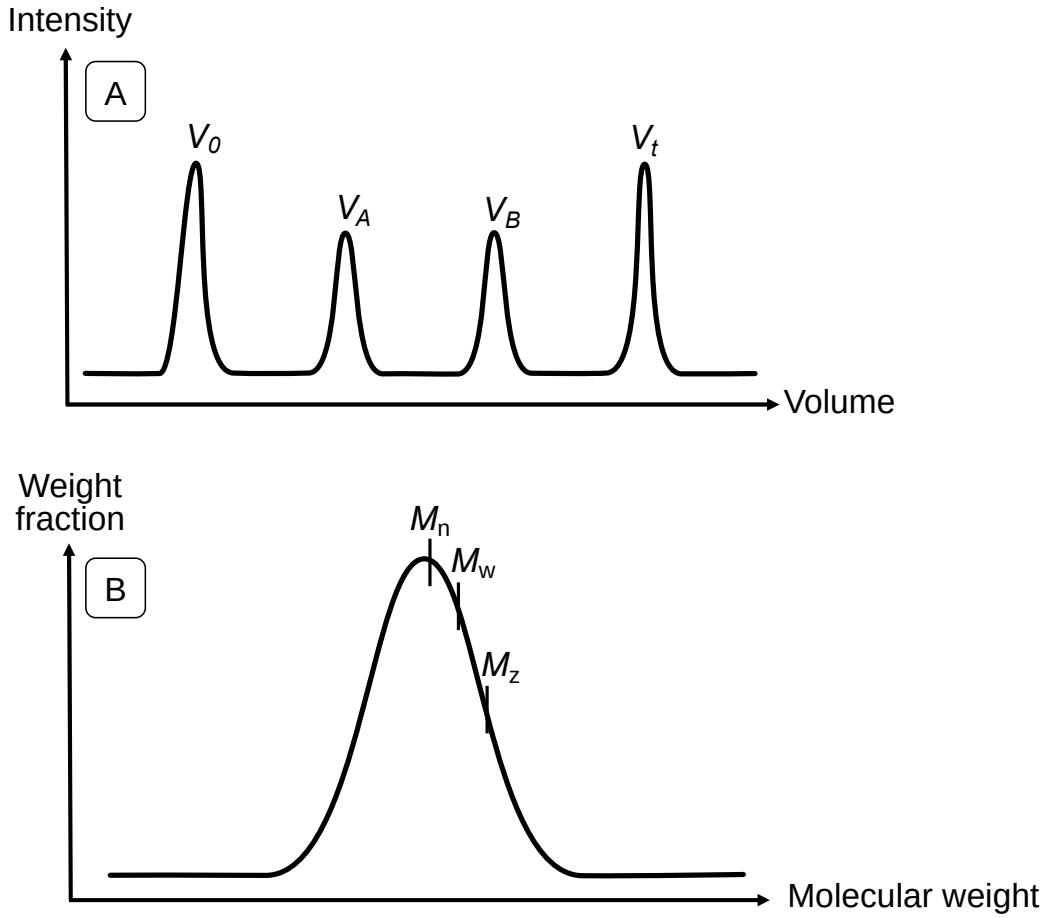

Figure 11. A) GPC Chromatogram of a mixture composed of two polymers A and B, where V_0 = no retention, V_t = complete retention, V_A = retention volume of polymer A and V_B = retention volume of polymer B. B) Illustration of a typical molecular weight distribution of a polymer obtained via GPC analysis, where M_n is the number-average molecular weight, M_w is the weight-average molecular weight and M_z is the Z-average molecular weight.

The basic set-up of a GPC experiment consists of an autosampler, a pump system, one or multiple columns packed with porous packing material as well as one or more detectors, which continuously monitor the concentration by weight of the polymer in the eluting solvent. Commonly employed detectors are concentration sensitive detectors such as UV absorption detectors or refractive index detectors as well as molecular weight sensitive detectors such as light scattering detectors.

2.3.2 Nuclear magnetic resonance spectroscopy

Nuclear magnetic resonance (NMR) spectroscopy is an exceptional powerful tool to characterize polymers in respect to their chemical nature, purity as well as to determine the molecular weight of polymers by using $_1$H NMR spectroscopy. Since, the molecular weight analysis via $_1$H NMR spectroscopy is a primary quantitative method and thus, does not require calibration, it is a fairly simple, fast and accurate method of analysis as compared to GPC. [122] The calculation of the molecular weight of a given homopolymer or copolymer via $_1$H NMR analysis relies on the determination of the degree of polymerization (DP_n) by comparing the relative proton peak intensity of a known moiety (e.g. end-group) to the repeating unit of the polymer. However, this so-called end-group analysis has two major drawbacks: I) The proton signal of the end-group cannot overlap with the proton signal of the polymeric repeating unit. II) This technique is rather limited to low molecular weight polymers of ≤ 25 kDa, due to loss of sensitivity. Thus, end-group analysis is more suited for homopolymers and copolymers of rather short chain length. Since, this doctoral project aims to synthesize (co)polymers of molecular weights of over 25 kDa, end-group analysis method was disregarded as useful method to determine the molecular weight by $_1$H NMR analysis. A second method to calculate the molecular weight of a (co)polymer via $_1$H NMR analysis is to determine the monomer conversion ($conv_{NMR}$) by taking an aliquot from the (co)polymerization mixture. This method allows to calculate the molecular weight for low molecular weight (co)polymers as well as for high molecular is compared with the proton signal of the monomer repeating unit of the polymer. To afford the average *DP* of the (co)polymer the targeted DP_{target} is multiplied with $conv_{NMR}$, as detailed in equation 9.

$$DP_n = DP_{target} \cdot conv_{NMR} \qquad (9)$$

with $$DP_{target} = \frac{[M]_0}{[CTA]_0}$$

Where $[M]_0$ is the initial monomer concentration and $[CTA]_0$ is the initial concentration of the CTA. To maximize the accuracy of the calculation, the polymerization has to be conducted under strict stoichiometric conditions. To calculate M_n of the given polymer, DP_n is multiplied with molar mass of the monomer ($M_{Monomer}$) and summated with the molar mass of the CTA (M_{CTA}), as described in equation 10.

$$M_n = DP_n \cdot M_{Monomer} + M_{CTA} \quad (10)$$

Since, this method is based on the ^{1}H NMR analysis of the crude polymerization mixture, the accuracy of the M_n values is affected by reaction impurities such as oligomers. Consequently, to maximize the accuracy of this method such calculations should be exclusively used for well-defined (co)polymers with narrow MWD. These requirements are fulfilled in the frame of this doctoral project and thus, this method was used as method of choice in order to determine the molecular weight of a polymer via ^{1}H NMR analysis.

2.3.3 Thermogravimetric analysis

Thermogravimetric analysis (TGA), which measures changes in sample weight as a function of increasing temperature allows to investigate particular physical phenomena such as absorption or desorption and chemical phenomena such as decomposition or oxidative degradation. [123] The instrumental requirements for a TGA are a high precision (micro)balance and a furnace that is programmed for a linear increase of temperature with time. In general, TGA is employed in polymer science in order to characterize polymers in respect to their thermal stability and decomposition pattern, as shown in Figure 12.

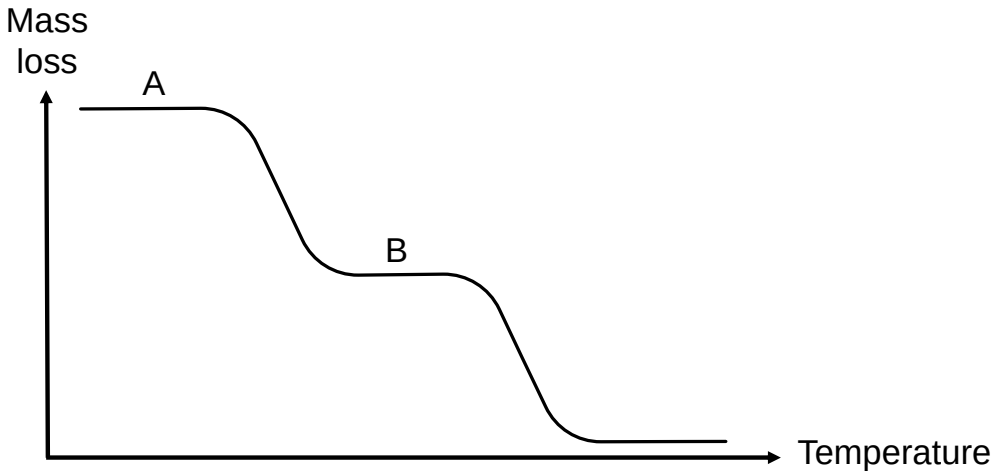

Figure 12. Typical thermogravimetric curve. A and B denote plateaus in the decomposition curve. Adapted with permission from ref. [123].

Thermal decomposition patterns are specific for a particular polymer and thus, allow to investigate the decomposition mechanism of polymers with divergent chemical nature in detail.

2.3.4 Differential scanning calorimetry

Complementary to TGA, the differential scanning calorimetry (DSC) relies on the measurement of the "heat content" as a function of increasing temperature. DSC is used for various applications including characterization of polymers in respect to their phase characteristics or kinetic investigation of isothermal curing processes. There are four different types of DSC namely Heat Flux DSC, Power compensated DSC, Modulated DSC, Hyper DSC as well as Pressure DSC. Nevertheless, the instrumental set-up of all four differ from each other; the experimental results are comparable. DSC is typically used in polymer characterization in order determine particular phase transitions temperatures such as glass-transition-temperatures (T_g), crystallization-temperatures (T_c) and melting-temperatures (T_m), [124] as detailed in Figure 13.

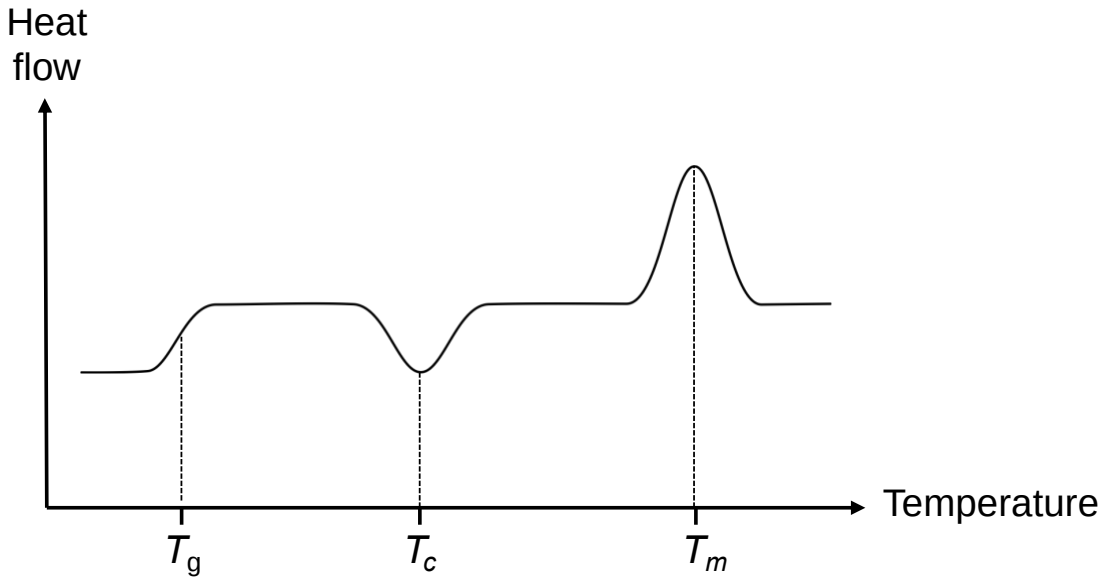

Figure 13. Typical phase transitions of a polymer determined via DSC. Adapted from ref. [124].

2.4 Characterization of thin polymer films on surfaces

2.4.1 Contact angle measurements

Contact angle measurements allow the quantitative measure of wetting of a solid by a liquid. In general, the contact angle (θ) is geometrically described by Young's equation as the angle formed by a spherical liquid droplet at the three-phase boundary, as illustrated in Figure 14. The contact angle is mainly governed by the interfacial tension γ_S, γ_{SL} and γ_L of the three phases. Consequently, a small interfacial tension of the solid-liquid interface ($\gamma_S > \gamma_{SL}$) results in a partial wetting of the solid surface as expressed by contact angle

below 90°. A high contact (>90°) is related to a high interfacial tension of the solid-liquid interface ($\gamma_S < \gamma_{SL}$) and yield partially de-wetted surfaces.

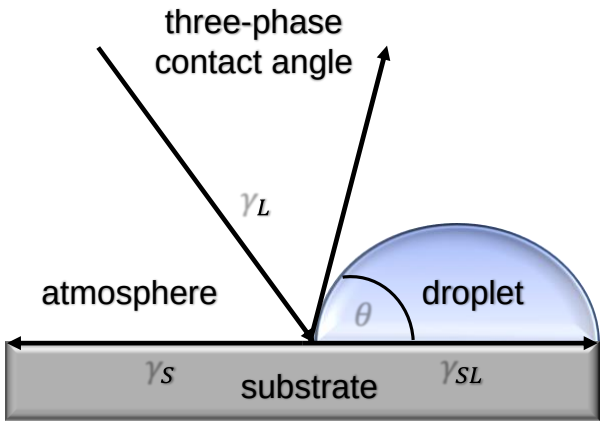

Figure 14. Contact angle of a spherical droplet on the three-phase boundary.

Such measurements give rise to evaluate the surface hydrophilicity or hydrophobicity as well as to investigate wetting and de-wetting phenomena. De-wetted surfaces with a contact angle larger than 135° are ascribed as “superhydrophobic” (total water droplet de-wetting) or “superamphiphobic” (total water and oil droplet de-wetting). Two techniques to determine contact angles are optical tensiometry and force tensiometry. The former technique is the most common one and relies on the measure of images of a droplet placed on the solid surface and subsequent data analysis according to a Young-Laplace-Fit. [125] In addition, the Fowkes-Method [126] and the Owens, Wendt, Rabel and Kaelble (OWRK)-Method [127] enable the calculation of the surface free energies (σ_S) between a solid substrate and a liquid, as detailed in equation 11.

$$\sigma_s = \gamma_{sl} + \gamma_l \cdot \cos\theta \qquad (11)$$

Both methods rely on the assumption that the surface free energy can be divided in a dispersive fraction and non-dispersive fraction, wherein the non-dispersive fraction is further specified in the OWRK-Method as polar fraction. The surface roughness has an immanent impact on the surface wettability and the contact angle. According to Wenzel [128] the wettability of a surface increases with the addition of the surface roughness, as described in equation 12.

$$\cos\theta_m = r \cdot \cos\theta_Y \qquad (12)$$

Where θ_m is the measured contact angle, θ_Y is the Young contact angle and *r* is the roughness ratio. The roughness ratio describes the ratio between the actual and projected solid surface area. For smooth surfaces these values are typically are equal to one ($r = 1$), whereas rough surfaces exhibit larger values of over one ($r > 1$). Notably, the Wenzel model relies on the assumption that the liquid droplet penetrates into the roughness grooves. Contrary to this, Cassie and Baxter developed a model to describe a liquid droplet on a chemically heterogeneous surface, in which the droplet does not penetrate into the roughness grooves. [129] The models derived from the Wenzel and Cassie-Baxter are both approximations and thus, does not apply for every real surface. Due to its ease of operation, contact angle measurements became an invaluable characterization technique in material science.

2.4.2 Atomic force microscopy

Atomic force microscopy (AFM) is a frequently employed high-resolution technique in surface science with a maximum resolution of fractions of a nanometer. AFM enables to characterize a given material surface in respect to its topography as well as nanomechanical characteristics. A typical AFM consists of a spring-loaded nanoscopic needle (cantilever) with a sharp tip, which is carried by a support (leaf), to scan the specimen surface in a pre-defined pattern, as illustrated in Figure 15. The tip is usually composed of silicon or silicon nitride with a curvature of the order of nanometers. In a typical AFM experiment the cantilever tip is brought into proximity of the sample surface, where upon forces between the tip and the sample lead to a deflection of the cantilever following Hook's law. The acting forces including capillary forces, van der Waals forces, mechanical contact forces and chemical bonding during an AFM experiment are strongly dependent on the experimental set-up as well as on the inherent nature of the sample surface. In general, an AFM scan can be operated under three different modes:

I) Contact mode: In contact mode the cantilever tip is dragged through the sample surface and the contours of the sample surface are recorded by using either the deflection of the cantilever or using the feedback signal required to hold the cantilever at a constant position. This mode requires cantilevers with a low stiffness due to the measurement of a static signal and is prone to noise and drift.

II) Tapping mode: At ambient conditions, most samples are enclosed by liquid meniscus layer. Due to this, the cantilever tip is sufficiently close to the sample

surface for short-range forces and thus, allows to detect these forces by preventing the tip from sticking to the surface. In the tapping mode, the cantilever oscillates up and down or near the resonance frequency and the oscillation amplitude is kept constant by applying a constant driving signal. When the cantilever tip is brought sufficiently close to the sample surface, amplitude decreases due to the acting forces between the surface and the tip. Consequently, a topography image is recorded by keeping the force of the intermittent contacts constant by means of an electronic feedback.

III) Non-contact mode: In non-contact mode the cantilever tip is not in contact with the sample surface. Consequently, the change of the resonance frequency is due to attraction-repulsion interactions between the tip and the sample surface. This mode is particularly useful for the investigation of soft tissues such as cells or membranes.

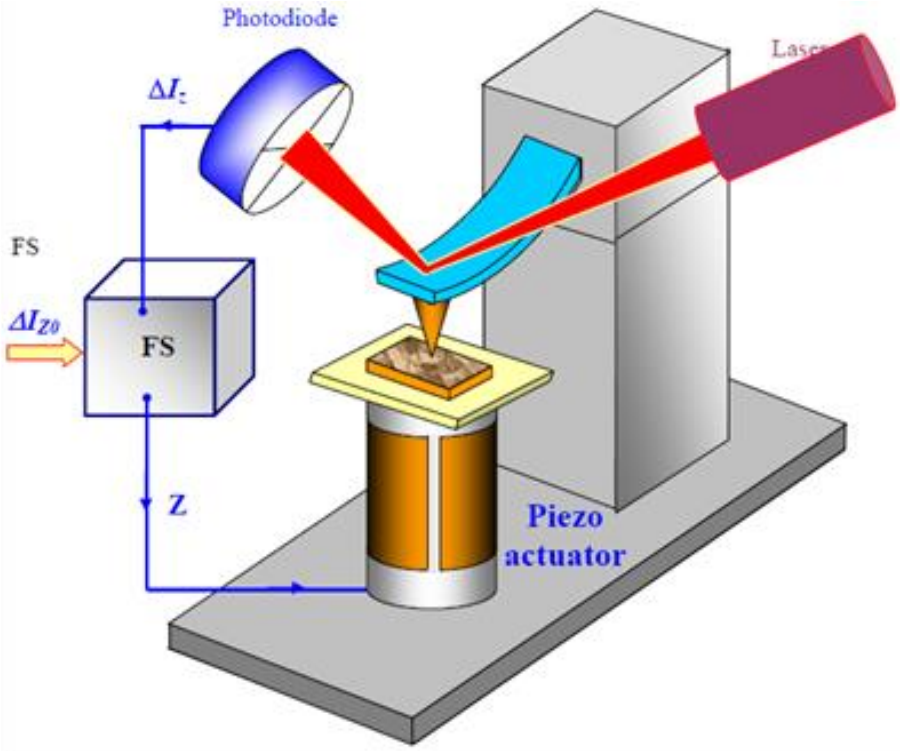

Figure 15. Basic set-up of an AFM equipped with a four-segment photodiode, Piezo actuator and feedback system (FS). The small deflections of the elastic cantilever are recorded by a four-section split photodiode, which transforms the optical signal of the laser beam to an electric signal (ΔI_Z). The ΔI_Z value is directly proportional to the deflection of the elastic cantilever. Reprinted with permission from ref. [130]. Copyright © 2004 V. L. Mironov.

2.4.3 X-ray photoelectron spectroscopy

X-ray photoelectron spectroscopy (XPS) or electron spectroscopy for chemical analysis (ESCA) is a quantitative technique to determine the elemental composition of the surface of a material as well as to determine the binding states of elements. [131] XPS relies on the determination of the kinetic energy spectrum of photoelectrons ejected from the surface of a specimen in vacuum by the irradiating X-way beam having a constant energy, as illustrated in Figure 16. Since the energy of the irradiating X-ray beam is known and the kinetic energy of emitted electrons is measured, the electron binding energy can be calculated by using equation 13.

$$E_{Binding} = E_{Photon} - (E_{Kinetic} + \phi) \qquad (13)$$

where $E_{Binding}$ is the binding energy, E_{Photon} is the energy of the X-ray photons, $E_{Kinetic}$ is the kinetic energy of the electron and ϕ is the work function, which is dependent on the spectrometer and material.

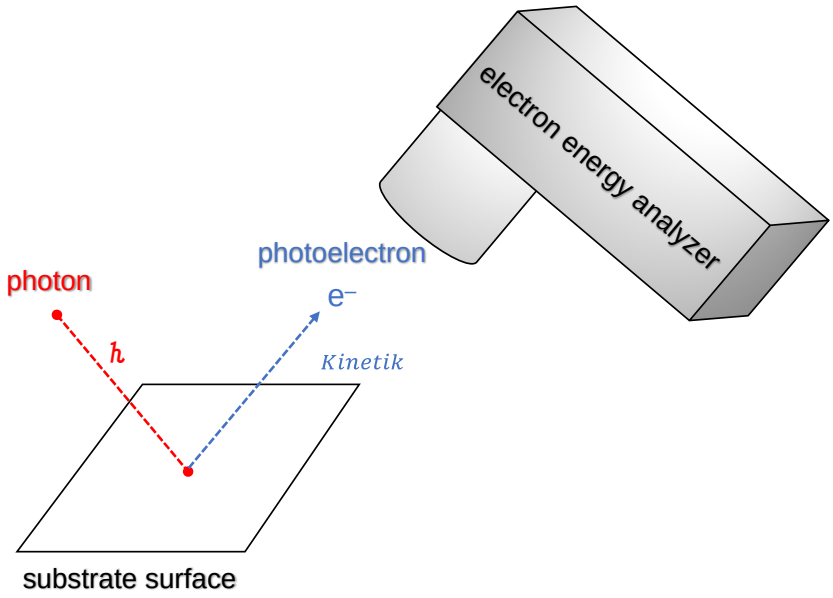

Figure 16. Illustration of the fundamental principle of an XPS measurement.

Due to its sensitivity upon impurities, XPS requires to be operated at ultra-high vacuum conditions in order to minimize the appearance of errors and inaccuracies. With the capability for obtaining quantitative elemental composition, electronic and chemical state and overlayer thickness information from the top ~10 nm of the sample surface, XPS has become one of the most frequently used techniques in academia and industry to characterize thin films.

2.4.4 Infrared reflection absorption spectroscopy

Infrared reflection absorption spectroscopy (IRRAS) is a non-destructive technique for the investigation of thin films adsorbed on reflective substrates such as metals. The fundamental principle of IRRAS relies on the measurement of the change in the reflectance spectrum of the substrate that accompanies adsorption. To enhance the sensitivity, the reflectance spectrum is recorded at grazing incidence of the infrared beam, as illustrated in Figure 17. Due to its high sensitivity, IRRAS allows to investigate thin layers of up to $<10_{-4}$ monolayers. In addition, IRRAS is performed under ambient pressure as compared to electron-based spectroscopy techniques such as XPS and the ease with which its results can be correlated from other vibrational spectroscopies such as ATR-IR spectroscopy. Since, IRRAS requires an IR reflective substrate surface, its rather limited to the investigation of adsorbed thin films on substrate surfaces with high IR reflectivity such as gold or other metals.

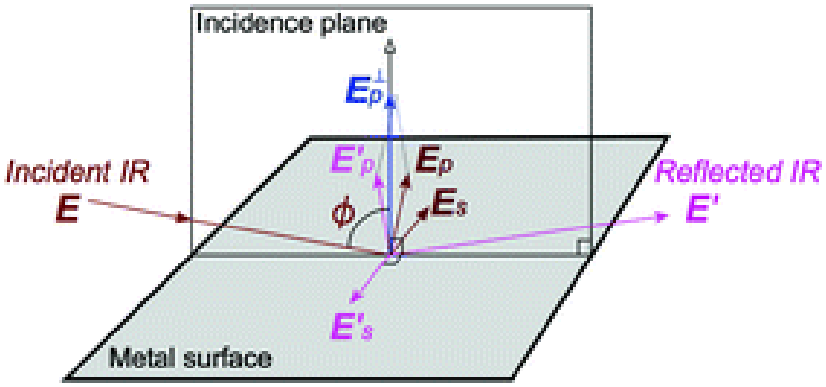

Figure 17. Schematic diagram of reflection of an infrared beam with a grazing angle at a metal surface. Reprinted with permission from ref. [132]. Copyright © 2018 Springer Nature.

Due to its ease of operation and high sensitivity, IRRAS became a very powerful technique to investigate thin polymer films adsorbed on surfaces with high IR reflectivity.

2.5 Micromechanical analysis

In the last decades, fracture mechanics become a powerful tool in material science to improve the performance of materials and engineering components. Fracture mechanics deal with the physics of stress and strain behavior of materials and enable the analysis of the micromechanical characteristics of a material. The fundamental principle of such a micromechanical analysis is to apply a force to a particular material in order to initiate crack propagation within the material matrix or at a material interface. [133] Such crack propagation phenomena can be classified into three primary modes that define the orientation of a crack relative to the stress loading. In general, a crack can be loaded in one mode or in a combination of these modes, as illustrated in Figure 18.

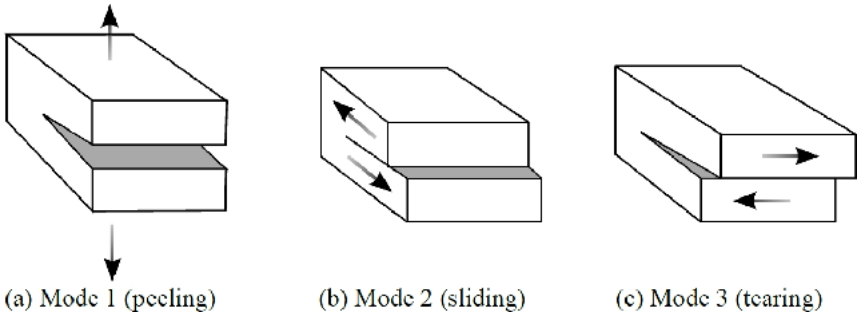

Figure 18. Three primary modes of failure in fracture mechanics. Reprinted with permission from ref. [134]. Copyright © 2017 U. Hirn.

A) Mode I fracture (opening/peeling mode): A tensile stress is applied normal to the plane of the crack.
B) Mode II fracture (sliding mode): A shear stress is applied parallel to the plane of the crack and perpendicular to the crack front.
C) Mode III fracture (tearing mode): A shear stress is applied parallel to the plane of the crack as well as parallel to the crack front.

The most common fracture failure of a material is caused by a Mode I-type crack propagation. Due to this, the micromechanical analysis of engineering components typically considers a Mode I-type crack propagation. In addition, material failures caused by a Mode I fracture are considered as the worst-case situation in the material failure of an engineering component.

3 Objectives

The development of a glass fiber composite material with superior material characteristics requires a rational design principle of the material structure and material boundaries. The inherent material properties and mechanical limitations of the polymer phase (e.g. epoxy) and the reinforcement material (e.g. glass) are essential to develop a deeper understanding of the mechanisms, which govern the material characteristics of a composite material. A commonly employed procedure to improve the mechanical properties of such a glass fiber-based composites are the introduction of an interlayer between the glass phase and polymer phase. For this purpose, low-molecular weight silane coupling agents are employed as adhesives in order to increase the interfacial adhesion between both phases. Nevertheless, this approach is rather limited to a small set of silanes coupling agents and does not allow to control the structure and morphology of the interlayer by means of the used precursor. More sophisticated approaches were developed in order overcome these limitations, in which the low-molecular weight precursors were substituted by polymeric precursors. Such an approach give rise to a new level of spatial control over the interphase structure and thus, enable the preparation of more complex structures and morphologies.
In fact, such modifications are often avoided due to high costs and elaborate procedures. Furthermore, many employed polymers inherently show poor adhesion due to lack of polar functional groups as well as low surface free energy. [135]

Since a plethora of materials encountered in nature are composite materials, nature is a great source of inspiration for engineering and developing new composite materials with superior material properties. Interestingly, such composite materials consist of constituent materials with rather poor material properties that are interconnected through an interphase with excellent spatial control over the interphase structure. Following these observations, a rational design of the interphase is crucial to develop new composite materials with superior mechanical properties.

Thus, the goal of this doctoral project is to develop an adequate polymer-based glass/polyepoxide interphase with a spatially resolved structure in order to improve the adhesion between glass polyepoxide matrix interphase as well as to improve the mechanical properties of a glass/polyepoxide based composite materials, as illustrated in Figure 19. The design of the interphase is inspired by the interphase between tendon and bone, which links two chemically diverse materials with tremendously different elastic moduli. This so-called tendon-to-bone insertion site is mimicked by using novel hybrid

inorganic/organic copolymers with sol-gel active Si-OR moieties. To chemically attach these copolymers to an epoxy matrix and glass surfaces, 2-hydroxyethyl methacrylate (HEMA) is used as epoxy-compatible monomer and 3-(triethoxysilyl)propyl methacrylate (TESPMA) as glass-compatible monomer. Owing to mimic the gradient composition of the tendon-to-bone insertion site, hybrid inorganic/organic block and gradient copolymers are used as precursor to fabricate hybrid sol-gel coatings. Herein, three main challenges have to be tackled: i) Synthesis of well-defined block and gradient hybrid inorganic/organic copolymers composed of TESPMA and HEMA. ii) Fabrication of sol-gel derived hybrid inorganic/organic coatings on glass surfaces. iii) Analysis of the microscopic mechanical properties.

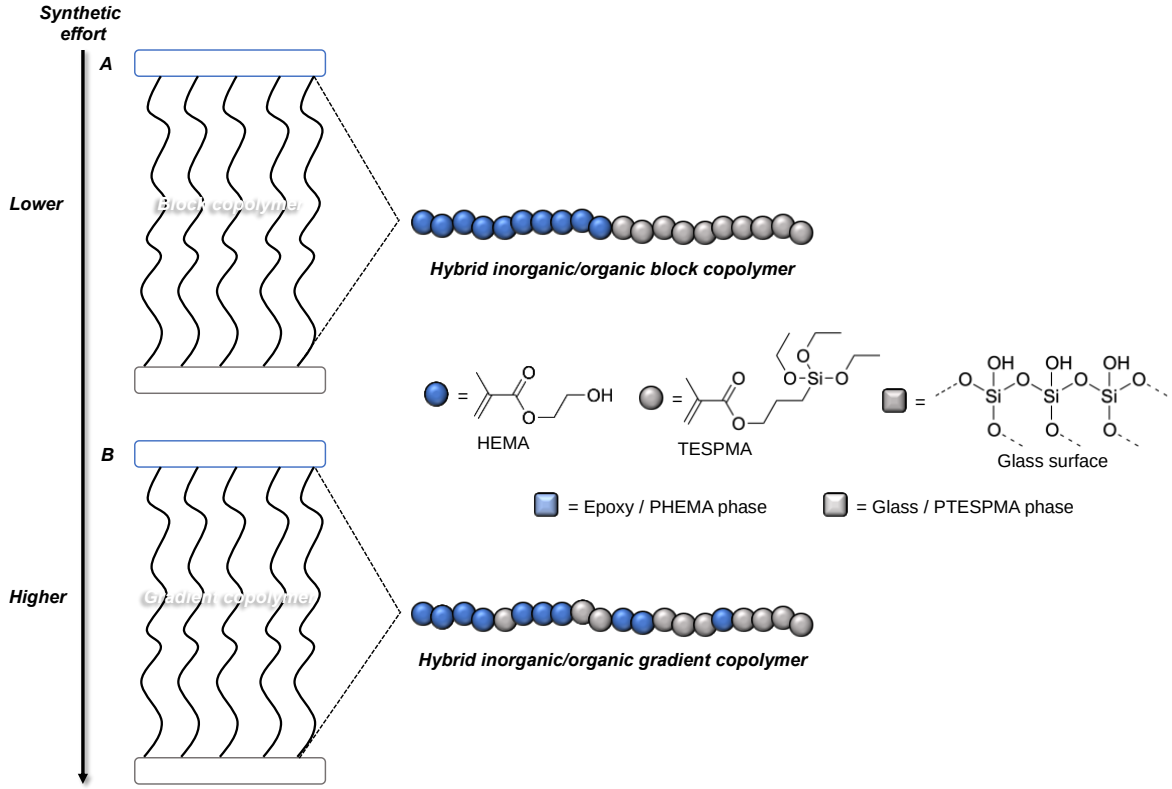

Figure 19. Schematic illustration of two methods to yield an inhomogeneous or gradient distribution of inorganic and organic content in the polymer layer.

I) For the synthesis of well-defined block and gradient hybrid inorganic/organic copolymers with sol-gel active Si–OR moieties RAFT polymerization was chosen due to its ease of operation and reliability. Furthermore, it is envisaged to vary the length of the TESPMA block length in order to control the film thickness of the hybrid coatings as well as to synthesize copolymers with different gradient composition profiles.

II) The fabrication of sol-gel based hybrid inorganic/organic coatings by using a sol-gel grafting-*onto* spin-coating approach. This technique enables the preparation of homogeneous thin polymer films by using sol-gel chemistry. Secondly, the grafting-*onto* approach allows to fully characterize the polymeric precursor in respect of their molecular weight, dispersity and microstructure as compared to a grafting-*from* approach. The hybrid coatings will be characterized in respect of their surface characteristics and structural composition by using common characterization techniques such as AFM, XPS or contact-angle measurements.

III) To correlate the structural characteristics of the interface to the microscopic properties of the composite a simplified glass slide custom-built tensile test shall be developed and used instead of a single-fiber pull-out test. This model-system allows to use glass slides with well-defined polymer layer thicknesses, instead of using coated glass fibers with a heterogenous distribution of polymer layer thicknesses. The micromechanical properties will be evaluated by employing a tensile strength test.

4 Results and Discussion

4.1 Preparation of hybrid inorganic/organic block copolymers

This chapter deals with the synthesis of well-defined hybrid inorganic/organic diblock copolymers composed of 2-tetrahydropyranylethyl methacrylate (THP-HEMA) and 3-(triethoxysilyl) propyl methacrylate (TESPMA) and 3-(triisopropoxysilyl) propyl methacrylate (IPSMA) via RAFT-mediated polymerizations in 1,4-dioxane. The reaction parameters of each polymerization were carefully investigated and evaluated in order to afford diblock copolymers with narrow MWD and precise microstructures. In addition, this chapter includes a brief discussion of the employed protecting group 2-tetrahydropyranyl (THP) group.

4.1.1 Synthesis of THP-HEMA

Owing to synthesize hybrid inorganic/organic copolymers with precise microstructures and narrow MWD a protecting group was introduced to mask the nucleophilic OH functionality of 2-hydroxyethyl methacrylate (HEMA), in order suppress the reaction between nucleophilic OH functionalities and Si-OR functionalities, as displayed in Scheme 6.

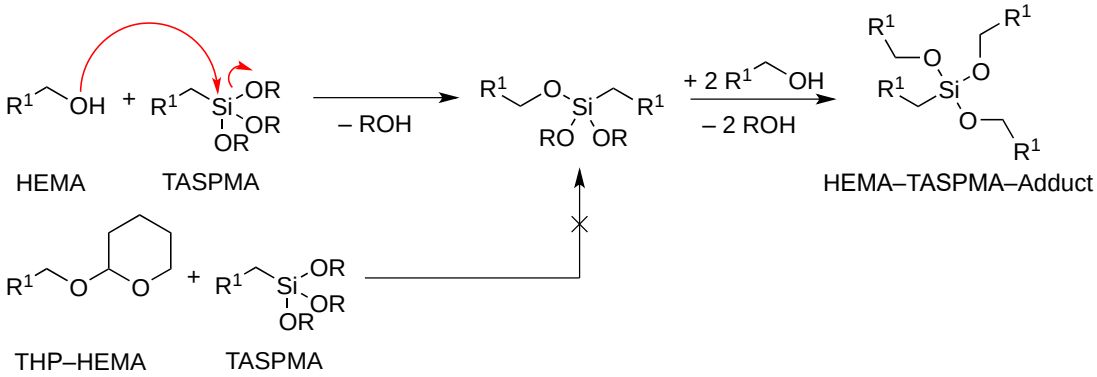

Scheme 6. Proposed mechanism of the HEMA–TASPMA–Adduct formation during copolymerization of HEMA and a TASPMA monomer.

The THP group is a widely used protecting group in chemical synthesis to mask OH containing compounds such as HEMA and can be introduced under various conditions including acid mediated, neutral agent mediated, heterogeneous catalyst mediated as well as miscellaneous. Additionally, THP groups are easily removable under mild acidic conditions. [136] In general, strong acids such as *p*-toluenesulfonic acid (PTSA) require shorter reaction times and lower temperatures than weaker acids such as pyridinium *p*-toluenesulfonate (PPTS) to regain the OH functionality. Previously, HEMA (**1**) was converted with 3,4-dihydro-2*H*-pyrane (DHP, **3**) and PTSA as catalyst to 2-

tetrahydropyranylethyl methacrylate (THP–HEMA, **2**) in diethyl ether at mild reaction conditions. [137-139] However, herein was employed an adapted procedure from Miyashita and co-workers by using using PPTS (**4**) mediated protection of HEMA in dichloromethane at room temperature, as depicted in Scheme 7. [140] The first procedure lead to the formation of ethylene glycol dimethacrylate (EGDMA) as side product, due to the acid catalyzed transesterification of HEMA. This side reaction could be successfully suppressed by employing a milder acid catalyst such as PPTS.

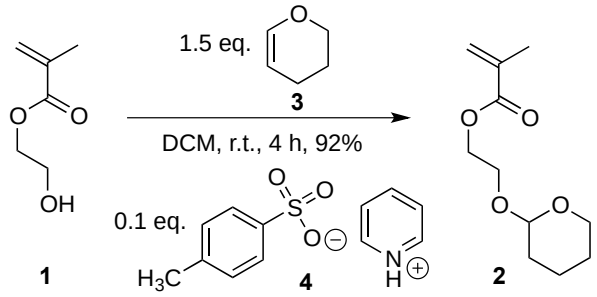

Scheme 7. Synthesis of THP–HEMA.

The general mechanism of the acid mediated THP protection relies on the nucleophilic attack of a OH functionality at a resonance stabilized oxocarbenium-ion, as illustrated in Scheme 8.

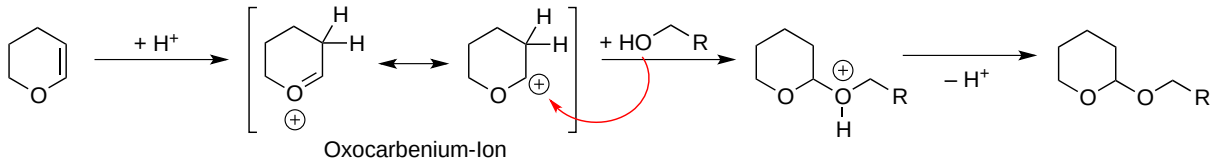

Scheme 8. General mechanism of the acid mediated THP protection of a primary alcohol.

Using the adapted procedure of Miyashita and co-workers, THP–HEMA was synthesized in high purity (> 99%) and high yield of 92%, as shown in the $_1$H NMR spectrum of the final product (see Figure 49, 7.1 Appendix).

4.1.2 Synthesis of P(THP–HEMA)

Schubert *et. al.* reported the synthesis of well-defined THP-HEMA homopolymers and copolymers by using 4-cyano-4-(thiobenzoylthio)pentanoic acid (CBPA) mediated RAFT polymerization in ethanol at 70 °C.[138, 139] Following Schubert's procedure, CBPA as well as 4-cyano-4-[(dodecylsulfanylthiocarbonyl)sulfanyl]pentanoic acid (CDTSPA) were used as CTA, since both CTAs are well suited for the polymerization of methacrylates in a protic polar environment (e.g. ethanol) or a non-protic polar environment (e.g. 1,4-dioxane). The RAFT polymerizations of THP-HEMA were carried out in anhydrous 1,4-

dioxane under various temperatures by using azobisisobutyronitrile (AIBN) as initiator, as shown in Scheme 9. In order to minimize chain end defects and ensure a high chain end fidelity the CTA/initiator ratio was set to four.

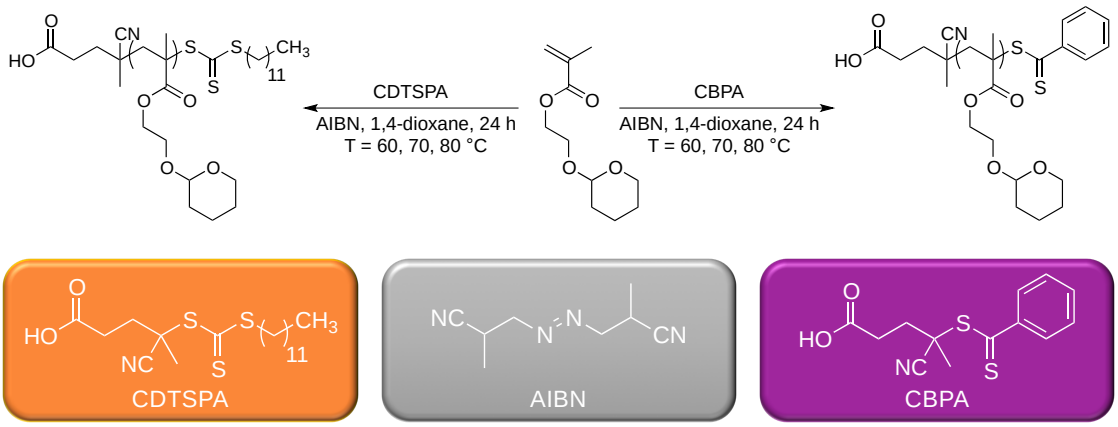

Scheme 9. Synthesis of P(THP–HEMA) via CDTSPA and CBPA mediated RAFT polymerization in 1,4-dioxane at various temperatures.

The obtained homopolymers with a targeted degree of polymerization (DP_{target}) of 100 were characterized according to their molecular weight, dispersity as well as conversions and compared in respect of all of these parameters. For this purpose, molar masses and conversions of homopolymers were estimated according to equation 14 and 15 by ^{1}H NMR analysis.

$$M_n^{NMR} = conv_{NMR} \cdot DP_{target} \cdot M_{Monomer} + M_{CTA} \quad (14)$$

$$conv_{NMR} = \frac{I_{4.6ppm} - I_{6.1ppm}}{I_{4.6ppm}} \quad (15)$$

where $[CTA]_0$ is the initial CTA concentration, $M_{Monomer}$ is the molar mass of the monomer, and M_{CTA} is the molar mass of the CTA. The conversion ($conv_{NMR}$) was calculated by comparing the integral of the polymeric proton signal at 4.6 ppm and the monomeric proton signal at 6.1 ppm, as illustrated in Figure 20. In addition, gel-permeation-chromatography (GPC) was used to determine dispersities and molar masses of the homopolymers, as summarized in Table 2. Both experimental data estimated by ^{1}H NMR analysis and determined by GPC, are summarized in Table 2. The GPC curves in Figure 21 clearly show a loss of control over the polymerization at 70 and 80 °C due to thermal decomposition of CBPA, as indicated by the bimodal distribution of the GPC traces and

an increased dispersity from 1.28 to 1.55 (P5–P6). In contrary, the GPC traces of the CDTSPA mediated RAFT polymerizations exhibit monomodal distributions with dispersities ranging from 1.14 to 1.19, suggesting a higher level of control over the polymerization kinetics under various temperatures. In addition, CDTSPA mediated RAFT polymerizations yielded THP–HEMA homopolymers (P1–P3) with consistently high conversions of over 85%. Comparing both experimental data of both employed CTAs at 60, 70 and 80 °C, CDTSPA-mediated RAFT polymerizations exhibit more consistent experimental data and thus, was used as CTA of choice.

Table 2. Synthesis of P(THP–HEMA) via CDTSPA and CDBPA mediated RAFT polymerizations at various temperatures.

Entry[a]	T (°C)	$conv_{NMR}$ (%)	M_{nNMR} (kDa)	DP_{nNMR}	M_{nGPC} [b] (kDa)	$Đ_b$
P1	60	86.3	18.9	P(THP–HEMA)$_{86}$	17.1	1.14
P2	70	93.3	20.4	P(THP–HEMA)$_{93}$	19.2	1.15
P3	80	91.9	20.1	P(THP–HEMA)$_{92}$	17.3	1.19
P4	60	85.9	18.7	P(THP–HEMA)$_{86}$	20.0	1.13
P5	70	92.0	20.0	P(THP–HEMA)$_{92}$	21.7	1.28
P6	80	81.8	17.3	P(THP–HEMA)$_{82}$	21.7	1.55

[a]Conditions: $[CDTSPA]_0/[AIBN]_0/[THP–HEMA]_0$ = 1/0.25/100 (P1–P3) and $[CBPA]_0/[AIBN]_0/[THP–HEMA]_0$ = 1/0.25/100 (P4–P6). [b]Obtained from GPC relative to linear polymethyl methacrylate standards in THF at 25 °C.

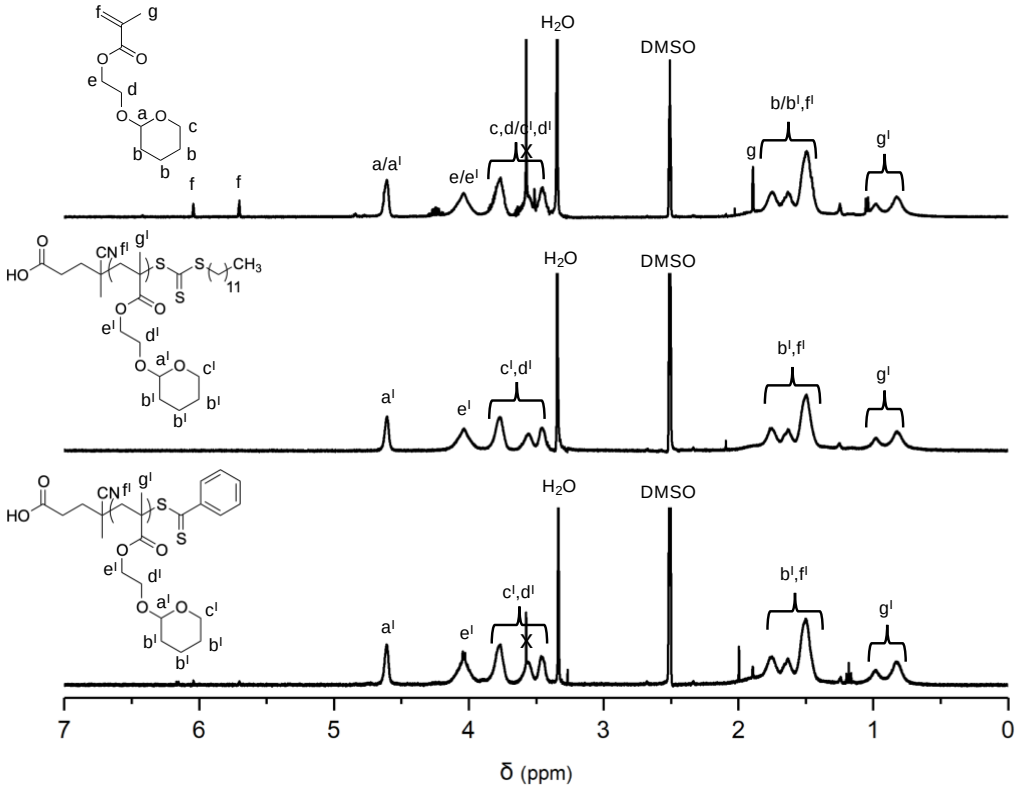

Figure 20. $_1$H NMR spectrum of THP–HEMA and P(THP–HEMA) mixture (top) and P(THP–HEMA) after purification (center and bottom) in DMSO–*d*$_6$.

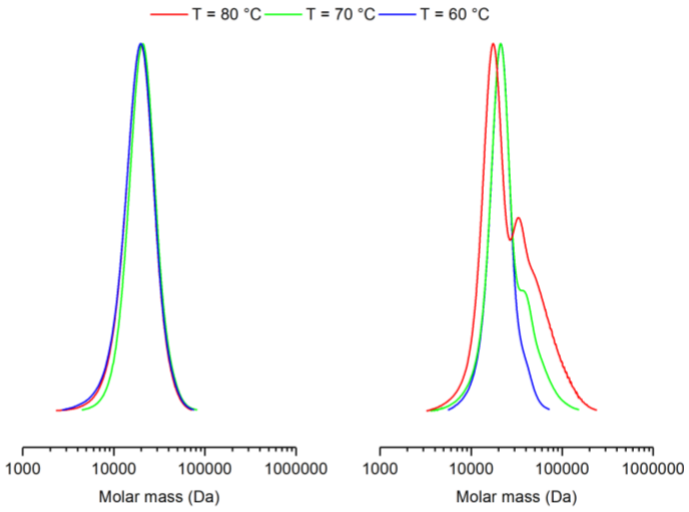

Figure 21. GPC traces of P(THP–HEMA) via CDTSPA mediated (left) and CBPA mediated (right) RAFT polymerizations at various temperatures.

According to the experimental data, the optimal reaction parameter set to afford P(THP–HEMA) with narrow MWD and high molar masses is the CDTSPA mediated RAFT polymerization at 70 °C in 1,4-dioxane (P2). In summary, well-defined P(THP-HEMA)

polymers with molar masses of up to 20.4 kDa and narrow MWD were obtained via CDTSPA mediated RAFT polymerizations in 1,4-dioxane.

4.1.2.1 Acid mediated deprotection of P(THP–HEMA)

In order to remove the pendant THP-groups from the polymer the side chains and to regain the nucleophilic OH functionality, three different deprotection procedures were tested. The deprotection of P(THP–HEMA) was adapted from previously reported procedures, wherein PTSA (pK_a = 0.7), AcOH (pK_a = 4.76) and PPTS (pK_a = 5.21) were used as deprotection agents. The reactions were carried out in protic environments at temperatures ranging from room temperature to 55 °C, as shown in Scheme 10.

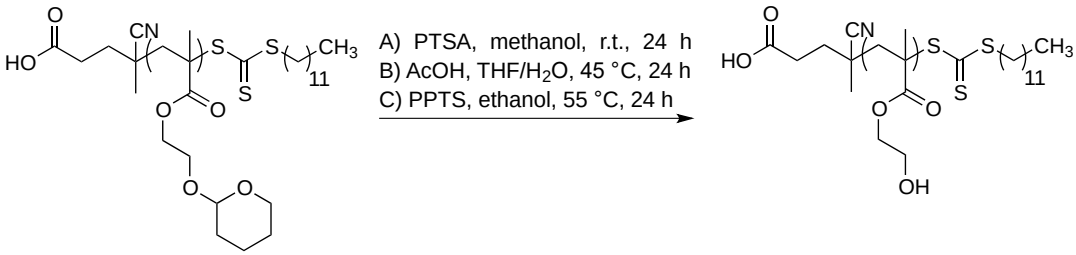

Scheme 10. Acidic deprotection of P(THP–HEMA).

The general mechanism of the acid mediated cleavage of THP ether is based on the nucleophilic ring opening of the pyrane ring under release of 5-hydroxypentanal as side product, as illustrated in Scheme 11.

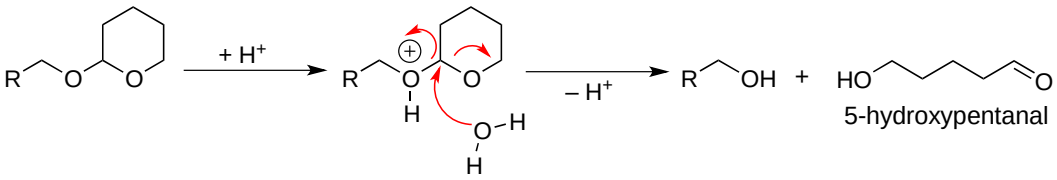

Scheme 11. General mechanism of the THP-ether deprotection.

Deprotection efficiencies of the individual procedures A–C were estimated by $_1$H NMR analysis, as depicted in Figure 22. Deprotection efficiencies were calculated by comparing the peak area of the tertiary proton of the cyclic acetal at 4.6 ppm and the peak area of the appearing OH protons at 4.8 ppm, as detailed in Equation 16.

$$Efficiency = \frac{I_{4.8ppm}}{I_{4.6ppm} + I_{4.8ppm}} \quad (16)$$

According to $_1$H NMR analysis, the PTSA and PPTS mediated reactions show a quantitative deprotection of over 99% efficiency yielding pure PHEMA as pure product after purification. Contrary to these findings, AcOH mediated deprotection exhibit a lower deprotection efficiency of 89% yielding copolymers composed of HEMA and THP–HEMA. Due to the high deprotection efficiency and mild reaction temperatures, the PTSA mediated deprotection was used as method of choice.

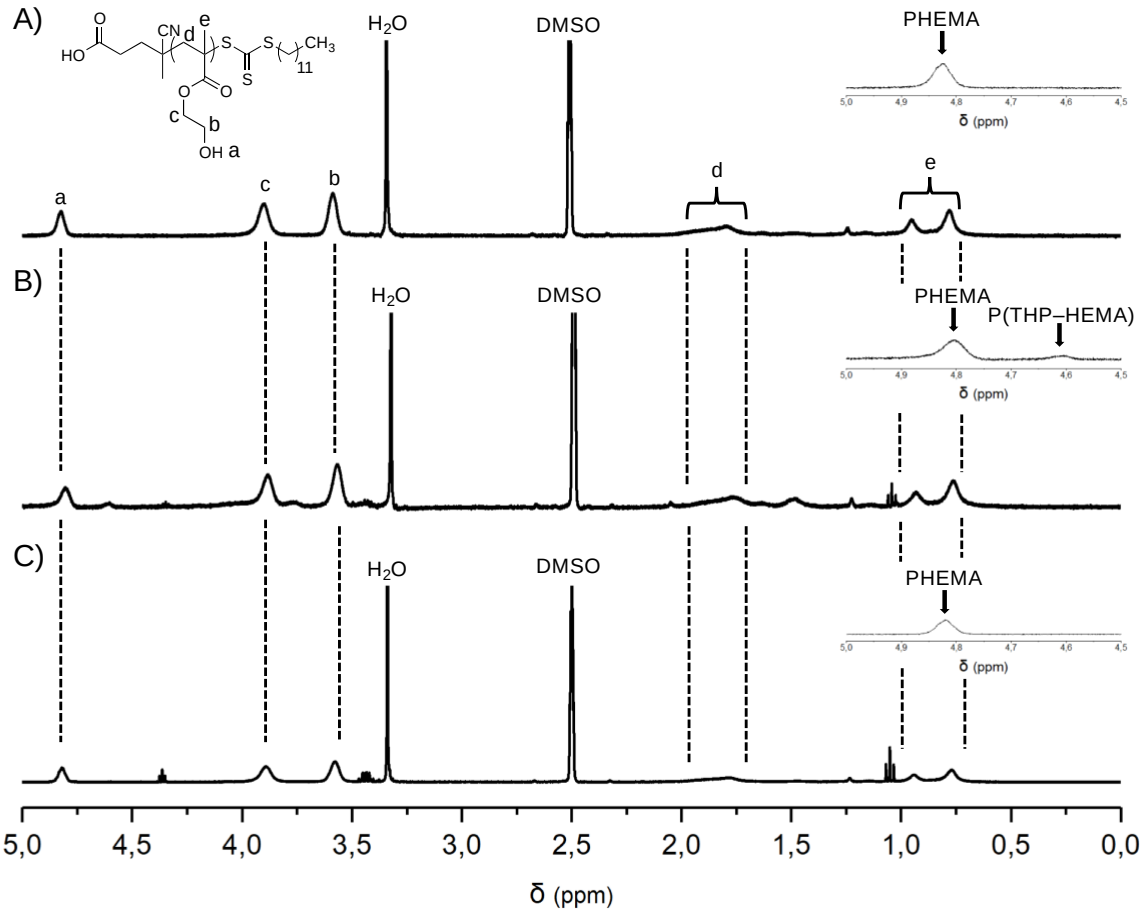

Figure 22. $_1$H NMR spectra in DMSO–d_6 after acid mediated deprotection of P(THP–HEMA). A) PTSA, methanol, r.t., 24 h. B) AcOH, THF/water, 45 °C, 24 h. C) PPTS, ethanol, 55 °C, 24 h.

4.1.2.2 Thermal properties of P(THP–HEMA) and deprotected P(THP–HEMA)

Thermogravimetric analysis (TGA) and Differential Scanning Calorimetry (DSC) were employed to further prove the successful cleavage of the pendant THP-groups and characterize both polymers in respect to their decomposition patterns and phase transition characteristics, as demonstrated in Figure 23.

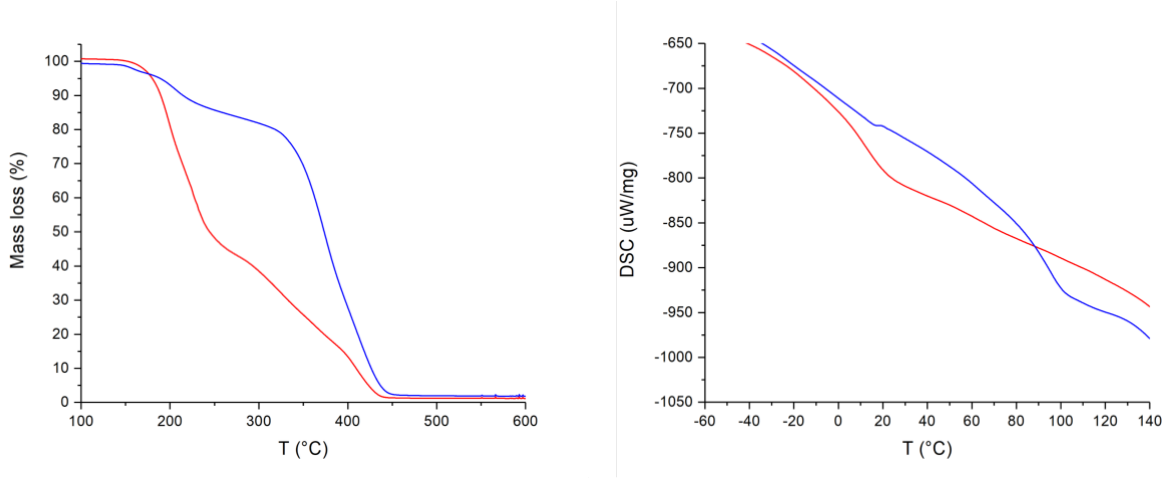

Figure 23. TGA thermograms (left) and DSC curves (right) of P(THP–HEMA) and deprotected P(THP–HEMA). The red curves denote P(THP–HEMA) and the blue curves denote deprotected P(THP–HEMA).

P(THP–HEMA) reveals a two-step degradation pattern. The first degradation-step is observed between 170 °C and 250 °C (~ 50% mass loss), which corresponds most likely to the loss of the pendant THP groups (~ 40% calculated mass loss). The second degradation step occurs between 300 °C and 450 °C, which is attributed to the degradation of PHEMA. These findings are consistent with previously reported data.[138] Deprotected P(THP–HEMA) shows a one-step degradation pattern with a transition between 350 °C and 450 °C, which is consistent with thermal stability studies of PHEMA.[141] The small transition between 220 °C and 250 °C could be attributed to the loss of the long alkyl chain of the RAFT agent chain ends. According to DSC measurements, P(THP–HEMA) exhibits a single T_g at (3.7 ± 1) °C, whereas the glass transition of deprotected P(THP–HEMA) is shifted to higher temperatures giving a T_g t of (79.8 ± 1) °C. The T_g of deprotected P(THP–HEMA) is consistent to the T_g of PHEMA (75 °C).[141] The slightly shift to higher temperatures might be attributed to the nature of the RAFT agent chain ends. These observations are consistent with findings of the ^{1}H NMR analysis and thus, clearly demonstrate the successful and quantitative cleavage of the pendant THP-groups from the polymer side chains.

4.1.3 Synthesis of P(THP–HEMA)-*b*-PTESPMA and P(THP–HEMA)-*b*-PIPSMA

To synthesize hybrid inorganic/organic diblock copolymers (BCP) composed of THP–HEMA, TESPMA (**5**) and IPSMA (**6**) a macroinitiator MacroCTA-approach was used, due to its ease of operation and versatility. For this reason, P2 (M_{nNMR} = 20.4 kDa, $Đ$ = 1.15) was employed as MacroCTA and AIBN as initiator to synthesize P(THP–HEMA)-*b*-

PTESPMA in a controlled fashion, as shown in Scheme 12. The MacroCTA/Initiator ratio was set to two in order to reach a high re-initiation efficiency.

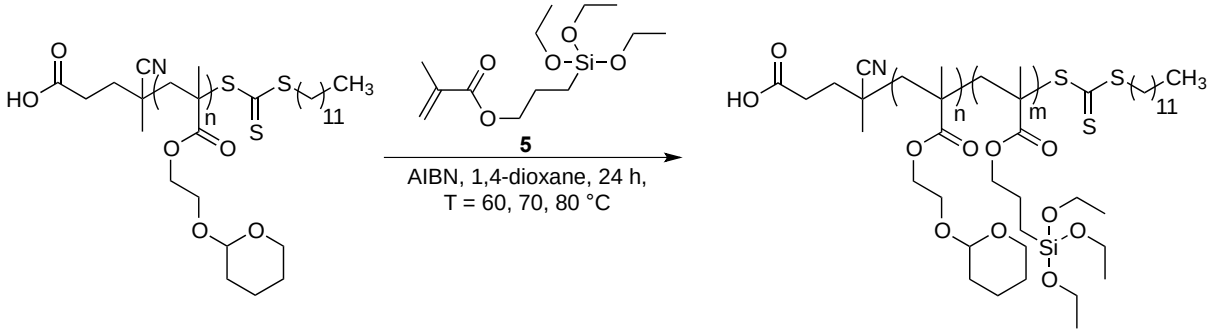

Scheme 12. Synthesis of P(THP–HEMA)-*b*-PTESPMA via MacroCTA mediated RAFT polymerizations at various temperatures.

The molecular weights and conversions of BCP were estimated according via $_1$H NMR analysis, as shown in Figure 24, and calculated by using equation 14 and 17. To study the temperature dependence of the re-initiation efficiency of the MacroCTA mediated RAFT polymerization, the synthesis of BCP1-3 was conducted under 60, 70 and 80 °C in anhydrous 1,4-dioxane.

$$conv_{NMR} = \frac{\frac{I_{0.6ppm}}{2} - I_{6.0ppm}}{\frac{I_{0.6ppm}}{2}} \qquad (17)$$

Table 3. Synthesis of P(THP–HEMA)-*b*-PTESPMA in 1,4-dioxane at various temperatures.

Entry[a]	T (°C)	$conv_{NMR}$ (%)	M_{nNMR} (kDa)	DP_{n+mNMR}	$M_{nGPC\ b}$ (kDa)	$Đ_b$
BCP1	60	92.5	47.2	P(THP–HEMA)$_{93}$-*b*-PTESPMA$_{93}$	46.8	1.25
BCP2	70	92.3	47.1	P(THP–HEMA)$_{93}$-*b*-PTESPMA$_{92}$	37.4	1.37
BCP3	80	90.3	46.5	P(THP–HEMA)$_{93}$-*b*-PTESPMA$_{90}$	44.6	1.94

[a]Conditions: [MacroCTA]$_0$/[AIBN]$_0$/[TESPMA]$_0$ = 1/0.5/100. [b]Obtained from GPC relative to linear polymethyl methacrylate stnadards in THF at 25 °C.

The experimental data of the obtained BCPs are summarized in Table 3. According to $_1$H NMR analysis, the chain extension of the P2 MacroCTA proceeded with high conversions of over 90% at all three temperatures along with dispersities ranging from 1.25 to 1.94.

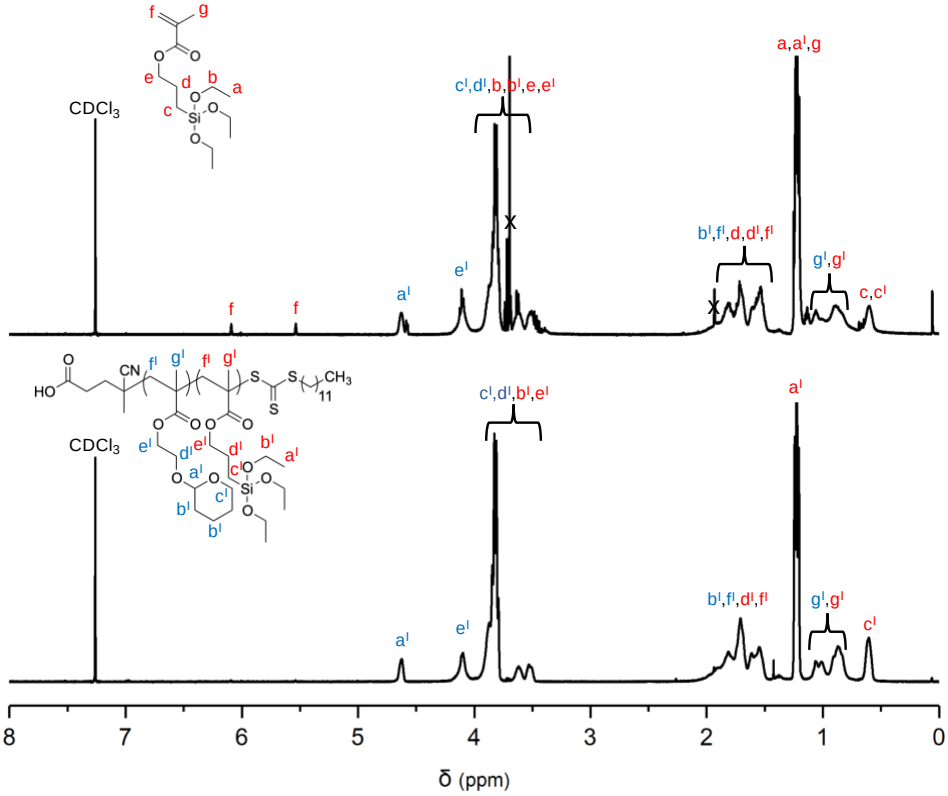

Figure 24. $_1$H NMR spectrum of crude P(THP–HEMA)-*b*-PTESPMA (top) and P(THP–HEMA)-*b*-PTESPMA (bottom) after purification in $CDCl_3$.

The afforded P(THP–HEMA)-*b*-PTESPMA copolymers display a broader MWD by increasing the temperature from 60 °C to 80 °C, as displayed in Figure 25. In addition, BCP3 shows a slight shoulder at higher molar masses, indicating intermolecular crosslinking of the Si-OCH_2CH_3 moieties at higher temperatures. In order to afford BCPs with precise structure and narrow MWD with various TESPMA (**5**) block lengths, the synthesis of BCPs were carried out 60 °C in 1,4-dioxane. In addition, IPSMA based BCPs were synthesized by using the same MacroCTA approach at 60 °C in 1,4-dioxane. IPSMA (**6**) was employed as monomeric precursor, due to its bulkier and more hydrolytically stable Si-$OCH(CH_3)_2$ moieties, as displayed in Scheme 13. Both obtained P3 and P4 block copolymers were synthesized with various TESPMA and IPSMA block lengths of 100, 50 and 25, as listed in Table 4. According to $_1$H NMR analysis the chain extension of P(THP–HEMA)-MacroCTA with TESPMA proceeded with conversions ranging from 88.7% to 92.5% (BCP 4–6), whereas the chain extension of P(THP–HEMA)-MacroCTA with IPSMA achieved conversions ranging from 78.7% to 92.2% (BCP7–9). The overall lower

conversions could be attributed to the higher steric hindrance of the Si-OCH(CH3)2 moieties as well as to impurities within IPSMA.

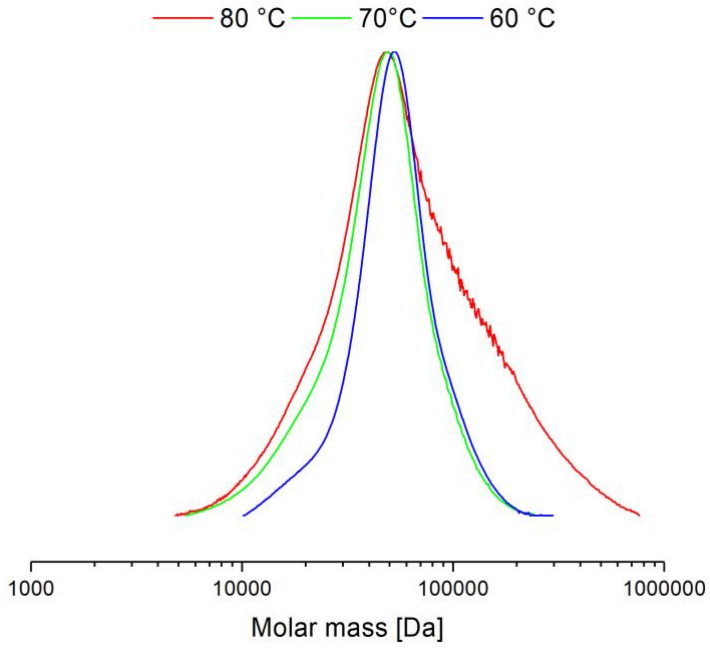

Figure 25. GPC traces of P(THP–HEMA)-*b*-PTESPMA synthesized at various temperatures.

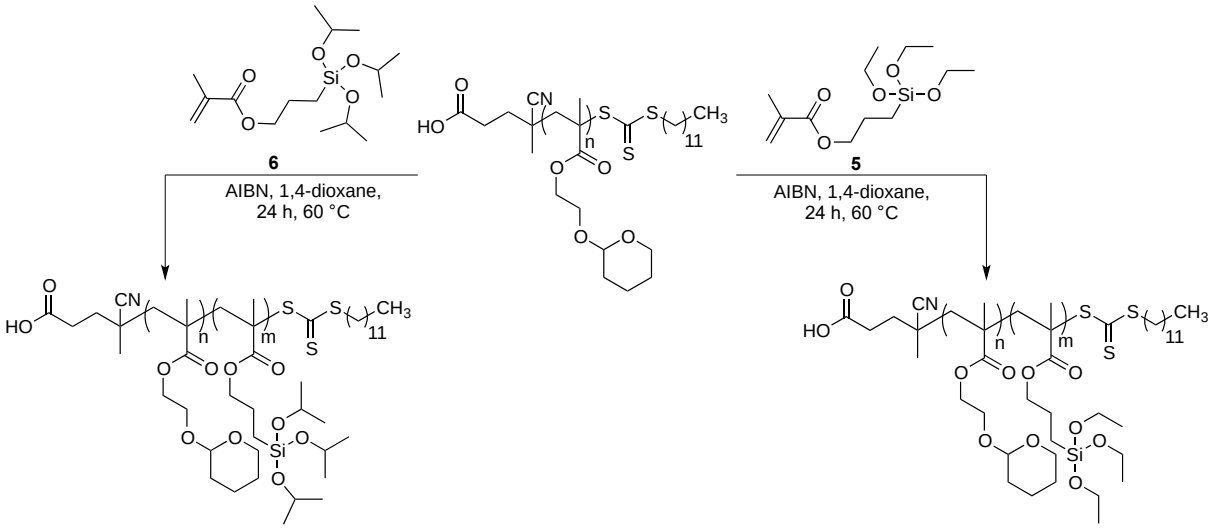

Scheme 13. Synthesis of P(THP–HEMA)-*b*-PIPSMA (left) and P(THP–HEMA)-*b*-PTESPMA (right).

The GPC traces of BCP4-6 and BCP8-9 exhibit a unimodal shape with reasonably narrow MWDs, indicating a high re-initiation efficiency of the P(THP–HEMA)-MacroCTA and overall good control over the polymerization, as demonstrated in Figure 26. BCP6 exhibits

a shoulder at higher molecular masses, indicating intermolecular crosslinking of the pendant Si-OCH2CH3.

Table 4. Synthesis of P(THP–HEMA)-*b*-PTESPMA and P(THP–HEMA)-*b*-PIPSMA in 1,4-dioxane at 60 °C.

Entry[a]	$conv_{NMR}$ (%)	M_{nNMR} (kDa)	DP_{n+mNMR}	M_{nGPC} [b] (kDa)	$Đ_b$
BCP4	92.5	47.2	$P(THP–HEMA)_{93}$-$PTESPMA_{93}$	46.8	1.25
BCP5	90.4	34.3	$P(THP–HEMA)_{93}$-$PTESPMA_{45}$	30.7	1.23
BCP6	88.7	26.8	$P(THP–HEMA)_{93}$-$PTESPMA_{22}$	27.3	1.34
BCP7	78.7	46.6	$P(THP–HEMA)_{93}$-$PIPSMA_{79}$	101.8	4.70
BCP8	92.2	35.7	$P(THP–HEMA)_{93}$-$PIPSMA_{43}$	32.8	1.16
BCP9	80.4	27.2	$P(THP–HEMA)_{93}$-$PIPSMA_{20}$	25.1	1.21

[a]Conditions: $[MacroCTA]_0/[AIBN]_0/[Monomer]_0$ = 1/0.5/100 (BCP4 & BCP7), $[MacroCTA]_0/[AIBN]_0/[Monomer]_0$ = 1/0.5/50 (BCP5 & BCP8), $MacroCTA]_0/[AIBN]_0/[Monomer]_0$ = 1/0.5/25 (BCP6 & BCP9). [b]Obtained from GPC relative to linear polymethyl methacrylate stnadards in THF at 25 °C.

Similarly, BCP9 shows a multimodal peak distribution with a maximum at 100,000,000 Da and two minor peaks between 100,000 Da and 10,000 Da. These observations suggest an inefficient re-initiation of the employed MacroCTA as well as poor control over the polymerization. Furthermore, these observations might be attributed to intermolecular crosslinking of the pendant $Si\text{-}OCH_2(CH_3)_2$ moieties. The intermolecular crosslinking of the sol-gel active Si–OR motifs might be attributed to residual water within the reaction vessel as well as atmospheric moisture during purification, Thus, after purification the BCPs were stored in anhydrous THF at a concentration of 100 mg mL^{-1} in order to inhibit the formation of silica aggregates. In summary, P(THP–HEMA)-*b*-PTESPMA with molar masses ranging from 27.3 kDa to 46.8 kDa with reasonable narrow MWD were obtained by using a two-step MacroCTA approach in 1,4-dioxane at 60 °C. In addition, P(THP–HEMA)-*b*-PIPSMA

with IPSMA block lengths of 20 and 43 exhibits narrow MWD with molar masses ranging from 25.1 kDa to 32.8 kDa. Nevertheless, BCP9 reveals a multimodal MWD as well as ultra-high molar mass of 101.8 kDa. Following these findings, both TESPMA and IPSMA based BCPs were analyzed with TGA in order to test their thermal stability.

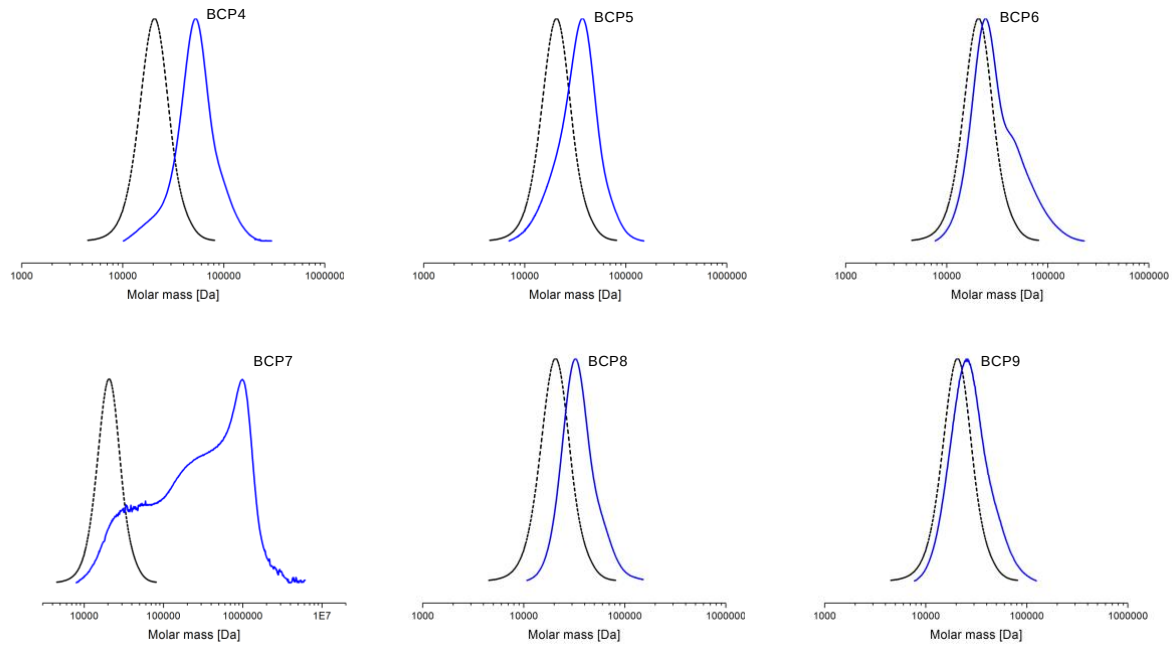

Figure 26. GPC traces of P(THP-HEMA)-*b*-PTESPMA (BCP4–6) and P(THP-HEMA)-*b*-PIPSMA (BCP7–9) with various TESPMA and IPSMA block length. The dashed black GPC traces denote the P(THP–HEMA) MacroCTA.

4.1.3.1 Thermal properties of P(THP–HEMA)-*b*-PTESPMA and P(THP–HEMA)-*b*-PIPSMA

The decomposition patterns and thermal stabilities of the individual TESPMA and IPSMA based BCPS were studied via TGA under a nitrogen flow rate of 30 mL min_{-1} and a temperature range of 25 °C to 600 °C. The TGA curves of the individual TESPMA and IPSMA based BCPs are displayed in Figure 27. In general, all BCPs reveal a two-step decomposition pattern, in which the first decomposition step is associated with the loss of the pendant THP groups. The second decomposition step might be related to the decomposition of the polymer backbone of the organic block segment and the inorganic block segment of the BCPs. Interestingly, the second decomposition step between is shifted to higher temperatures by increasing the TESPMA and IPSMA block length, indicating a higher thermal stability.

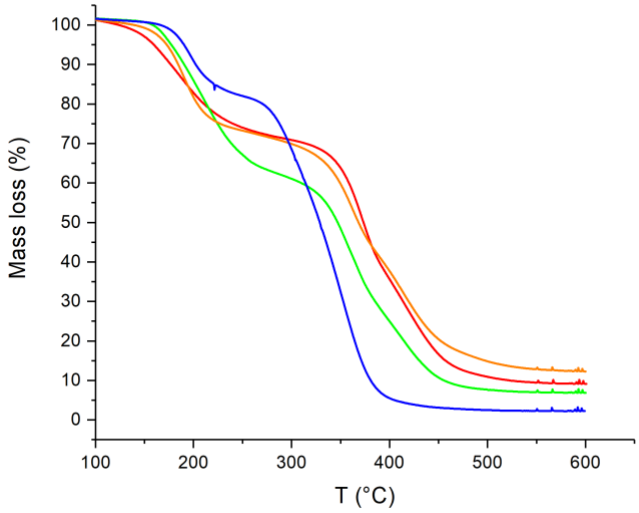

Figure 27. Thermogravimetric analysis of PTHP–HEMA$_{93}$-b-PTESPMA$_{93}$ (red curve), PTHP–HEMA$_{93}$-b-PTESPMA$_{45}$ (green curve), PTHP–HEMA$_{93}$-b-PTESPMA$_{22}$ (blue curve), PTHP–HEMA$_{93}$-b-PIPSMA$_{43}$ (orange curve) and PTHP–HEMA$_{93}$-b-PIPSMA$_{20}$ (violet curve).

These findings are consistent with previously reported thermal stabilities of hybrid inorganic/organic (nano)objects composed of (P)HEMA and SiO_2, the thermal stability of which could be increased by increasing the mole fraction of SiO_2. [142, 143]

4.2 Preparation of hybrid inorganic/organic statistical/gradient copolymers

In the previous chapter the preparation of well-defined THP–HEMA and TESPMA block copolymers by employing a two-step MacroCTA approach was discussed. Since, this technique is limited to the preparation of diblock copolymers and thus, does not allow the synthesis of well-defined gradient copolymers. This chapter includes a detailed description of the synthesis of P(THP–HEMA)-*grad*-PTESPMA by using a semi-batch forced gradient approach. For the preparation of such gradient copolymers, it is advantageous to have a deeper understanding of the copolymers kinetics of the given comonomer system. For this reason, this chapter includes further a detailed description and analysis of the copolymerization kinetics as well as the determination of the reactivity ratios of the THP–HEMA/TESPMA comonomer system.

4.2.1 Synthesis of P(THP–HEMA)-*stat*–PTESPMA and estimation of reactivity ratios

To gain a deeper understanding of the copolymerization kinetics of a given comonomer pair such as THP–HEMA/TESPMA, P(THP–HEMA)-*stat*-PTESPMA copolymers with different molar fractions of THP–HEMA and TESPMA were synthesized. The copolymerization of THP–HEMA and TESPMA was carried out in 1,4-dioxane at 70 °C with different THP–HEMA:TESPMA feed ratios (5:1, 3:1, 1:1, 1:3, 1:5) by employing CDTSPA as CTA and AIBN as initiator, as displayed in Scheme 14. The overall targeted degree of polymerization was set to 100 and the CTA/initiator ratio was set to four in order to minimize the appearance of chain defects. The concentration of the comonomer mixture was set to 1 mmol mL^{-1}. The copolymerization kinetics of THP–HEMA and TESPMA were investigated by using ^{1}H NMR analysis. Therefore, aliquots were taken at given time intervals and analyzed in respect to the monomer conversion, molecular weight and molar composition. The individual monomer conversions of THP–HEMA and TESPMA were estimated by comparing the peak areas of the vinylic protons of THP–HEMA and TESPMA at 6.13 ppm and 6.09 ppm with the polymeric protons of P(THP–HEMA) at 4.6 ppm and PTESPMA at 0.6 ppm, as shown in Figure 28. The individual monomer conversion of THP–HEMA and TESPMA were calculated according to Equation 11 and Equation 11 respectively.

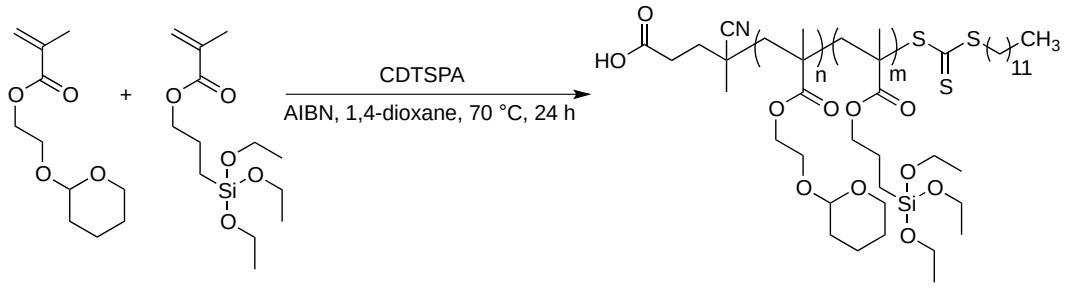

Scheme 14. Synthesis of P(THP–HEMA)-*stat*-PTESPMA.

According to ^{1}H NMR analysis, the copolymerization's with different feed ratios of THP–HEMA and TESPMA proceeded with conversions of 89–97% and 83–95% respectively, as shown in Figure 29. The molecular weights ($M_{n\mathrm{NMR}}$) of the given copolymers were calculated according to equation 18.

$$M_n^{NMR} = (conv_{THP-HEMA}^{NMR} \cdot DP_{THP-HEMA} \cdot M_{THP-HEMA}) + (conv_{TESPMA}^{NMR} \cdot DP_{TESPMA} \cdot M_{TESPMA}) + M_{CDTSPA} \quad (18)$$

where MCDTSPA and MTHP-HEMA/TESPMA are the molecular weights of the CTA and monomers, Conv.THP-HEMA/TESPMA are the individual monomer conversions and DPTHP-HEMA/TESPMA are the targeted degree of polymerization of each monomer.

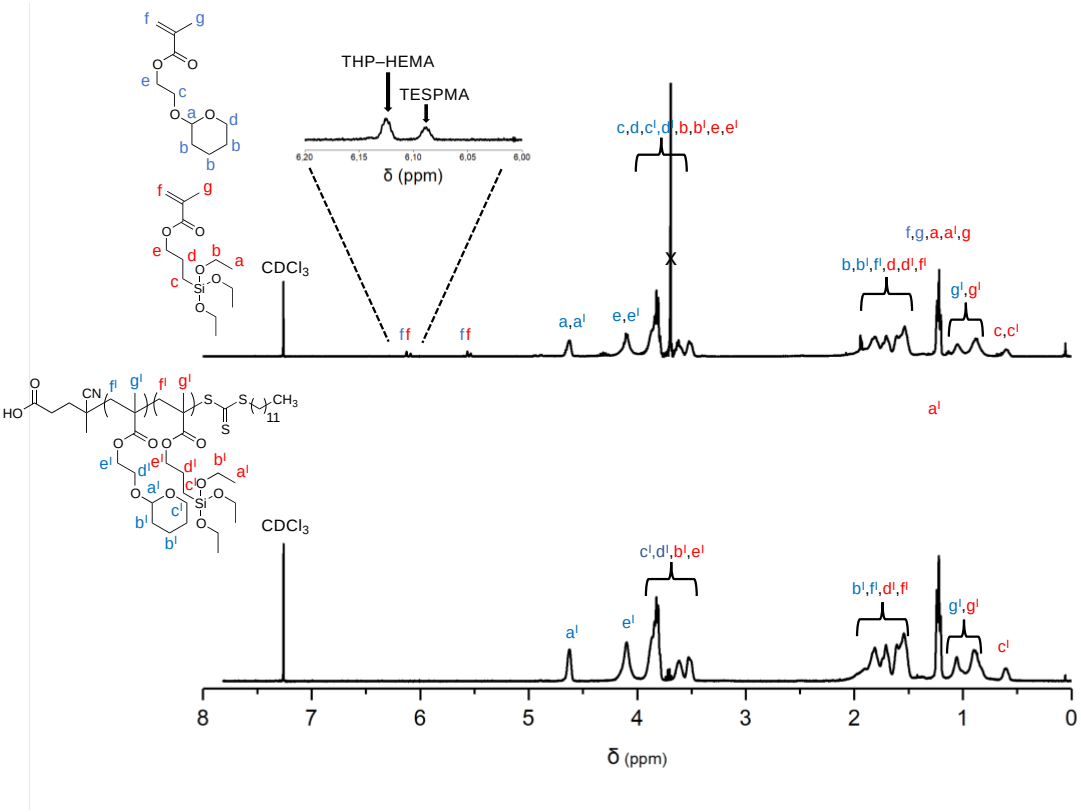

Figure 28. $_1$H NMR spectrum of crude P(THP–HEMA)-*stat*-PTESPMA (top) and purified P(THP–HEMA)-*stat*-PTESPMA (bottom) in $CDCl_3$. The inset shows the vinylic proton signals of THP–HEMA and TESPMA between 6.00 and 6.20 ppm.

The AIBN initiation of propagating chains was neglected as well as the initiation efficiency was set to one. The linear increase of the calculated M_{nNMR} values over the total monomer conversion of the P(THP–HEMA)-*stat*-PTESPMA copolymers clearly demonstrate good control over the copolymerization kinetics, as demonstrated in Figure 30B. These findings are consistent with the linear first order kinetic plots, as displayed in Figure 30C. To assess the effect of the comonomer composition on the polymerization rate, the total monomer conversion was plotted against the reaction time, as shown in Figure 30A. According to these data, the overall monomer conversion decreases from 96% to 86% with increasing molar fraction of TESPMA. This effect might be attributed to a lower rate of propagation of TESPMA as well as increased retardation due to the chemical nature of TESPMA. To qualitatively evaluate the comonomer reactivity of both monomers, the evolution of the monomer composition with total monomer conversion was estimated with $_1$H NMR analysis, as displayed in Figure 31.

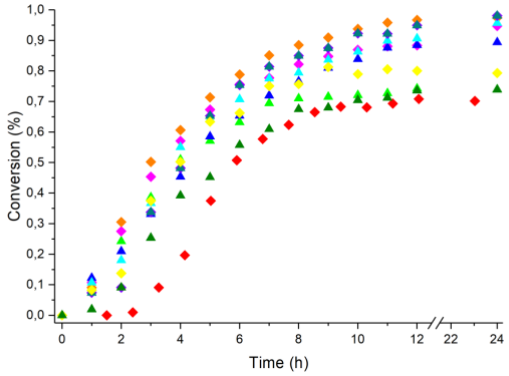

Figure 29. Individual monomer conversions versus time of THP–HEMA (rhombi) and of TESPMA (triangles) at different THP–HEMA/TESPMA feed ratios. Conditions: THP–HEMA:TESPMA (5:1, red), THP–HEMA:TESPMA (3:1, green), THP–HEMA:TESPMA (1:1, blue), THP–HEMA:TESPMA (1:3, orange) and THP–HEMA:TESPMA (1:5, magenta).

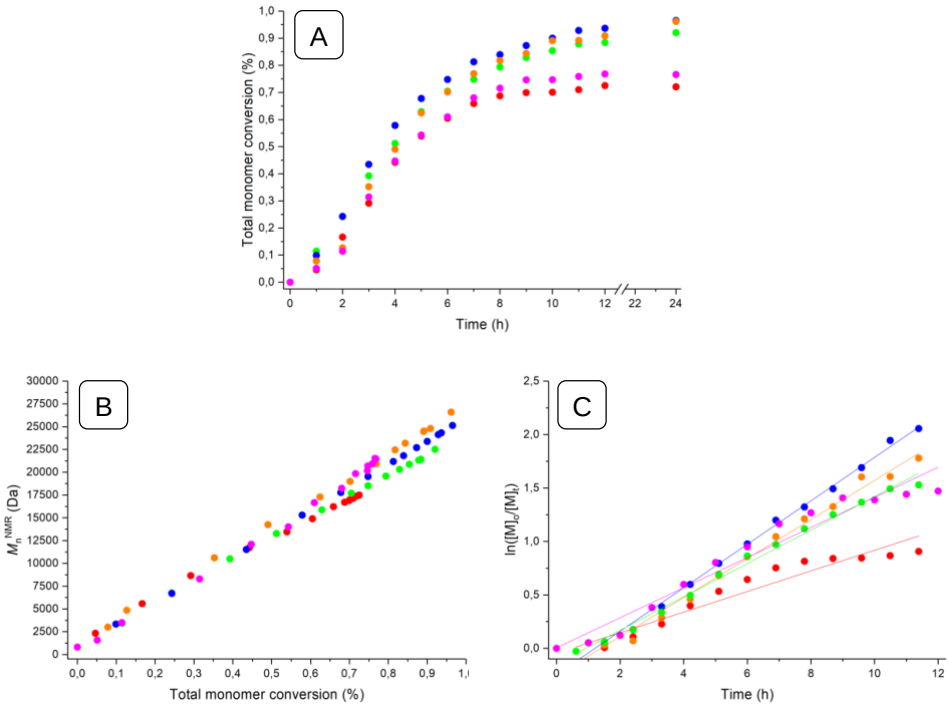

Figure 30. A) Total monomer conversion versus time at different THP–HEMA/TESPMA feed ratios. B) Corresponding plots of the number-average molecular weight (M_n) versus total monomer conversion. C) First order kinetic plots of the copolymerization THP–HEMA/TESPMA at different feed ratios. Conditions: THP–HEMA:TESPMA (5:1, red), THP–HEMA:TESPMA (3:1, green), THP–HEMA:TESPMA (1:1, blue), THP–HEMA:TESPMA (1:3, orange) and THP–HEMA:TESPMA (1:5, magenta).

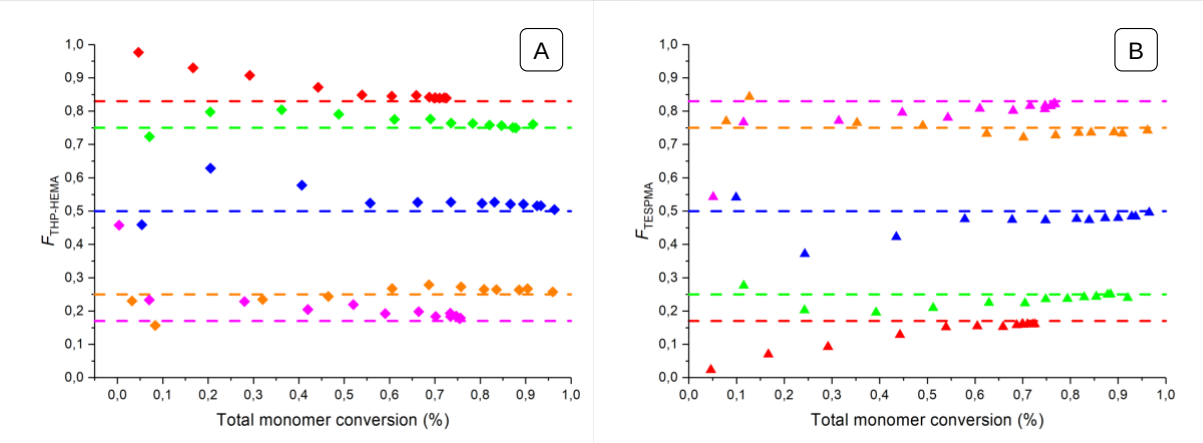

Figure 31. A) Incorporated mole fraction of THP–HEMA ($F_{THP–HEMA}$) versus total monomer conversion at different THP–HEMA/TESPMA ratios. B) Incorporated mole fraction of TESPMA (F_{TESPMA}) versus total monomer conversion at different THP–HEMA/TESPMA ratios. The dashed lines correspond to the mole fractions of THP–HEMA and TESPMA feed. respectively. Conditions: THP–HEMA:TESPMA (5:1, red), THP–HEMA:TESPMA (3:1, green), THP–HEMA:TESPMA (1:1, blue), THP–HEMA:TESPMA (1:3, orange) and THP–HEMA:TESPMA (1:5, magenta).

To obtain the reactivity ratios the experimental data were fitted with a least square nonlinear fit (LSNF), which yield $r_{THP–HEMA}$ = 0.97 and r_{TESPMA} = 1.01 at low conversions as well as $r_{THP–HEMA}$ = 0.99 r_{TESPMA} = 1.04 at medium conversions, as shown in Figure 32. According to the LSNF method, the reactivity ratios of THP–HEMA and TESPMA are equal to one and thus, demonstrating the formation of ideal random copolymers. To verify these findings, the Kelen-Tüdos-Method (KTM) and Extended-Kelen-Tüdos-Method (EKTM) were employed to determine the reactivity ratios of the given monomer pair. Both methods rely on the definition of three new experimental parameters α, ξ and η, which usually results in a more uniform data distribution. The KTM and EKTM parameters are summarized in Table 7 and 8. Due to the similar reactivities of both monomers, the distribution factor α was set to one. To afford the reactivity ratios via KTM and EKTM η was plotted against ξ, as shown in Figure 33. The linear data fit gives $\frac{-r_2}{\alpha}$ as ordinate section ($\xi = 0$) r_1 as slope ($\xi = 1$). [111, 112]

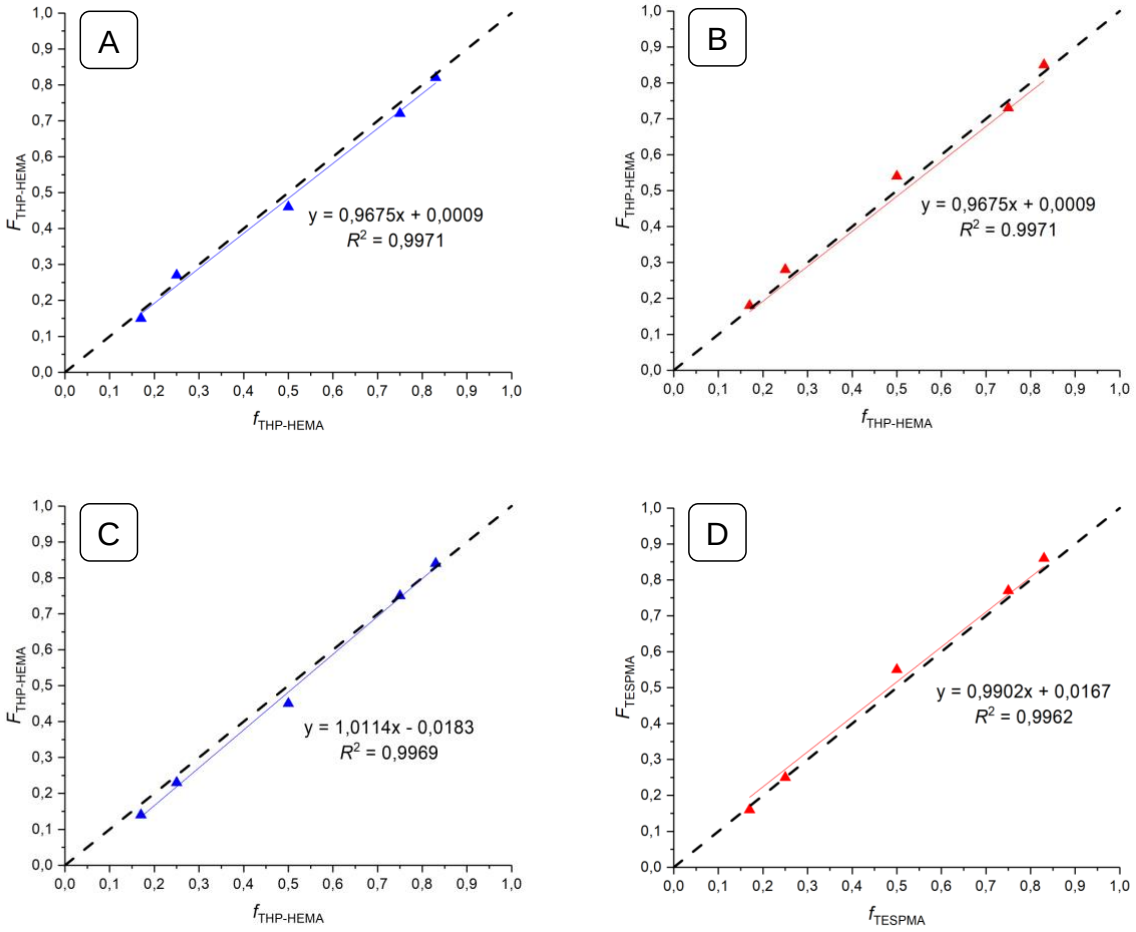

Figure 32. Corresponding plots of the calculated incorporated THP-HEMA fraction ($F_{THP–HEMA}$) versus theoretical THP–HEMA fraction ($f_{THP–HEMA}$) at low conversion (A) and medium conversion (C). Corresponding plots of the calculated incorporated TESPMA fraction (F_{TESPMA}) versus theoretical TESPMA fraction (f_{TESPMA}) at low conversion (B) and medium conversion (D).

According to the KTM and EKTM plot, the reactivity ratios are $r_{THP–HEMA}$ = 1.20 and r_{TESPMA} = 1.16 (KTM) as well as $r_{THP–HEMA}$ = 0.96 and r_{TESPMA} = 0.95 (EKTM). The reactivity ratios derived from the EKTM are in good agreement with the reactivity ratios determined via the LSNF method and thus, verify the formation of ideal random copolymers. Nevertheless, the reactivity ratios determined via the KTM show a slight shift to higher values. This deviation is consistent with previously reports, in which the determination of reactivity ratios at low conversions result in less accurate values due to the nature of the RAFT polymerization. [144-146]

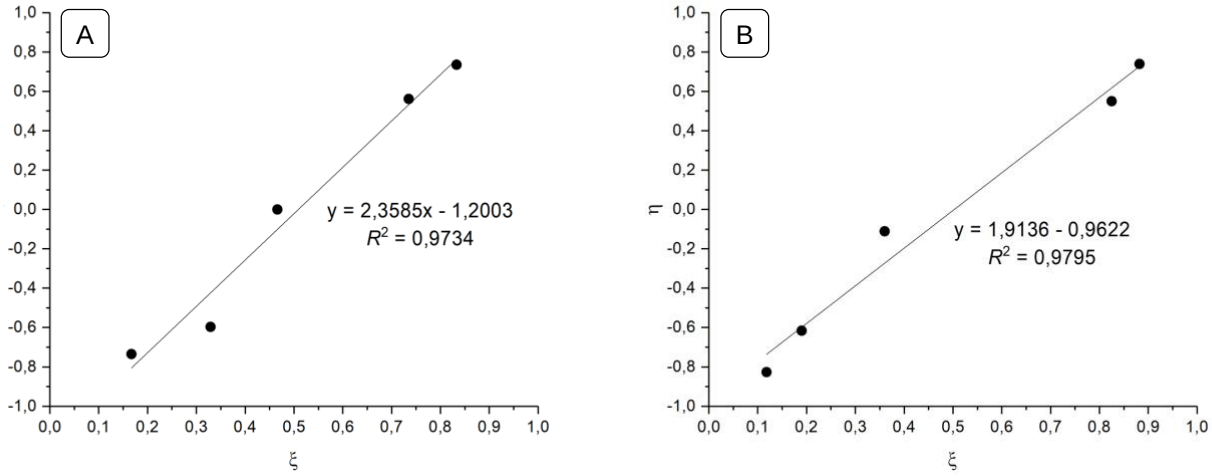

Figure 33. A) Kelen-Tüdos-Plot of the CDTSPA mediated copolymerization of THP–HEMA/TESPMA in 1,4-dioxane at 70 °C. B) Extended-Kelen-Tüdos-Plot of the CDTSPA mediated copolymerization of THP–HEMA/TESPMA in 1,4-dioxane at 70 °C.

Table 5. Estimated molar fractions of THP-HEMA and TESPMA at low monomer conversions.

THP–HEMA:TESPMA	$f_{THP\text{-}HEMA}$	f_{TESPMA}	$F_{THP\text{-}HEMA}$	F_{TESPMA}	$conv_{NMR}$
5:1	0.83	0.17	0.82	0.18	9
3:1	0.75	0.25	0.72	0.28	11
1:1	0.50	0.50	0.46	0.54	10
1:3	0.25	0.75	0.27	0.73	9
1:5	0.17	0.83	0.15	0.85	9

Table 6. Estimated molar fractions of THP-HEMA and TESPMA at medium monomer conversions.

THP–HEMA:TESPMA	$f_{THP–HEMA}$	f_{TESPMA}	$F_{THP–HEMA}$	F_{TESPMA}	$conv_{NMR}$
5:1	0.83	0.17	0.84	0.16	38
3:1	0.75	0.25	0.75	0.25	45
1:1	0.50	0.50	0.45	0.55	34
1:3	0.25	0.75	0.23	0.77	35
1:5	0.17	0.83	0.14	0.86	41

Table 7. KTM parameters for the CDTSPA mediated copolymerization of THP–HEMA and TESPMA 1,4-dioxane at 70 °C.

THP–HEMA:TESPMA	$f = \frac{f_{THP-HEMA}}{f_{TESPMA}}$	$F = \frac{F_{THP-HEMA}}{F_{TESPMA}}$	$G = \frac{F(f-1)}{f}$	$H = \frac{F^2}{f}$	$\xi = \frac{H}{(\alpha + H)}$	$\eta = \frac{G}{(\alpha + H)}$
5:1	5.000	4.530	3.624	4.105	0.833	0.735
3:1	3.000	2.617	1.745	2.284	0.735	0.561
1:1	1.000	0.848	0.000	0.720	0.466	0.000
1:3	0.333	0.367	–0.734	0.404	0.329	–0.597
1:5	0.200	0.182	–0.728	0.166	0.167	–0.735

Table 8. EKTM parameters for the CDTSPA mediated copolymerization of THP–HEMA and TESPMA 1,4-dioxane at 70 °C.

THP-HEMA:TESPMA	$\theta_{THP-HEMA}$	θ_{TESPMA}	$Z = \frac{log(1-\theta_{THP-HEMA})}{og(1-\theta_{TESPMA})}$	F	$G = \frac{(F-1)}{Z}$	$H = \frac{F}{Z^2}$	ξ	η
5:1	0.387	0.375	1.040	5.141	3.984	4.758	0.882	0.739
3:1	0.454	0.454	1.000	3.000	2.000	3.000	0.825	0.550
1:1	0.502	0.367	1.526	0.832	–0.110	0.357	0.360	–0.111
1:3	0.482	0.367	1.437	0.307	–0.482	0.148	0.190	–0.616
1:5	0.502	0.392	1.403	0.166	–0.594	0.085	0.118	–0.827

In summary, the detailed investigation of the CDTSPA mediated RAFT copolymerization of THP–HEMA/TESPMA in 1,4-dioxane at 70 °C revealed the formation of ideal random copolymers. Thus, the incorporated monomer fraction in the polymer chain is equal to the monomer fraction in the comonomer feed. These observations are consistent with the determined reactivity ratios of both monomers, which are close to one. Following these findings, the change of the incorporated monomer fraction can be directly controlled by the change of the comonomer feed during the copolymerization. Thus, a gradual change of the comonomer feed yields copolymers with gradient compositions.

4.2.2 Synthesis of blocky P(THP–HEMA)-*grad*-PTESPMA

Since the batch copolymerization of THP–HEMA and TESPMA yields exclusively ideal random copolymers, the synthesis of gradient copolymers requires the continuous addition monomer B to a mixture of monomer A (feeding) or injection of a pre-defined amount of monomer B to a mixture of monomer A (shot). The latter method yields so-called blocky gradient or tapered copolymers, in which two monomer A-rich and monomer B-rich

segments are interconnected through a mixed block segment with statistical distribution of monomer A and B. Following this many-shot approach, a blocky P(THP–HEMA)-*grad*-PTESPMA copolymer was synthesized by employing the same copolymerization conditions as mentioned in section 4.2.1. To afford blocky gradient copolymers a mixture of THP–HEMA/TESPMA (3:1) was copolymerized in batch for a given time interval and after 3.5 and 7 h to the mixture was injected an 1M TESPMA solution, as demonstrated in Figure 34. Since the conversion of THP–HEMA reached after 3.5 h ~50% and after 7 h ~85%, the first TESPMA shot altered the comonomer feed ratio from 3:1 to ~1:1 and the second shot from 1:1 to ~1:3.

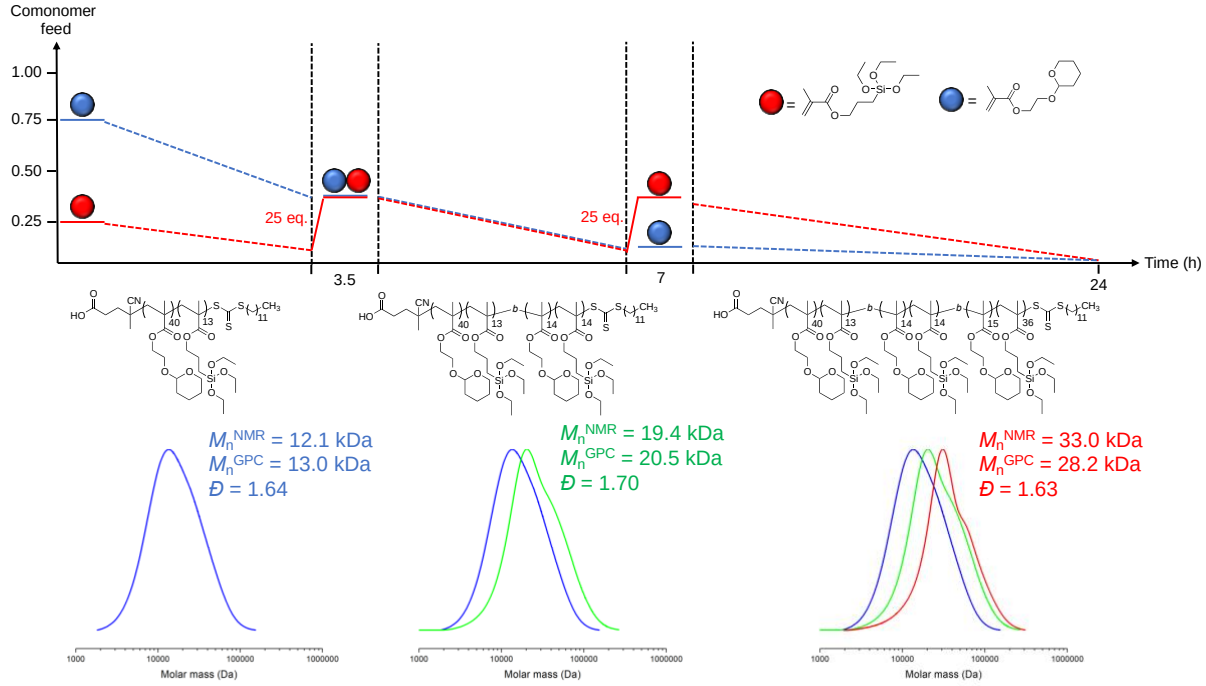

Figure 34. Synthesis of blocky gradient copolymers composed of THP–HEMA and TESPMA via CDTSPA mediated polymerization in 1,4-dioxane 70 °C. Comonomer feed ratio of THP–HEMA/TESPMA over time (top). Composition of the blocky gradient composed of THP–HEMA and TESPMA (center). GPC traces of the blocky gradient copolymer after 3.5 h (blue), 7 h (green) and 24 h (red) (bottom).

According to $_1$H NMR analysis, this two-shot strategy yield a block-like gradient copolymer with a "THP–HEMA-rich" block segment ($F_{THP–HEMA}$ = 0.75, F_{TESPMA} = 0.25), an intermediate block segment ($F_{THP–HEMA}$ = 0.50, F_{TESPMA} = 0.50), and a "TESPMA-rich" block segment ($F_{THP–HEMA}$ = 0.29, F_{TESPMA} = 0.71), as detailed in Table 9.

Table 9. Copolymer composition of blocky P(THP–HEMA)-*grad*-PTESPMA.

"THP–HEMA-rich" block segment		"Intermediate" block segment		"TESPMA-rich" block segment	
$DP_{THP–HEMANMR}$	$DP_{TESPMANMR}$	$DP_{THP–HEMANMR}$	$DP_{TESPMANMR}$	$DP_{THP–HEMANMR}$	$DP_{TESPMANMR}$
40	13	14	14	15	36
(3.1/1)		(1/1)		(1/2.4)	

[a]Conditions: [THP–HEMA]/[TESPMA][CDTSPA]$_0$/[AIBN]$_0$ = 75/25 to 75/1/0.25. The CDTSPA mediated RAFT copolymerization was carried out in 1,4-dioxane at 70 °C.

However, the injection of TESPMA triggered the occurrence of undesired side reactions as indicated by the appearing shoulder at higher molar masses in the GPC traces. These observations might be attributed to different propagation rates of the macroradicals within the copolymerization mixture as well as to an inefficient re-initiation. Since the two-shot strategy results in the formation of blocky gradient copolymers with broadened MWD and less defined microstructures, this technique was disregarded as useful technique to prepare well-defined gradient copolymers composed of THP–HEMA and TESPMA. Thus, the synthesis of hybrid inorganic/organic copolymers was continued by using a semi-batch technique with continuous addition of TESPMA to a mixture of THP–HEMA.

4.2.3 Synthesis of P(THP–HEMA)-*grad*–PTESPMA

The preparation of P(THP–HEMA)-*grad*–PTESPMA (GCP) with smooth gradient microstructures was accomplished by using a semi-batch forced gradient approach, as depicted in Scheme 15. The copolymerization was carried out under similarl conditions as mentioned in section 4.2.1.

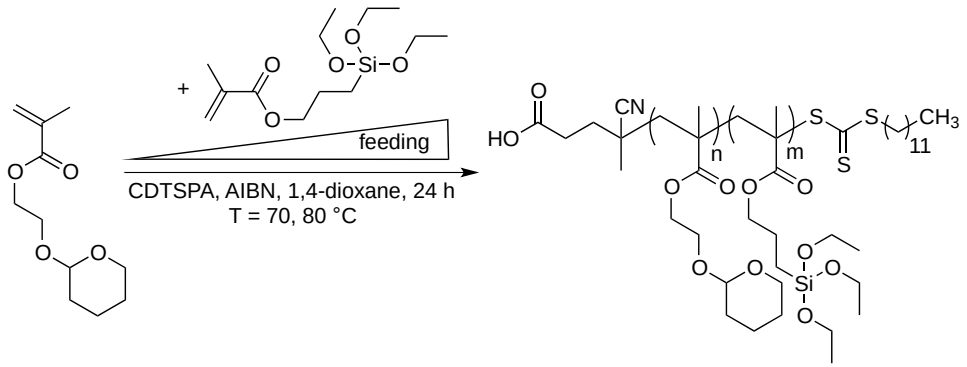

Scheme 15. Synthesis of P(THP–HEMA)-*grad*-PTESPMA by using a semi-batch forced gradient approach.

Since the copolymerization of THP–HEMA and TESPMA exhibits ideal random characteristics, the gradual change from incorporated THP–HEMA to incorporated TESPMA is directly proportional to the comonomer feed ratio of THP-HEMA and TESPMA. Due to these characteristics, the feeding rate of TESPMA governs the formation of rather step gradient microstructures (fast feeding rate) or rather smooth gradient microstructures (slow feeding rate). Following these considerations, the feeding rate of TESPMA was set to 1.0 mL h^{-1} (GCP1, GCP3, GCP5) and 1.5 mL h^{-1} (GCP2, GCP4, GCP6), as summarized in Table 10. To exclude the appearance of concentration dependent retardation phenomena the (co)monomer concentration was set to 1.0 mmol mL^{-1}. The copolymerization kinetics were tracked via ^{1}H NMR analysis as well as GPC analysis and evaluated according to the conversions, molecular weight and dispersity. To assess the polymerization rate of the both monomers, the individual monomer conversions were plotted against the reaction time, as illustrated in Figure 35. The CDTSPA mediated copolymerization of THP–HEMA and TESPMA at 70 °C in 1,4-dioxane with a feeding rate of 1.0 mL h^{-1} (GCP1) and 1.5 mL h^{-1} (GCP2) yielded gradient copolymers with low conversions of TESPMA of 39.2% (GCP1) and 65.3% (GCP2) and sufficiently high conversions of THP–HEMA 74.6% (GCP1) and 83.2% (GCP2).

Table 10. Reaction conditions for the synthesis of P(THP–HEMA)-*grad*-PTESPMA via CDTSPA mediated RAFT polymerization.

Entry[a]	T (°C)	feeding rate (mL h^{-1})	$V_{1MTESPMA}$ (mL)	feeding time (h)
GCP1	70	1.0	7.5	7.5
GCP2	70	1.5	7.5	5.0
GCP3	70	1.0	7.5	7.5
GCP4	70	1.5	7.5	5.0
GCP5	80	1.0	7.5	7.5
GCP6	80	1.5	7.5	5.0

[a]Conditions: $[MacroCTA]_0/[AIBN]_0/[THP–HEMA]_0/[TESPMA]_0$ = 1/0.25/75/0 to 75 (GCP1–2), $[MacroCTA]_0/[AIBN]_0/[THP–HEMA]_0/[TESPMA]_0$ = 1/0.25 to 0.5/75/0 to 75 (GCP3–6).

The slow polymerization rates suggest an inefficient re-initiation of the propagating macroradicals, which might be attributed to the occurrence of side reactions (retardation) or a low concentration of radicals within the copolymerization mixture. Since the

concentration of radicals in RAFT is directly related to the concentration of initiator as well as to the decomposition rate of the initiator.

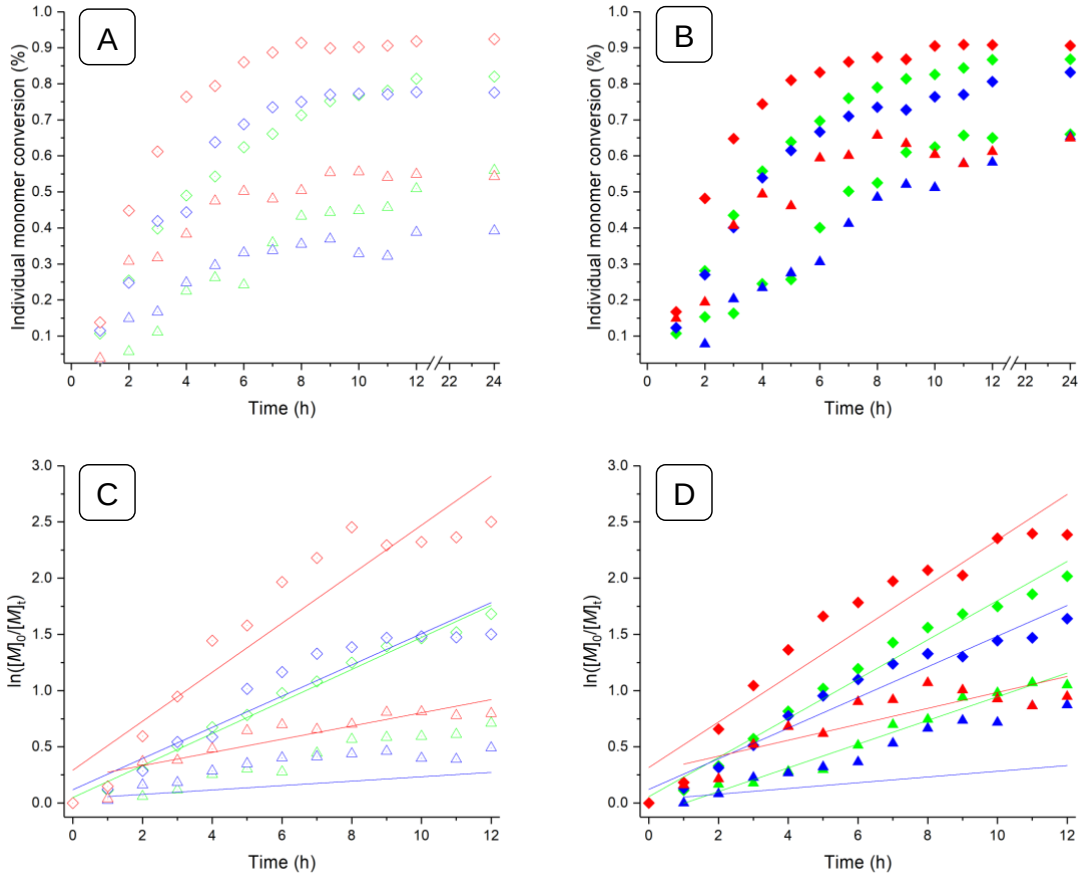

Figure 35. A & B) Individual monomer conversions versus time with a TESPMA feeding rate of 1.0 mL h_{-1} (open symbols) and 1.5 mL h_{-1} (closed symbols). C & D) First order kinetic plots of the copolymerization of THP–HEMA/TESPMA with continuous addition of TESPMA. The triangles denote TESPMA and rhombi denote THP–HEMA. Conditions: $[CDTSPA]_0/[AIBN]_0$ = 1/0.25, 1,4-dioxane, 70 °C (blue); $[CDTSPA]_0/[AIBN]_0$ = 1/0.25 to 0.5, 1,4-dioxane, 70 °C (green); $[CDTSPA]_0/[AIBN]_0$ = 1/0.25 to 0.5, 1,4-dioxane, 80 °C (red).

The concentration of radicals can be increased via addition of more initiator or/and higher reaction temperatures, which results in a faster decomposition of the initiator. Following these assumptions, the copolymerization of THP–HEMA and TESPMA was carried out at 70 °C in 1,4-dioxane with continuous addition of AIBN (GCP3 and GCP4). Thus, the initial CTA/Initiator ratio was altered from four to two with increasing amount of TESPMA in the comonomer feed. GPC3 and GCP4 exhibit a slightly increased rate of polymerization as indicated by the slopes the first order kinetic plots in Figure 35C and 35D. In addition, the

individual monomer conversions of TESPMA slightly increased from 39.2% to 56.0% (GCP3) and from 65.3 to 66.7% (GCP4). To further increase the concentration of radicals within the reaction, the reaction temperature was increased from 70 °C to 80 °C (GCP5 and GCP6). These conditions yielded gradient copolymers with higher THP–HEMA conversions of 92.4% (GCP5) and 90.6% (GCP6). Interesting, the TESPMA conversions of GCP5 and GCP6 are similar to the TESPMA conversions of GCP3 and GCP4. A higher concentration of radicals within the copolymerization mixture results in a higher number of termination events and thus, can compromise the rate of polymerization at higher conversions as well as yield copolymers with a broadened MWD. To assess the former hypothesis, the overall monomer conversion was plotted versus the reaction time, as demonstrated in Figure 35. According to these plots, GCP5 and GCP6 exhibit a slowdown of the polymerization rate at a conversion of 73.4% and at a conversion of 77.3% respectively as indicated by a plateau after 9 h. This plateau is presumably attributed to the occurrence of termination events such as radical coupling or chain dependent retardation. Compared to both former mentioned GCPs, GCP1–4 exhibit an increase of conversion even after 24 h, but with an overall slower rate of polymerization as compared to GCP5 and GCP6.

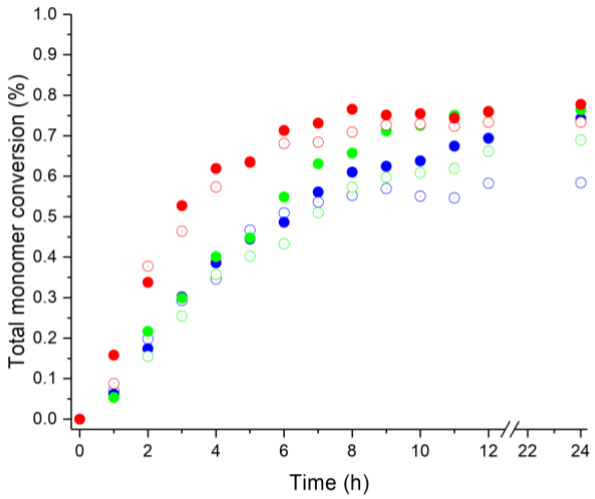

Figure 36. Total monomer conversion versus time with a TESPMA feeding rate of 1.0 mL h^{-1} (open symbols) and 1.5 mL h^{-1} (closed symbols). Conditions: $[CDTSPA]_0/[AIBN]_0$ = 1/0.25, 1,4-dioxane, 70 °C (blue); $[CDTSPA]_0/[AIBN]_0$ = 1/0.25 to 0.5, 1,4-dioxane, 70 °C (green); $[CDTSPA]_0/[AIBN]_0$ = 1/0.25 to 0.5, 1,4-dioxane, 80 °C (red).

To further investigate the copolymerization kinetics of GCP1–6 was employed GCP analysis and compared with the ^1H NMR data, as displayed in Figure 37 and Table 11. According to the GPC analysis, the gradient copolymers show a reasonable narrow MWD

with dispersities ranging from 1.40 to 1.69. The molar masses of the corresponding copolymers increase linearly with increasing conversion and thus, indicating a good control over the reaction kinetics, as shown in Figure 37A and 37B. Notably, the higher concentration of radicals within the copolymerization mixture (GCP3–6) do not yield copolymers with a broader MWD as compared to GCP1 and GCP2. These findings clearly demonstrate, that the continuous addition of AIBN during the copolymerization does not compromise the overall control over the copolymerization. Consequently, the addition AIBN enable the synthesis of gradient copolymers with higher molecular weights of 27.1kDa (GCP5) and 29.1 kDa (GCP6) compared to 23.4 kDa (GCP1) and 28.0 kDa (GCP2). The discrepancies between the M_{nNMR} and M_{nGPC} are due to employed GPC calibration against PMMA.

Table 11. Synthesis of P(THP–HEMA)-*grad*-PTESPMA via CDTSPA mediated RAFT polymerization under various experimental conditions.

Entry[a]	$conv_{NMR}$ (%)	M_{nNMR} (kDa)	DP_{n+mNMR}	M_{nGPC} [b] (kDa)	$Đ$[b]
GCP1	58.4	23.4	$P(THP–HEMA)_{58}$-$PTESPMA_{29}$	17.0	1.69
GCP2	74.2	28.0	$P(THP–HEMA)_{62}$-$PTESPMA_{49}$	15.6	1.40
GCP3	69.0	25.8	$P(THP–HEMA)_{61}$-$PTESPMA_{42}$	16.0	1.40
GCP4	76.4	28.7	$P(THP–HEMA)_{65}$-$PTESPMA_{49}$	19.6	1.44
GCP5	73.4	27.1	$P(THP–HEMA)_{69}$-$PTESPMA_{41}$	20.8	1.41
GCP6	77.8	29.1	$P(THP–HEMA)_{68}$-$PTESPMA_{49}$	22.0	1.51

[a]Conditions: $[MacroCTA]_0/[AIBN]_0/[THP–HEMA]_0/[TESPMA]_0$ = 1/0.25/75/0 to 75 (GCP1–2), $[MacroCTA]_0/[AIBN]_0/[THP–HEMA]_0/[TESPMA]_0$ = 1/0.25 to 0.5/75/0 to 75 (GCP3–6). [b]Obtained from GPC relative to linear polymethyl methacrylate standards in THF at 25 °C.

Interestingly, the gradient copolymers synthesized with a TESPMA feeding rate of 1.0 mL h^{-1} (GCP1, GCP3 ane GCP5) show consistently lower conversions and molecular weights as compared to the copolymers synthesized with a TESPMA feeding rate of 1.5 mL h^{-1} (GCP2, GCP4 and GCP6). These findings are presumably attributed to a slower polymerization rate at higher conversions due to the occurrence of side reactions such as radical coupling. Thus, giving gradient copolymers with overall lower conversions and lower molecular weights. To further evaluate the copolymerization kinetics, the corresponding GPC traces were analyzed in respect to their MWD with time, as depicted

in Figure 38. The GPC traces are shifted to higher molar masses, indicating an efficient re-initiation/propagation of the growing macroradical with time.

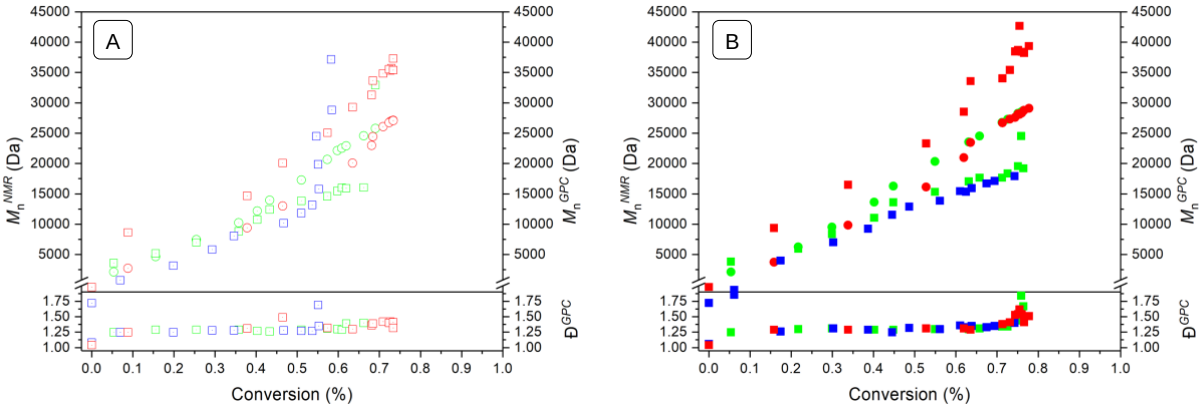

Figure 37. A) Number average molecular number estimated by $_1$H NMR analysis (M_{nNMR}, open circles) and by GPC (M_{nGPC}, open squares) and dispersity (Đ) versus conversion for the CDTSPA mediated THP–HEMA/TESPMA copolymerization with a TESPMA feeding rate of 1.0 mL h^{-1}. B) M_{nNMR} (closed circles) and M_{nGPC} (closed squares) and *Đ* versus conversion for the CDTSPA mediated THP–HEMA/TESPMA copolymerization with a TESPMA feeding rate of 1.5 mL h^{-1}. Conditions: [CDTSPA]$_0$/[AIBN]$_0$ = 1/0.25, 1,4-dioxane, 70 °C (blue); [CDTSPA]$_0$/[AIBN]$_0$ = 1/0.25 to 0.5, 1,4-dioxane, 70 °C (green); [CDTSPA]$_0$/[AIBN]$_0$ = 1/0.25 to 0.5, 1,4-dioxane, 80 °C (red).

The appearing shoulders at higher molar masses clearly show a loss of control over time due to a higher number of termination events at higher monomer conversions. These observations are consistent with the findings of the $_1$H NMR kinetic analysis and thus, demonstrate a loss of control over the reaction kinetics with increasing monomer conversion. To investigate the evolution of the comonomer fraction with changing THP–HEMA/TESPMA feed ratio, the cumulative comonomer fractions (F_{cum}) were calculated according to Equation 19 and Equation 20 and plotted against the normalized chain length (total monomer conversion), as illustrated in Figure 31.

$$F_{cum}^{THP-HEMA} = \frac{conv_{THP-HEMA}^{NMR} \cdot [M_{THP-HEMA}]_0}{conv_{THP-HEMA}^{NMR} \cdot [M_{THP-HEMA}]_0 + conv_{TESPMA}^{NMR} \cdot [M_{TESPMA}]_0} \quad (19)$$

$$F_{cum}^{TESPMA} = \frac{conv_{TESPMA}^{NMR} \cdot [M_{TESPMA}]_0}{conv_{THP-HEMA}^{NMR} \cdot [M_{THP-HEMA}]_0 + conv_{TESPMA}^{NMR} \cdot [M_{TESPMA}]_0} \quad (20)$$

where $conv_{NMR}$ are the corresponding conversions and $[M_{THP–HEMA/TESPMA}]_0$ are the initial monomer concentrations of THP–HEMA and TESPMA.

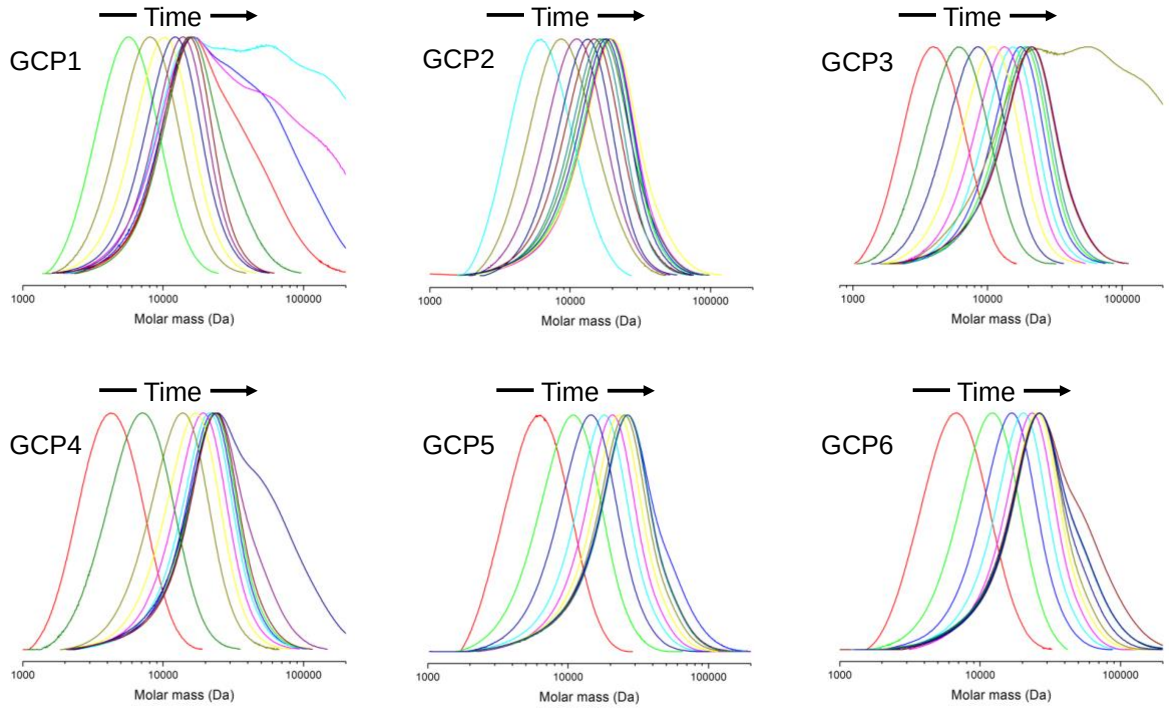

Figure 38. GPC traces of P(THP–HEMA)-*grad*-PTESPMA copolymers (GCP1–6).

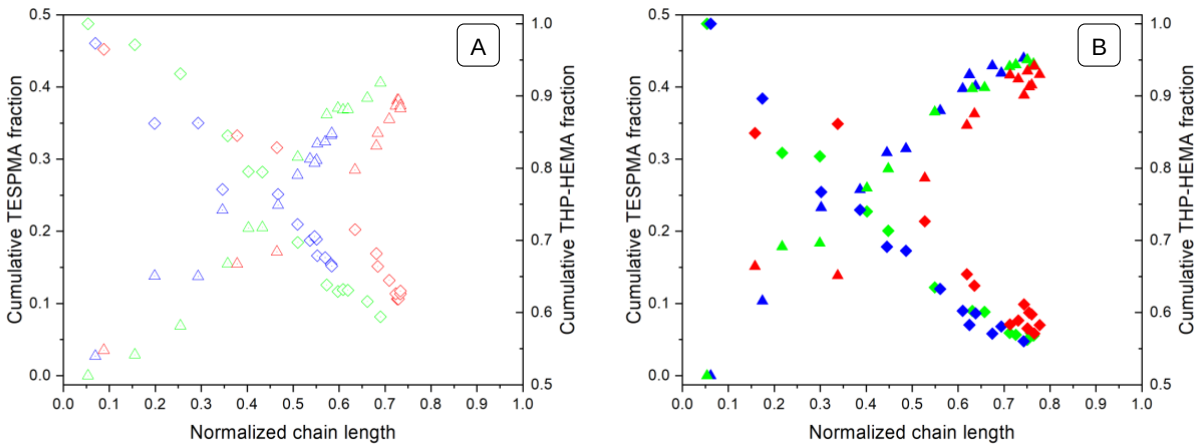

Figure 39. A) Cumulative TESPMA and THP–HEMA fraction versus normalized chain length with a TESPMA feeding rate of 1.0 mL h^{-1}. B) Cumulative TESPMA and THP–HEMA fraction versus normalized chain length with a TESPMA feeding rate of 1.5 mL h^{-1}. The triangles denote TESPMA and rhombi denote THP–HEMA. Conditions: $[CDTSPA]_0/[AIBN]_0$ = 1/0.25, 1,4-dioxane, 70 °C (blue); $[CDTSPA]_0/[AIBN]_0$ = 1/0.25 to 0.5, 1,4-dioxane, 70 °C (green); $[CDTSPA]_0/[AIBN]_0$ = 1/0.25 to 0.5, 1,4-dioxane, 80 °C (red).

These plots clearly demonstrate that an appreciable compositional gradient can be formed by using a semi-batch forced gradient approach. In addition, the composition of the gradient can be altered by changing the feeding rates of TESPMA, giving compositional gradients with steeper composition profiles (Figure 39B) or smoother composition profiles (Figure 39A). After the careful investigation and evaluation of the copolymerization kinetics, the most appropriate conditions to synthesize gradient copolymers with precise microstructures and reasonable narrow MWD was found to be the CDTSPA mediated copolymerization at 80 °C in 1,4-dioxane (GCP5 and GCP6). In order to minimize the appearance of chain defects, the semi-batch forced gradient synthesis was terminated after 9 h giving the gradient copolymers GCP7 (M_{nNMR} = 26.9 kDa, P(THP–HEMA)$_{67}$-PTESPMA$_{42}$, M_{nGPC} = 19.8 kDa, $Đ$ = 1.40) and GCP8 (M_{nNMR} = 28.8 kDa, P(THP–HEMA)$_{66}$-PTESPMA$_{49}$, M_{nGPC} = 21.3 kDa, $Đ$ = 1.41). To prevent the formation of silica aggregates due to the reactive Si-OCH$_2$CH$_3$ motifs, the gradient copolymers were stored in anhydrous THF at a concentration of 100 mg mL^{-1}. These gradient copolymers were further characterized via TGA to evaluate their thermal stability.

4.2.3.1 Thermal properties of P(THP–HEMA)-*grad*-PTESPMA

Thermal stabilities and decomposition patterns of the gradient copolymers GCP7 and GCP8 were evaluated by using TGA, as displayed in Figure 40. According to TGA, both gradient copolymers reveal a two-step degradation pattern, in which the first degradation step is attributed to the loss of the pendant THP groups of the polymer side chains.

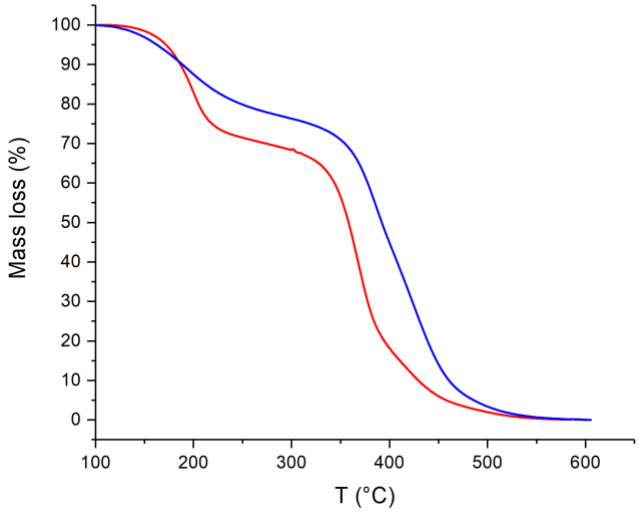

Figure 40. Thermogravimetric analysis of GCP7 (red curve) and GCP8 (blue curve).

The second degradation step of GCP8 is shifted to higher temperatures as compared to GCP7, which is presumably attributed to the higher incorporated TESPMA fraction F_{TESPMA} = 0.43 in GCP8 compared to F_{TESPMA} = 0.39 in GCP7. These observations are consistent with the thermal analysis of BCP 1–3, in which the second degradation step was shifted to higher temperatures upon increasing the TESPMA block length (see 4.1.3.1).

In summary, the semi-batch forced gradient approach enabled the preparation of THP-HEMA and TESPMA based copolymers with gradient microstructures. Due to the inherent reactivity of the comonomer pair, the composition profiles of the gradient copolymers could be altered by appropriate adjustment of the TESPMA feeding rate. Wherein, a faster TESPMA feeding rate of 1.5 mL h^{-1} yielded a gradient copolymer with a steeper gradient composition profile as compared and *vice versa*. After careful evaluation and adjustment of the reaction parameters such as temperature, initiator concentration and reaction time, undesired side reactions could be reduced to a minimum. These optimizations give rise to gradient copolymers with precise microstructures and reasonably narrow MWDs.

4.3 Hybrid inorganic/organic copolymer thin films

This chapter deals with the fabrication of sol-gel derived hybrid inorganic/organic coatings on glass slides by using a grafting-*onto* spin coating approach. For this purpose, hybrid inorganic/organic gradient copolymers with different composition profiles as well as hybrid inorganic/organic diblock copolymers with three different TESPMA block lengths were employed as precursor to fabricate such hybrid coatings. These hybrid coatings were further characterized in respect to their film thickness, film roughness and wettability by using AFM and contact angle measurements. To gain more information about the structural composition of these hybrid films, the hybrid films were characterized via XPS and IRRAS.

4.3.1 Fabrication of hybrid inorganic/organic thin films

For the preparation of sol-gel derived hybrid coatings, purified gradient copolymers GCP7 (M_{nNMR} = 26.9 kDa, P(THP–HEMA)$_{67}$-PTESPMA$_{42}$, M_{nGPC} = 19.8 kDa, $Đ$ = 1.40) and GCP8 (M_{nNMR} = 28.8 kDa, P(THP–HEMA)$_{66}$-PTESPMA$_{49}$, M_{nGPC} = 21.3 kDa, $Đ$ = 1.41) solutions in anhydrous THF (c ≈ 100 mg mL^{-1}) were diluted in a THF/water mixture to afford a precursor concentration of 50 mg mL^{-1} with 10 Vol.-% of water. Above 10 Vol.-% of water content, the copolymer started to precipitate out of the precursor solution. The pristine

glass slides were immobilized with piranha acid before use and washed with THF to remove residual dust from the glass surface. On the center of the glass slides was placed a droplet of the precursor solution (150 µL) and the glass substrate was rotated for 60 sec. at 3000 rpm with a spinning ramp of 1000 rpm sec.$^{-2}$ in order to homogeneously distribute the precursor solution over the glass surface area. To evaluate the impact of the catalyst on the surface topographies of the corresponding hybrid films, the gelation of the pendant Si-OCH_2CH_3 motifs was triggered with 1M HCl and 1M NaOH solution, as demonstrated in Scheme 16.

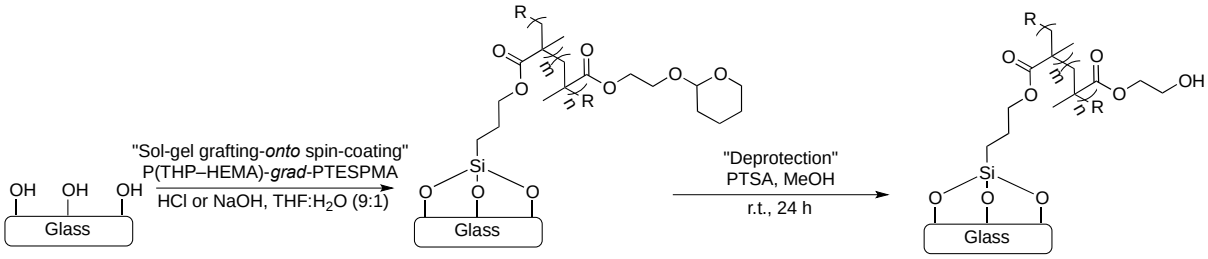

Scheme 16. Fabrication of hybrid inorganic/organic thin films by using a sol-gel grafting-*onto* approach.

The hybrid films derived from NaOH mediated sol-gel grafting-*onto* approach were further treated with methanolic 0.1M PTSA solution in order to cleave the pendant THP-groups on the surface. Contrary to this, it was assumed that the HCl mediated reaction triggers the cleavage of the pendant THP groups as well as the formation of Si-O-Si bonds. To prove this hypothesis, the hybrid films were investigated by using water contact angle measurements, as detailed in Table 12. According to these measurements, the NaOH hybrid films show a slightly smaller contact of (67.21 ± 2.02) (GCP7) and (69.38 ± 1.14) (GCP8) compared to the HCl derived hybrid films of (74.86 ± 1.15) (GCP7) and (76.03 ± 1.23) (GCP8). These findings clearly suggest that the HCl mediated reaction does not cleave the pendant THP groups. The slightly higher hydrophilicity of the NaOH derived hybrid films compared to the HCl derived hybrid films might attributed to the appearance of non-reacted Si-OH motifs within the silica network. The decreased water contact angles of (57.14 ± 2.34) (GCP7) and (61.48 ± 2.40) (GCP8) after treatment with 0.1M PTSA indicate the successful cleavage of the pendant THP groups. These findings are consistent with the batch deprotection of P(THP–HEMA), in which the pendant THP groups were quantitatively cleaved by using PTSA as deprotection agent (see 4.1.2.1).

Table 12. Water contact angles of hybrid films by using GCP7 and GCP8 as precursor.

Entry	Catalyst	Contact angle[a] (deg.)	Contact angle[b] (deg.)
pristine glass	–	48.79 ± 0.67	–
GCP7	HCl	74.86 ± 1.15	–
GCP7	NaOH	67.21 ± 2.02	57.14 ± 2.34
GCP8	HCl	76.03 ± 1.23	–
GCP8	NaOH	69.38 ± 1.14	61.48 ± 2.40

[a]Water contact angles of hybrid films fabricated via sol-gel grafting-*onto* spin-coating under atmospheric conditions. [b]Water contact angle after treatment with 0.1M PTSA solution.

To further characterize the hybrid films in respect to their surface topography, AFM images were recorded by facilitating the force modulation method, as illustrated in Figure 41. According to the AFM images, the hybrid films reveal microporous structures due to the formation of a polymeric silica network.

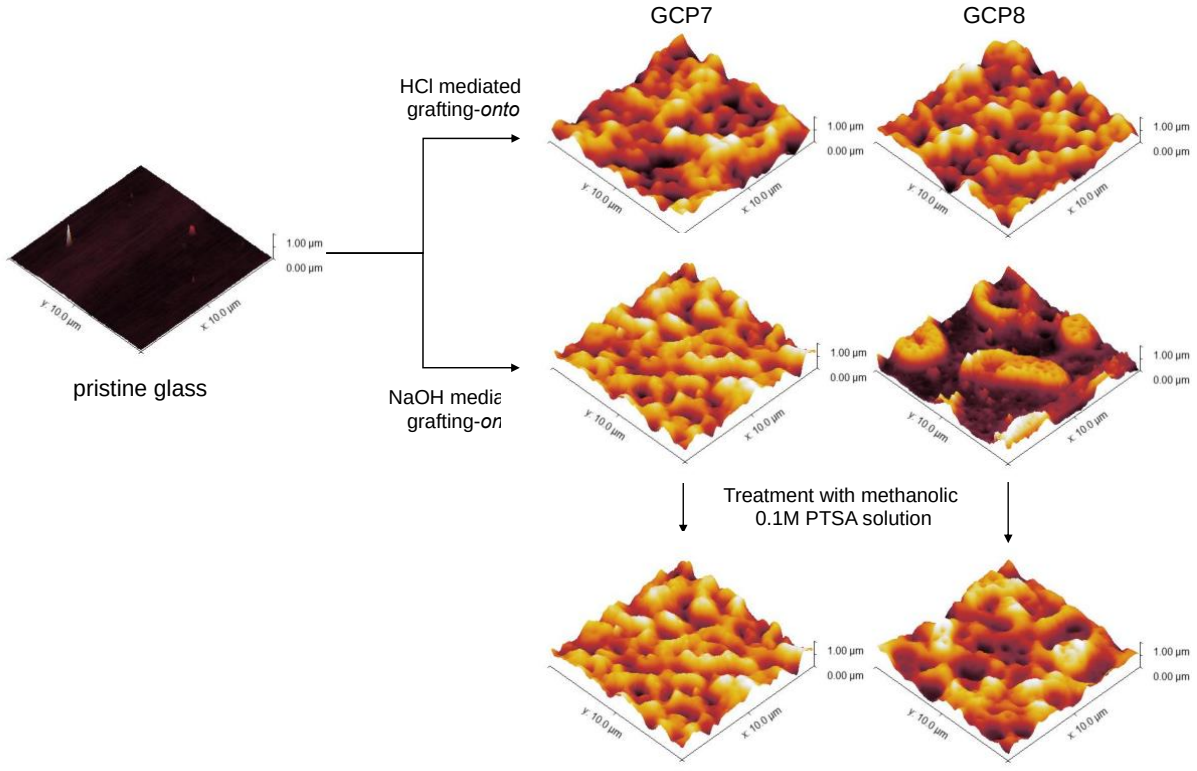

Figure 41. AFM images of HCl and NaOH derived hybrid films by using GCP7 and GCP8 as precursor.

To evaluate the film thickness of the corresponding hybrid films, the film surface was scratched and analyzed with AFM, as summarized in Table 13. The local surface

roughness's were calculated by using root-mean-square (RMS) data analysis from a 10 µm x 10 µm surface area. According to AFM analysis, the HCl derived hybrid films exhibit a slightly thinner film thickness of 240 nm (GCP7) and 250 nm (GCP8) compared to 300 nm (GCP7) and 390 nm (GCP8) respectively. These slight variations in the hybrid film thickness might be attributed to different crosslinking efficiencies and to a lower crosslinking density of the NaOH derived hybrid films. Notably, the NaOH derived hybrid films reveal a decreased film thickness of 180 nm (GCP7) and 200 nm (GCP8) upon treatment with PTSA and thus, indicating the formation of a denser polymeric silica network due to post-crosslinking of non-reacted Si-OH motifs. Similarly, the surface roughness of the NaOH derived hybrid films decreased from 106 nm to 78 nm (GCP7) and from 232 nm to 135 nm (GCP8) upon treatment with PTSA. Interestingly, the GCP8 precursor yields thicker hybrid films compared to the GCP7 hybrid films, which is presumably attributed to the slightly higher mole fraction of incorporated TESPMA in the GCP8 precursor (F_{TESPMA} = 0.43) compared to the GCP7 precursor (F_{TESPMA} = 0.39). To evaluate the impact of the surface roughness on the surface wettability, the contact angles were related to the surface roughness's of the GCP7 and GCP8 derived films. In case of the NaOH derived films, the decrease of surface roughness's is directly related to the decrease of the water contact angles.

Table 13. AFM analysis of HCl and NaOH derived hybrid films.

Entry[a]	Catalyst	Film thickness (nm)	RMS roughness (nm)
pristine glass	–	–	1
GCP7	HCl	240	122
GCP7	NaOH	300	106
		180[b]	78[b]
GCP8	HCl	250	87
GCP8	NaOH	390	232
		200[b]	135[b]

[a]Film thickness and roughness of hybrid films fabricated via sol-gel grafting-*onto* spin-coating under atmospheric conditions. [b]Film thickness and roughness after treatment with 0.1M PTSA solution. The film thickness and RMS roughness were determined by using software analysis (Gwydion 2.4.1).

These observations suggest that the surface of the NaOH derived films is wetted homogeneously and the water droplet is in a Wenzel-like state. Thus, the NaOH derived hybrid films become less hydrophobic upon treatment with methanolic PTSA solution, due to smoothening of the surface. Contrary to these observations, the surface roughness's of the HCl derived hybrid films have only a minor impact on the water contact angle. This observation might be attributed to a more heterogenous wetting of the surface as compared to the NaOH derived hybrid films. To further prove this hypothesis, BCP4 (M_{nNMR} = 47.2 kDa, P(THP–HEMA)$_{93}$-PTESPMA$_{93}$, M_{nGPC} = 46.8 kDa, $Đ$ = 1.25), BCP5 (M_{nNMR} = 34.3 kDa, P(THP–HEMA)$_{93}$-PTESPMA$_{45}$, M_{nGPC} = 30.7 kDa, $Đ$ = 1.23) and BCP6 (M_{nNMR} = 26.8 kDa, P(THP–HEMA)$_{93}$-PTESPMA$_{22}$, M_{nGPC} = 27.3 kDa, $Đ$ = 1.34) diblock copolymers with various TESPMA block lengths were employed as precursor to afford hybrid films with various film thickness's. The BCP4–6 precursors were grafted on glass slides by using the same NaOH mediated sol-gel grafting-*onto* spin-coating approach as mentioned before, as displayed in Figure 42.

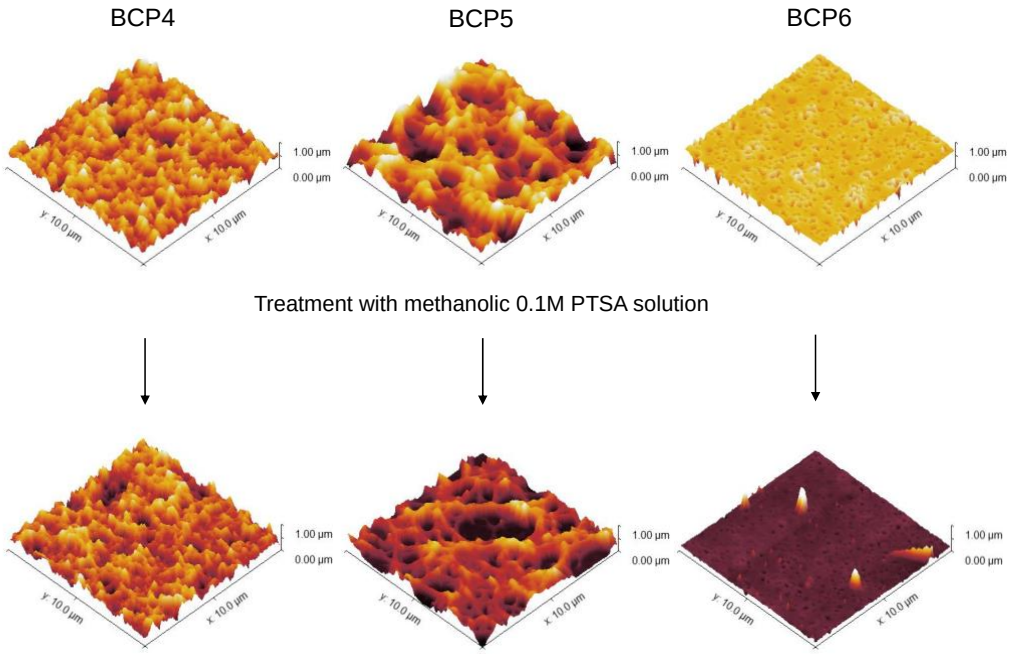

Figure 42. AFM images of NaOH derived hybrid films by using BCP1, BCP2 and BCP3 as precursor.

According to the water contact angle measurements, the hydrophobicity of the hybrid films increases with increasing TESPMA block length as indicated by the increased water contact angle from (58.39 ± 1.21) (BCP3) to (85.70 ± 1.75) (BCP1), as summarized in Table 14. These findings suggest the formation of a denser polymeric silica network by employing a BCP with a longer TESPMA block segment. After treatment with methanolic

0.1M PTSA solution, the contact angles of the BCP derived hybrid films decreased to (60.03 ± 1.85) (BCP4), (56.71 ± 6.94) (BCP5) and (51.56 ± 0.72). The higher relative decrease of the BCP4 and BCP5 derived hybrid films (~30%) are presumably attributed to a higher polymer grafting density as compared to the BCP3 derived hybrid films. The surface topographies of BCP 4 and BCP 5 exhibit a similar porous microstructure as the hybrid films derived from GCP7 and GCP8.

Table 14. Water contact angles of hybrid films by using BCP1, BCP2 and BCP3 as precursor.

Entry	Catalyst	Contact angle[a] (deg.)	Contact angle[b] (deg.)
pristine glass	–	48.79 ± 0.67	–
BCP4	NaOH	85.70 ± 1.75	60.03 ± 1.85
BCP5	NaOH	77.20 ± 1.36	56.71 ± 6.94
BCP6	NaOH	58.39 ± 1.21	51.56 ± 0.72

[a]Water contact angles of hybrid films fabricated via sol-gel grafting-*onto* spin-coating under atmospheric conditions. [b]Water contact angle after treatment with 0.1M PTSA solution.

Table 15. AFM analysis of NaOH derived hybrid films.

Entry[a]	Catalyst	Film thickness[b] (nm)	RMS roughness[b] (nm)
pristine glass	–	–	1
BCP4	NaOH	400	239
		300[b]	175[b]
BCP5	NaOH	300	206
		190[b]	155[b]
BCP6	NaOH	130	48
		100[b]	67[b]

[a]Film thickness and roughness of hybrid films fabricated via sol-gel grafting-*onto* spin-coating under atmospheric conditions. [b]Film thickness and roughness after treatment with 0.1M PTSA solution. The film thickness and RMS roughness were determined by using software analysis (Gwydion 2.4.1).

In general, the BCP4 derived hybrid film reveal microstructures with smaller pore size as compared to the BCP5 and BCP6 derived hybrid films, which indicates the formation of a denser polymeric silica network. The film thicknesses and RMS roughness's of the corresponding BCP derived hybrid films are summarized Table 15. In general, the film thickness of the BCP derived hybrid films increases from 130 nm (BCP6) to 400 nm (BCP4) with increasing TESPMA block length as well as decrease upon treatment with methanolic PTSA solution. To further evaluate the surface characteristics of the BCP derived hybrid films, the surface roughness's of the individual films were correlated to the water contact angles before and after treatment with methanolic PTSA solution. The decrease of surface roughness's is directly related to the decrease of the water contact angles and thus, the hydrophobicity of the films is affected by the surface roughness. These observations are consistent with the observations made by the GCP derived hybrid films.

In summary, a higher incorporated TESPMA fraction yield thicker hybrid films with porous microstructures. These microstructures clearly indicate the formation of a silica-based inorganic/organic phase on glass substrate surface. In addition, the surface roughness's of the GCP and BCP derived hybrid films is directly related to the water contact angles. Thus, the hydrophobicity of these films decreases upon treatment with methanolic PTSDA solution, due to smoothing of the film surface.

4.3.2 Structural analysis of hybrid inorganic/organic thin films

To unveil the structural identity of the hybrid films, there were further characterized via IRRAS and XPS. Since IRRAS requires a substrate surface with a high IR reflectivity in order to maximize the reflection of the incident IR beam, the glass slides were sputtered with gold (layer thickness ~ 40 nm) and plasma treated, as shown in Figure 43. The plasma etching was carried out in order to regain a sol-gel active OH functionalities on the surface.

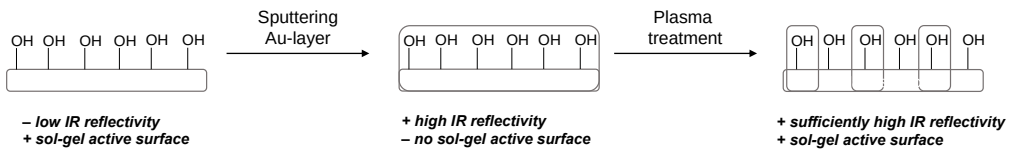

Figure 43. Schematic illustration of the used method to enhance the IR reflectivity of glass substrates.

The hybrid film formation was accomplished as mentioned before by using NaOH as catalyst. The IRRAS spectra of the hybrid films before and after treatment with methanolic 0.1M PTSA solution were recorded at an angle of incidence of 84°, as depicted in Figure 44. Both spectra were normalized in respect to the stretching vibrations of carbonyl (C=O) groups at 1735 cm^{-1}. The IRRAS spectra correspond to the average spectra of three records. The hybrid films exhibited some characteristic vibrations of both PTESPMA, P(THP–HEMA) and PHEMA such as Si-O-Si, Si-O, C=O and C-O, as detailed in Table 16.

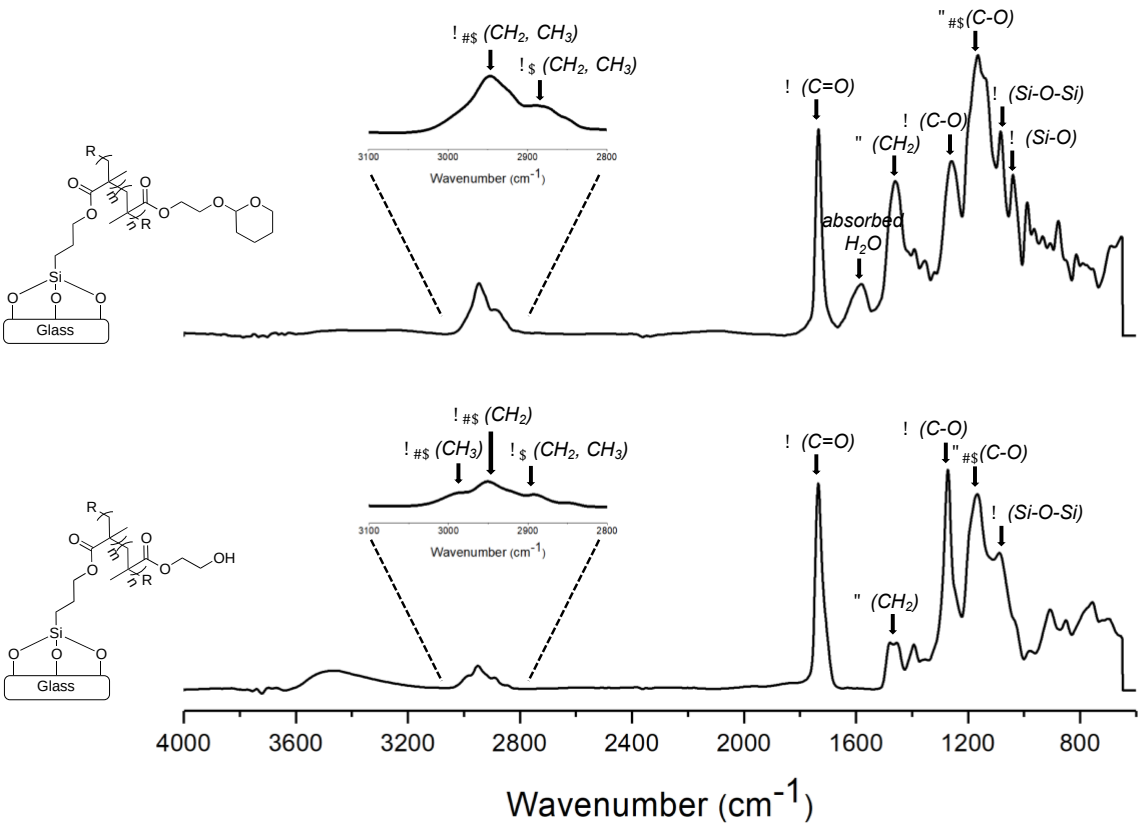

Figure 44. IRRAS spectra of a NaOH derived hybrid film by using GCP8 as precursor (top) and IRRAS spectra of a NaOH derived hybrid film after treatment with methanolic PTSA solution (bottom). The inset shows the symmetric and asymmetric stretching vibrations of the CH_3 and CH_2 groups between 2800 and 3100 cm^{-1}.

The peak position related to the asymmetric and symmetric stretching vibrations of CH_3 and CH_2 are shifted to higher frequencies upon treatment of the hybrid film with PTSA. Meanwhile, the stretching vibrations of C=O and the deformation vibrations of CH_2 exhibit no evident frequency shift. The stretching vibration and asymmetric deformation vibrations of C-O at 1260 cm^{-1} and 1166 cm^{-1} respectively are shifted to higher frequencies of 1271 cm^{-1} and 1168 cm^{-1} respectively. Since these bands are attributed to the appearance of ester bonds and THP groups, these observations suggest a successful deprotection of the

THP groups upon treatment with methanolic PTSA solution. Furthermore, the intensity of the stretching vibration band of C-O is largely increased, whereas the intensity of the deformation vibration band of C-O is decreased, due to loss of the cyclic acetal of the THP groups. Notably, the three stretching vibration bands of the Si-O-Si and Si-O species at 1082, 1039 and 989 cm_{-1} are smoothed to one vibration band at 1079 cm_{-1}. These observations suggest a post-crosslinking on non-reacted Si-OR and Si-OH species upon acidic treatment and are consistent with the results obtained via AFM analysis.

Table 16. Spectral band assignments for immobilized hybrid films before and after treatment with methanolic 0.1M PTSA solution.

Frequency[a] (cm_{-1})	Possible assignment[a]
2946 2952[b]	ν_{as} (CH_2, CH_3)
2856 2863[b]	ν_s (CH_2, CH_3)
1735 1736[b]	ν (C=O)
1457 1454[b]	δ (CH_2)
1260 1271[b]	ν (C–O)
1166 1168[b]	δ_{as} (C–O)
1082, 1039, 989 1079[b]	ν (Si–O–Si, Si–O)

[a]Spectral band assigments of NaOH derived hybrid films by using GCP8 as precursor. [b]Spectral band assignments of NaOH derived hybrid film after treatment with methanolic 0.1M PTSA solution.

Quantitative elemental analysis on the modified glass surfaces was obtained by using XPS to characterize the covalently immobilized GCP8 before and after treatment with PTSA, as detailed in Table 17. Based on the observations made by XPS, the relative atomic percent concentration of carbon (C) decreased from 70.5% to 65.5%, whereas the atomic percent concentrations of oxygen (O) and of silicon (Si) increased from 21.7% to 24.4%

and from 7.2% to 10.1% respectively. These findings are consistent with the theoretical elemental composition of hybrid film before and after treatment with PTSA. The small deviations between the experimental and theoretical atomic percent concentrations are attributed to minor impurities at the surface such as carbon contamination of the gold surface due to environmental exposure as well as adsorption of water and other contaminants. Since both hybrid films contain carbon and oxygen, it is nearly impossible to distinguish the source of carbon and oxygen in XPS wide scan. Consequently, to further characterize the hybrid films C1s core level analysis was performed to quantify the O-C-O and C-O-C functionalities unique to the THP ether acetal moiety, as demonstrated in Figure 44. Since, the O-C-O and C-O-C functionalities are exclusively present in the non-treated hybrid film and thus, the disappearance of corresponding peaks in the C1s peak would clearly indicate the cleavage of the pendant THP groups.

Table 17. Estimated elemental compositions and theoretical elemental composition of hybrid films before and after treatment with PTSA.

Entry	C (%)	O (%)	Si (%)	Na (%)
1*a*	70.5	21.7	7.2	0.6
	(72.0)	(24.0)	(4.0)	–
2*b*	65.5	24.4	10.1	–
	(68.4)	(26.3)	(5.3)	–

*a*Elemental composition of NaOH derived hybrid films by using GCP8 as precursor. *b*Elemental composition of NaOH derived hybrid film after treatment with methanolic 0.1M PTSA solution.

The position of the C-C/C-H in C1s spectra was specified and the peaks of the different carbon environments were referenced relative to the C-C/C-H peak at (284.6 ± 0.1) eV. The C1s spectra for the non-treated hybrid film was fitted with five peaks: (C-H/C-C) at (284.6 ± 0.1) eV, (C-O-C) at (286.4 ± 0.1) eV, (C-O-C=O) at (286.8 ± 0.1) eV, (O-C-O) at (287.6 ± 0.1) and (C-O-C=O) (288.7 ± 0.1) eV, as demonstrated in Figure 45A, whereas the C1s spectra of the hybrid film treated with methanolic 0.1M PTSA solution was fitted with four peaks: (C-H/C-C) at (284.6 ± 0.1) eV, (C-OH) (286.6 ± 0.1), (C-O-C=O) at (286.8 ± 0.1) eV and (C-O-C=O) (288.7 ± 0.1) eV, as displayed in Figure 45B. The quantitative analysis of the percentage of XPS C1s signals are summarized in Table 18. According to the XPS high-resolution C1s spectra, the signals of the C-O-C and C-O-C functionalities

disappeared after treatment of the GCP8 derived hybrid film with methanolic 0.1M PTSA solution. Consistently to this, (C-OH) signal shows the appearance of OH functionalities on the hybrid film surface.

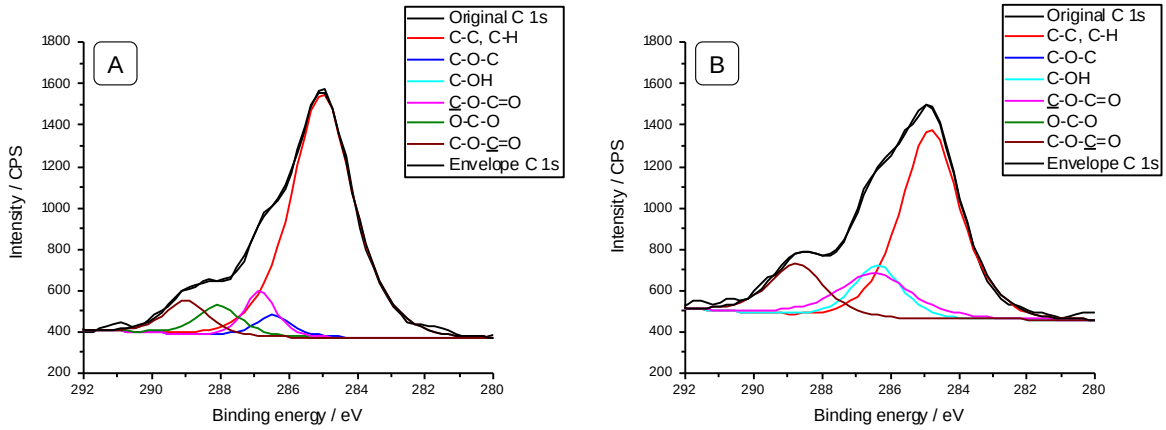

Figure 45. A) XPS high-resolution C1s spectra of NaOH derived hybrid film by using GCP8 as precursor. B) XPS high-resolution C1s spectra of NaOH derived hybrid film after treatment with methanolic 0.1M PTSA solution.

Table 18. Estimated functionality percentage concentration of hybrid films before and after treatment with PTSA.

Entry	C-C/C-H (%)	C-O-C (%)	C-OH (%)	C-O-C=O (%)	O-C-O (%)	C-O-C=O (%)
1*a*	71.6	6.1	–	8.2	6.4	7.2
2*b*	59.8	–	13.0	12.8	–	14.4

*a*Elemental composition of NaOH derived hybrid films by using GCP8 as precursor. *b*Elemental composition of NaOH derived hybrid film after treatment with methanolic 0.1M PTSA solution.

These findings clearly suggest the successful cleavage of the pendant THP groups upon acidic treatment. However, the experimentally proportion of the alcohol carbon (C-OH) in the C1s spectra is slightly higher as compared to the theoretical value, indicating the adsorption of water or residual solvent upon treatment with methanolic 0.1M PTSA solution. According to the findings in the IRRAS and XPS experiments, the treatment with methanolic PTSA solution results in the quantitative cleavage of THP groups located on the surface of the hybrid films. In the next step, these hybrid films with nucleophilic OH

groups will be utilized in micromechanical tests in order to evaluate the impact of the polymeric interphase on the mechanical properties of a given glass/polyepoxide system.

4.4 Micromechanical analysis

Mode 1 tensile tests enabled the determination of the interfacial tensile strength (τ_{max}) and evaluation the impact of the polymeric interphase on the micromechanical properties of glass slide-model system. To prepare the test samples, two coated glass slides were fixed with a stainless-steel clamp between a 2 mm thick PTFE-foil as spacer giving a cavity of 180 mm^2 (V_{Epoxy}) with a surface area of 90 mm^2 (A_{Epoxy}), see experimental part Figure 47A. Next, the sample was immersed in the resin system at room temperature to allow the epoxy resin to suck into the cavity. The epoxy resin was cured at 100 °C for 2 h according to an adapted procedure of Sturm and co-workers. [147, 148] Upon curing of the resin system, a strong network was formed composed of diglycidyl ethers of bisphenol A. Thus, the uncured epoxy resin network allows the incorporation of PHEMA chains into the network due to chemical and physical attachment of the PHEMA chains to the resin network. The mechanism of surface-grafted polymeric connector chains in interface/interphase systems has been intensively investigated by Gutowski and co-workers. [149, 150] The interpenetrating surface-tethered PHEMA chains can become trapped in the matrix network and thus, acting as mechanical interlocking agents within the network. The test samples were carefully mounted on two metal attachments by using an epoxide-based glue and fixed into the Zwick 1454 tensile testing machine, see experimental part Figure 48B and 48C. In a first step, three Force-Distant-Curves for each sample were recorded in order to determine the maximal force (F_{max}) to break the test sample, as demonstrated in Figure 46A and 46B. Upon simplifying the assumption, that the debonding force is distributed equally on the glass slide-matrix interface, the interfacial tensile strength can be calculated by using equation 21.

$$\tau_{max} = \frac{F_{max}}{A_{Epoxy}} \tag{21}$$

The micromechanical results are summarized in Table 19. To relate and evaluate the macromolecular interphase nanostructure to the micromechanical properties, the nominal τ_{max} values were practically compared with the reference test sample, which was composed of two pristine glass slides, as displayed in Figure 46A. The surface coverage (Γ) of the corresponding hybrid films were estimated by using equation 22. [151, 152]

$$\Gamma = h \cdot \rho \tag{22}$$

where *h* is the layer thickness and ρ is the bulk density of the thin polymer film. Herein, the bulk density was set to 50 mg cm^{-3}, which corresponds to the density of the pure precursor solution. The grafting densities (σ) of the corresponding hybrid films are the inverse of the average area per adsorbed polymer chain, as approximated in equation 23.

$$\sigma = \frac{\Gamma \cdot N_A}{M_n^{NMR}} \tag{23}$$

where N_A is the Avogadro constant and M_{nNMR} is the molar mass of the attached polymer chains.

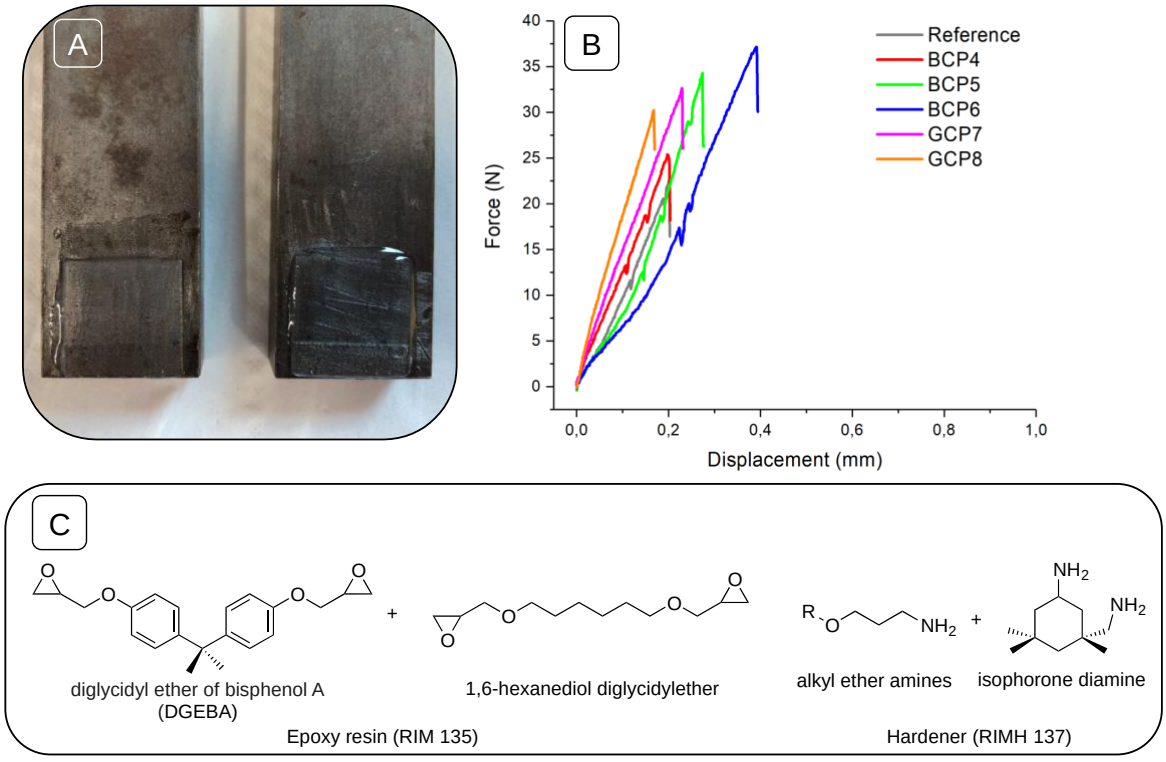

Figure 46. A) Image of a sample after testing it on the Zwick 1454 tensile testing machine B) Force-displacement-curves of the corresponding test samples. The Force-Distance-Curves correspond to the average of three measurements. C) Chemical structures of the epoxy matrix composed of EPIKOTE Resin MGS RIM 135/EPIKURE CuringAgent MGS RIMH 137.

According to the micromechanical analysis, the interfacial tensile strength is relatively increased between 11.9% and 51.1% as compared to the reference test sample. These findings clearly suggest that the introduction of polymeric interphase enhances interfacial adhesion between the glass slide and matrix. Notably, the block copolymer with a short TESPMA block segment (BCP6) shows a remarkably higher interfacial tensile strength of (413.3 ± 9.1) Pa as compared to the tensile strength of (282.2 ± 69.6) Pa of the block copolymers with a long TESPMA block segment (BCP4).

Table 19. Results from the micromechanical analysis.

Entry[a]	F_{max}[a] (N)	τ_{max} (Pa)	Film thickness[b] (nm)	Γ_c (mg cm^{-2})	σ_c (chains nm^{-2})
Reference	22.7 ± 5.8	252.2 ± 64.2	–	–	–
BCP4	25.4 ± 6.3	282.2 ± 69.6	300	1.5 x 10^{-3}	0.19
BCP5	34.3 ± 8.3	381.1 ± 92.2	190	9.5 x 10^{-4}	0.16
BCP6	37.2 ± 1.3	413.3 ± 9.2	100	5.0 x 10^{-4}	0.11
GCP7	32.6 ± 3.8	362.2 ± 13.6	180	9.0 x 10^{-4}	0.20
GCP8	30.0 ± 6.9	333.6 ± 77.5	200	1.0 x 10^{-3}	0.21

[a]The F_{max} values correspond to the average of three measurements. [b]Film thicknesses were estimated via AFM analysis and subsequent software supported data analysis (Gwydion 2.4.1). [c]The surface coverages and grafting densities were calculated according to equation 18 and 19.

Similarly, GCP7 with an incorporated TESPMA fraction of 0.39 reveals a slightly higher interfacial tensile of (362.2 ± 13.6) Pa compared to (333.6 ± 77.5) Pa of GCP8 with an incorporated TESPMA fraction of 0.43. In general, it seems that a shorter TESPMA anchor segment results in a higher interfacial adhesion. To further prove this hypothesis, the individual hybrid film thicknesses were related to the interfacial tensile strength, as demonstrated in Figure 46B. According to this, the interfacial tensile strength decreases with increasing film thickness of the hybrid coatings. These findings might be attributed to an insufficient penetration of the PHEMA chains into the epoxy matrix due to a high chain density of PHEMA chains on the surface. Consequently, to reach a sufficient penetration of the PHEMA chains, it is desirable to fabricate thin hybrid films with thicknesses of ≤100 nm and rather low grafting densities in order to maximize the interpenetration of PHEMA chains. These observations are consistent with previously reported investigations, in which the interfacial adhesion was directly related to the film thickness and grafting density of the

tethered polymer chains. In these studies, the interfacial adhesion was maximized by using thin polymer films with rather low grafting densities in order to afford a high interfacial adhesion between a glass/epoxy matrix interface. [12] In addition, Duchet *et. al.* stated that the toughness of composite-like material can be improved by the presence of tethered polymer chains at the reinforcement/matrix interface, whereas a too high grafting density compromise the interfacial adhesion. [6] Notably, the results suggest that the composition of the precursor polymer and the morphology of the hybrid films have only a minor impact on the interfacial adhesion. Most likely, the structural differences between the individual hybrid films are neglectable on a nanometer-scale and thus, the interfacial adhesion is mainly affected by the grafting densities of the corresponding hybrid films.

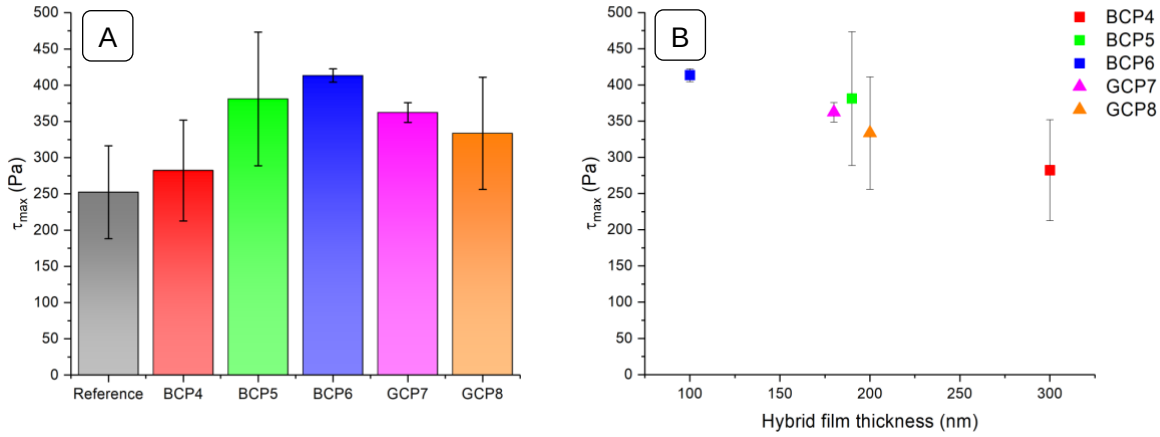

Figure 47. Mechanical performance of the BCP4–6, GCP7 and GCP8 coated glass slides: A) Nominal interfacial shear strength. B) Correlation of the nominal interfacial shear strength to the hybrid film thicknesses.

However, these observations might change by approaching hybrid films with thicker film thicknesses of ≥ 1000 nm, in which the structural composition and inherent mechanical properties of the hybrid films become more dominant.

Based on the findings made by the micromechanical analysis, the introduction of a silane-based polymeric interphase provides a sufficient stress transfer from the polymer matrix to glass and thus, give rise to a glass/polyepoxide material with improved mechanical properties. The interfacial tensile strength between glass and the polymer matrix increases regardless of the employed polymeric precursor. The maximum tensile strength of (413.3 ± 9.2) Pa is reached by using a linear diblock copolymers (BCP6) as precursor. Notably, both the diblock precursors and gradient precursors give very similar results in respect to the determined interfacial tensile strength.

5 Summary and Conclusions

In this thesis, a polymeric interphase was developed in order to improve the mechanical properties of glass/polyepoxide model system. The polymeric interphase was composed of sol-gel active hybrid inorganic/organic diblock and gradient copolymers between the glass and polyepoxide interface was introduced in order to enhance the interfacial adhesion between both phases. The design principle of the polymeric interphase was inspired by the tendon-to-bone insertion site, which links to mechanically different tissues. The mechanism of the enhancement of the interfacial adhesion relies on to chemical and physical attachment of the polymeric precursor to both phases.

For this purpose, a series of hybrid inorganic/organic copolymers with block and gradient microstructures were synthesized by employing CDTSPA mediated RAFT polymerizations in 1,4-dioxane. The hybrid inorganic/organic copolymers were composed of masked HEMA (THP–HEMA) as epoxy compatible and TESPMA as glass surface compatible component. The synthesis of P(THP–HEMA)-PTESPMA diblock copolymers was accomplished by using a THP–HEMA based MacroCTA approach. This two-step MacroCTA approach yielded well-defined diblock copolymers with narrow MWD and three different TESPMA block lengths. To synthesize well-defined gradient copolymers composed of THP–HEMA/TESPMA, the copolymerization kinetics of the given comonomer system was investigated in detail in order to gain detailed information over copolymerization kinetics in batch. In addition, the reactivity ratios were estimated by using a LSNF as well as KTM and EKTM, giving reactivity ratios for both monomers close to one. According to these investigations, the batch copolymerization of THP-HEMA/TESPMA yields exclusively ideal random copolymers. To overcome this limitation, the synthesis of gradient copolymers was accomplished by using a semi-batch forced gradient approach, in which a mixture of THP–HEMA was continuously feeded with 1M TESPMA solution. Due to the inherent reactivity of the comonomers, the steepness of the gradient microstructure could be altered by changing the TESPMA feeding to higher feeding rates. The semi-batch forced gradient approach enabled the preparation of well-defined gradient copolymers with reasonable narrow MWDs. In addition, the semi-batch forced gradient approach give rise to a greater variety of gradient compositions profiles as well as is not limited to a specific comonomer pair with appropriated reactivity ratio as compared to a spontaneous gradient approach. Due to the sol-gel active Si-OCH_2CH_3 motifs, the spontaneous formation of silica networks was observed in bulk. Thus, the polymeric

precursors were stored in anhydrous THF in order to inhibit the spontaneous gelation of the Si-OCH_2CH_3 motifs.

Next, the synthesized block copolymers with three different TESPMA block lengths and two gradient copolymers with diverse gradient microstructures were employed as polymeric precursor to fabricate sol-gel derived hybrid films on glass substrates. The formation of hybrid films on the glass substrates was accomplished by using a base and acid mediated sol-gel grafting-*onto* spin-coating approach. The former base catalyzed process yielded hybrid films with film thicknesses from 100 to 300 nm. Notably, the hybrid film thicknesses decreased upon treatment with methanolic 0.1M PTSA solution in order to cleave the THP groups from the hybrid film surface. These observations are attributed to shrinkage of the hybrid films upon post-crosslinking of non-reacted Si-OH motifs as well as evaporation of residual solvent. In general, the film thickness could be altered by using precursor with a higher incorporated TESPMA fraction or longer TESPMA block length. To further prove the structural identity of the hybrid films, IRRAS and XPS spectra were recorded. These studies revealed that pedant THP groups were successfully cleaved upon treatment with methanolic PTSA solution.

Lastly, a custom-built glass slide-model system was developed, wherein two coated glass slides were stitched with a bisphenol A glycidyl ether-based epoxy resin together. To prove the micromechanical properties of such a model system, mode I tensile tests were conducted and compared with a reference test sample. Based on the experimental data of this tests, the interfacial adhesion strength was relatively increased between 11.9% and 51.1%. The relative increase of the adhesion strength was mainly governed by the hybrid films thicknesses and grafting densities. Thus, hybrid films with a film thickness of ≤ 100 nm and a rather low grafting density result in a stronger interfacial adhesion as compared to thicker hybrid films with a high grafting density. These observations are presumably attributed to an insufficient interpenetration of the PHEMA chains into epoxy resin due to a high chain density. Interestingly, the composition of the polymeric precursor as well as film composition had no crucial impact on the strengthening mechanisms on the nanometer-scale. Following these findings, the hypothesis that a gradient-like macromolecular interphase on a nanometer-scale is highly desirable in order to maximize the interfacial adhesion is not valid. However, these observations might alter by approaching thick hybrid films of ≥ 1000 nm, in which the structural differences of the individual hybrid films are more pronounced. Thus, further experiments should focus on the thicker films with a higher level of film inhomogeneity and spatial resolution. Most likely, such micrometer thick films reveal different film characteristics as compared to the

nanometer thick films and the strengthening mechanism is more dominated by structural factors as well as by the inherent mechanical properties of the polymeric interphase.

In conclusion, the introduction of macromolecular interphase in a composite-like glass-polyepoxide system has an immanent impact on the mechanical properties. According to the mode I tensile tests, a nanometer thick polymeric interphase composed of block and gradient inorganic/organic copolymers results in an increased interfacial adhesion, due to physical and chemical attachment of tethered polymer chains to both phases. The adhesion between both phases is directly related to the interpenetration of the PHEMA chains into the epoxy resin and thus, a high interfacial adhesion is accomplished by a high level of interpenetrated PHEMA chains. To achieve this, it is advantageous to fabricate thin hybrid films of ≤100 nm and rather low grafting densities of 0.11 chains nm^{-2}. These requirements are sufficiently accomplished by using diblock inorganic/organic copolymers as precursors.

5 Zusammenfassung und Fazit

In der vorliegenden Arbeit wurde eine polymerbasierte Interphase entwickelt um die mechanischen Eigenschaften eines Glass/Polyepoxid Modellsystem zu verbessern. Dazu wurde an der Grenzfläche zwischen Glas und Epoxid-Harz eine polymere Interphase, bestehend aus hybrid anorganischen/organischen Block- und Gradientkopolymeren eingeführt, um die Haftung zwischen diesen beiden Phasen zu erhöhen. Das Designprinzip dieser polymeren Interphase war inspiriert bei der Knochen-Gelenkband-Insertionsstelle, welche zwei mechanisch unterschiedliche Gewebe miteinander verknüpft. Der Mechanismus der Erhöhung der Grenzflächenhaftung beruht auf der chemischen und physikalischen Verknüpfung beider Phasen durch polymere Haftvermittler.

Zu diesem Zweck wurde eine Reihe von hybrid anorganischen/organischen Block- und Gradientkopolymeren, bestehend aus „maskierten“ HEMA (THP–HEMA) als Epoxidharzkompatible Komponente und TESPMA als glaskompatible Komponente, mit Hilfe von CDTSPA vermittelter RAFT Polymerisation in 1,4-Dioxan synthetisiert. Zur Synthese von linearen P(THP–HEMA)-PTESPMA Diblockkopolymeren wurde ein THP–HEMA basiertes MacroCTA-Syntheseverfahren verwendet. Dieses zweistufige MacroCTA-Syntheseverfahren ergab wohldefinierte Diblockkopolymere mit variierenden TESPMA Blocklängen und einer schmalen Molmassenverteilung. Da die Synthese von Gradientkopolymeren ein tieferes Verständnis der Kopolymerisationskinetik des gegebenen Komonomersystem erforderte, wurden detaillierte Kinetikstudien in Lösung durchgeführt. Außerdem wurden die Reaktivitätsverhältnisse des gegebenen Monomerpaares mit Hilfe der LSNF, der KTM sowie der EKTM Methode bestimmt. Basierend auf diesen Ergebnissen liefert die Kopolymerisation von THP–HEMA und TESPMA in Lösung ausschließlich Kopolymere mit einer rein zufällig statistisch verteilten Kopolymerkomposition. Daher wurde die Synthese von Gradientkopolymeren mit Hilfe des Semi-Batch-Gradientkopolymerisationsverfahrens durchgeführt in der zu einer Reaktionslösung bestehend aus 1M THP-HEMA-Lösung kontinuierlich eine 1M TESPMA-Lösung hinzugetropft wurde. Aufgrund der gegebenen Reaktivitätsverhältnisse des Monomerpaares konnte das Kompositionsprofil der Gradientkopolymere mit Hilfe der TESPMA-Zutropfgeschwindigkeit variiert werden. Da im Semi-Batch-Kopolymerisationsverfahren das Kompositionsprofil nicht über die Reaktivitätsverhältnisse des Monomerpaares gesteuert wird, wie im spontanen Gradientkopolymerisationsverfahren, erlaubt es die Synthese von einer größeren Vielzahl

an Gradientkopolymeren mit unterschiedlichen Kompositionsprofilen. Aufgrund der Reaktivität der Sol-Gel aktiven Si-OCH_2CH_3 Gruppen kam es in zur spontanen Bildung von Silica-Klustern in Lösung. Um dies zu verhindern wurde die gereinigten Kopolymere in wasserfreiem THF gelagert.

Die synthetisierten Blockkopolymeren mit drei verschiedenen TESPMA Blocklängen und zwei Gradientkopolymere mit unterschiedlichen Kompositionsprofilen wurden als polymere Ausgangsstufen verwendet, um Sol-Gel basierte Hybridfilme auf Glassubtraten herzustellen. Die Sol-Gel-Beschichtung wurde sowohl unter basischen als auch sauren Bedingungen mit Hilfe des Grafting-*onto*-Verfahrens durchgeführt. Der letztere basenkatalysierte Prozess ergab Hybridfilme mit Schichtdicken von 100 bis 300 nm. Die auf der Oberfläche lokalisierten THP-Gruppen wurden mit Hilfe von mit 0.1M PTSA Lösung in Methanol gespalten, welches zu einer Reduzierung der Schichtdicke der Hybridfilme führte. Diese Beobachtungen sind auf das Schrumpfen der Hybridfilme beim Nachvernetzen nicht umgesetzter Si-OH-Motive sowie auf das Verdampfen von restlichen Lösungsmittels zurückgeführen. Im Allgemeinen konnte die Filmdicke durch Verwendung einer polymeren Ausgangsstufe mit einer größeren TESPMA-Anteil oder einer längeren TESPMA Blocklänge verändert werden. Um die strukturelle Identität der Hybridfilme weiter zu untersuchen, wurden IRRAS- und XPS-Spektren aufgenommen. Diese Studien zeigten, dass die freien THP-Gruppen nach Behandlung mit PTSA-Lösung in Methanol erfolgreich abgespalten wurden.

Zuletzt wurde ein speziell angefertigtes Glasobjektträger-Modellsystem entwickelt, bei den zwei beschichteten Objektträgern mit einem Epoxidharz auf Bisphenol-A-Glycidylether-Basis zusammengeklebt wurden. Um die mikromechanischen Eigenschaften eines solchen Modellsystems zu untersuchen, wurden Mode I Zugversuche durchgeführt und mit einer Referenzprobe verglichen. Basierend auf den experimentellen Ergebnissen dieser Tests war die Grenzflächenhaftung relativ zwischen 11,9% und 51,1% erhöht. Die relative Erhöhung der Haftfestigkeit wurde hauptsächlich durch die Hybridfilmdicken und Pfropfdichten bestimmt. So führen Hybridfilme mit einer Filmdicke von ≤ 100 nm und einer eher geringen Pfropfdichte zu einer stärkeren Grenzflächenhaftung im Vergleich zu dickeren Hybridfilmen mit einer hohen Pfropfdichte. Diese Beobachtungen werden vermutlich auf eine unzureichende Durchdringung der PHEMA-Ketten mit Epoxidharz aufgrund einer hohen Kettendichte zurückgeführt. Interessanterweise hatte die Zusammensetzung des polymeren Vorläufers sowie der Filmzusammensetzung keinen entscheidenden Einfluss auf die Verstärkungsmechanismen im Nanometerbereich. Auf Basis dieser Erkenntnisse ist die

Hypothese, dass eine gradientenartige makromolekulare nanoskalige Interphase im vorteilhaft ist, um die Grenzflächenhaftung zu maximieren, nicht gültig. Diese Beobachtungen könnten sich jedoch bei dickeren Hybridfilme von ≥ 1000 nm ändern, bei denen die strukturellen Unterschiede der Hybridfilme stärker sind. Weitere Experimente sollten sich daher auf dickere Filme mit einem höheren Grad an Filminhomogenität und räumlicher Auflösung konzentrieren. Höchstwahrscheinlich weisen solche mikrometerdicken Schichten im Vergleich zu nanometerdicken Schichten andere Filmeigenschaften auf, und der Verstärkungsmechanismus wird stärker von strukturellen Faktoren sowie von den inhärenten mechanischen Eigenschaften der polymeren Zwischenphase dominiert.

Insgesamt hat die Einführung der makromolekularen Interphase in ein Modell Glas -Polyepoxid-System einen immanenten Einfluss auf die mechanischen Eigenschaften. Gemäß der Mode I Zugversuche führt eine nanometerdicke polymere Interphase aus anorganisch/organischen Block- und Gradientkopolymeren zu einer erhöhten Grenzflächenhaftung, da beide Phasen physikalisch und chemisch über Polymerketten miteinander verbunden sind. Die Haftung zwischen beiden Phasen steht in direktem Zusammenhang mit der gegenseitigen Durchdringung der PHEMA-Ketten in das Epoxidharz, und somit wird eine hohe Grenzflächenadhäsion durch einen hohen Anteil von durchdrungenen PHEMA-Ketten erreicht. Dabei ist es vorteilhaft, dünne Hybridfilme von ≤ 100 nm und eher niedrige Pfropfdichten von 0,11 Polymerketten nm^{-2} herzustellen. Diese Anforderungen werden durch die Verwendung von anorganisch/organischen Diblockkopolymeren als polymere Ausgangsstufen ausreichend erfüllt.

6 Experimental Part

6.1 Materials

4-cyano-4-[(dodecylsulfanylthiocarbonyl)sulfanyl]pentanoic acid (CDTSPA, 97%, Aldrich), 4-cyano-4-(phenylcarbonothioylthio)pentanoic acid (CBPA, 97%, Aldrich), 3,4-dihydro-2*H*-pyrane (DHP, 97%, Aldrich), sodium hydroxide (NaOH, 99%, Fisher Scientific), hydrochloric acid (HCl, 37%, Merck), glacial acetic acid (AcOH, 99%, Merck), p-toluenesulfonic acid monohydrate (PTSA, 99%, Merck), pyridine (99%, Chemsolute), methanol (pure, 99%, Chemsolute), ethanol (pure, 99%, Chemsolute), ethyl actetate (HPLC grade, Chemsolute), tetrahydrofurane (THF, pure, 99%, Chemsolute), diethyl ether (99%, Fisher Scientific), tetrahydrofurane (extry dry, water < 50 ppm, Acros Organics), 1,4-dioxane (extra dry, 99.8%, Acros Organics), dichloromethane (anhydrous, 99.8%, Aldrich) were used without further purification. Azobisisobutyronitrile (AIBN, 95%, Merck) was recrystallized from methanol two times before use. Triethylamine (TEA, 99%, Aldrich) was distilled under reduced pressure before use. The monomer 2-hydroxyethyl methacrylate (HEMA, 98%, ABCR) was used as received, whereas 3-(triethoxysilyl) propyl methacrylate (TESPMA, 97%, ABCR) and 3-(triisopropoxysilyl) propyl methacrylate (IPSMA, 95%, ABCR) were distilled under reduced pressure before use. The synthesis of pyridinium p-toluenesulfonate (PPTS) is reported elsewhere.[140]

6.2 Polymer characterization

6.2.1 Gel permeation chromatography

M_n and $Đ$ values of PTHP–HEMA, PTHP–HEMA-*b*-PTESPMA, PTHP–HEMA-*b*-PIPSPMA, PTHP–HEMA-*stat*-PTESPMA and PTHP–HEMA-*grad*-PTESPMA (co)polymers were obtained at 25 °C by gel-permeation chromatography (GPC) equipped with a Thermo Separation Products (TSP) isocratic pump P-100/1000, Shodex RI-71 detector and a PSS-SDV 5µ VS column. Linear polymethyl methacrylate standards were applied as calibration. THF was used as eluent at a flow rate of 1.0 mL min^{-1}.

6.2.2 NMR Spectroscopy

^{1}H-NMR and ^{13}C-NMR spectra were recorded in $CDCl_3$ and DMSO-d_6 on a Bruker DPX 400 or Bruker AVANCE 500 at 300 K, and TMS (δ = 0.00) was used as the internal

reference. All monomer conversions were estimated by ^{1}H-NMR analysis with the samples directly taken at a given time interval.

6.2.3 Mass spectrometry

Mass spectra were recorded on a HPLC-MS Agilent 6210 System equipped with an analytical Agilent 1100 HPLC System, and an ESI-MSD TOF detector of Agilent Technologies.

6.2.4 ATR-Infrared spectroscopy

IR spectra were recorded on a Nicolet FTIR spectrometer from ThermoFisher Scientific equipped with a diamond ATR at room temperature.

6.2.5 Differential scanning calorimetry

Differential scanning calorimetry (DSC) measurements were conducted on a Hitachi EXSTAR SII DSC 7020 under a nitrogen atmosphere using a heating rate of 10 °C min^{-1} from –60 to 160 °C. Four cycles were recorded for each sample. The glass transition temperature (T_g) values correspond to the average T_g values of the three last heating cycles.

6.2.6 Thermogravimetric analysis

Thermogravimetric analysis (TGA) was conducted under a nitrogen atmosphere on a Mettler Toledo TGA/SDTA 851^{e} in the range of 25 °C to 600 °C with a heating rate of 10 °C min^{-1} and a nitrogen flow rate of 30 mL min^{-1}.

6.3 Surface characterization

6.3.1 Contact angle measurements

Water contact angle measurements were recorded on a Drop Shape Analyzer – DSA100S under atmospheric conditions. Eight water droplets were placed and analyzed along a diagonal on the substrate surfaces. Thus, the contact angles correspond to the average values of these eight values. The water contact angle measurements were carried out by Gundula Hidde (BAM 6.7).

6.3.2 Atomic force microscopy

The AFM topographies were recorded by Mario Sahre (BAM 6.7) on Scanning Probe Microscope Dimension 3100 AFM, Digital Instruments GmbH (Bruker) Measurement oscillating in intermittent contact, probe: silicon (NCLR, NanoSensors), nominal radius 10 nm; Resonant frequency approx. 170 kHz, amplitude attenuation approx. 5%; 512 x 256 measurement points. The film thicknesses and RMS roughnesses were estimated via software supported data analysis (Gwydion 2.4.1).

6.3.3 X-ray photoelectron spectroscopy

The hybrid films were characterized via XPS on a Sage 150 Spektrometer. Survey spectra were acquired at constant pass energy, and the elemental quantification was conducted by using software supported surface analysis. The high-resolution scans of core level of carbon were recorded at lower pass energy. The XPS measurements and data analysis were conducted by Dr. Korinna Altmann (BAM 6.6).

6.3.4 Infrared external reflection spectroscopy

IRRAS spectra were recorded on a Nicolet FTIR spectrometer from ThermoFisher Scientific equipped with a variable-angle reflection attachment. The angle of incidence was set to 84°. Due to the low IR reflectivity of the glass substrate, the glass slides were sputtered with gold (layer thickness ~ 40 nm) and treated with atmospheric-pressure plasma for 15 min at a current of 1.49 A.

6.4 Synthesis

All reactions were conducted under anhydrous conditions under nitrogen atmosphere. The reaction vessels were dried at 150 °C overnight to remove traces of water. All RAFT mediated polymerizations were carried out under strict exclusion of oxygen to prevent retardation during the polymerization, due to the biradical character of molecular oxygen.

6.4.1 Preparation of 0.05M AIBN stock-solution

A Schlenk flask was charged with AIBN (164 mg, 1.0 mmol) and tightly sealed with a rubber septum. The solid AIBN was dissolved in 1,4-dioxane (20 mL) and the solution was degassed by bubbling nitrogen through the solution for 30 min at room temperature.

6.4.2 Preparation of 1M TESPMA stock-solution

In a Schlenk flask equipped with a stirring bar and sealed with a rubber septum TESPMA (5.9 mL, 20 mmol) was added and dissolved in 1,4-dioxane (20 mL). The solution was degassed by bubbling nitrogen through the solution for 30 min at room temperature.

6.4.3 Synthesis of 2-tetrahydropyranylethyl methacrylate

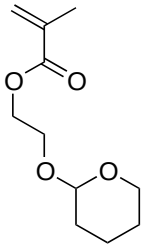

PPTS (2.1 g, 8.2 mmol) was added to a solution of HEMA (10 mL, 82.4 mmol) in dichloromethane (30 mL), followed by addition of DHP (11.3 mL, 123.6 mmol). The colorless mixture was stirred for 4 h at room temperature. After stirring, the mixture was diluted in diethyl ether (100 mL), washed with half-saturated brine (3 x 100 mL) and dried over $MgSO_4$. The organic layer was concentrated in *vacuo* and purified by flash column chromatography (ethyl acetate, 1 *Vol*.-% TEA) to afford the product in a racemic mixture as yellowish liquid. (16.4 g, 76.5 mmol, 92.8%). R_f = 0.8 (ethyl acetate, 1 *Vol.*-% TEA). **^{1}H-NMR (DMSO-*d*$_6$, 400 MHz):** δ = 6.11–5.98 (m, 1H), 5.74–5.66 (m, 1H), 4.66–4.62 (m, 1H), 4.39–4.14 (m, 2H), 3.90–3.37 (m, 4H), 1.89 (s, 3H), 1.77–1.36 (m, 6H) ppm. **^{13}C-NMR (DMSO-*d*$_6$, 101 MHz):** δ = 166.71 (s), 136.04 (s), 125.99 (s), 98.02 (s), 64.73 (s), 63.93 (s), 61.28 (s), 30.29 (s), 25.19 (s), 19.12 (s), 18.18 (s). **MS (ESI):** *m / z* 237 $[M + Na]^+$.

6.4.4 Synthesis of poly-2-tetrahydropyranylethyl methacrylate via CBPA mediated RAFT polymerization

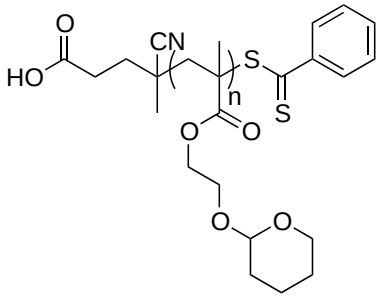

A Schlenk tube equipped with a stirring bar was charged with CBPA (28 mg, 0.1 mmol), tightly sealed with a rubber septum and CBPA was dissolved in 1,4-dioxane (10 mL). THP–HEMA (2.16 mL, 10 mmol) was added to the solution and the mixture was degassed by three freeze-pump-thaw cycles. Next, the mixture was immersed in a pre-heated oil bath

(T = 60, 70, 80 °C) and equilibrated for 15 min. To start the polymerization a degassed 0.05 M AIBN stock-solution in 1,4-dioxane (0.5 mL, 0.025 mmol) was syringed into the reaction mixture. After 24 h of stirring, the reaction mixture was cooled down in a water/ice bath and exposed to air to terminate the polymerization. Then, 1,4-dioxane was evaporated at reduced pressure to afford the crude product. The crude product was re-dissolved in THF (≈ 5 mL), precipitated into cold methanol (≈ 40 mL) three times and dried under reduced pressure at 40 °C overnight to afford the product as pinkish solid. (Yield ≈ 70–80%) **(DMSO-*d*$_6$, 400 MHz):** δ = 4.68–4.57 (m, 1H), 4.17–3.94 (m, 2H), 3.86–3.70 (m, 2H), 3.65–3.40 (m, 2H), 1.95–1.40 (m, 6H), 1.10–0.75 (m, 3H) ppm. **IR (ATR, cm^{-1}):** 2940 (ν_{as} (CH_2, CH_3)), 2870 (ν_s (CH_2, CH_3)), 1719 (ν (C=O)), 1260 (ν (C-O)), 1140 (ν (C-O-C)), 1074 (δ_{as} (C-O)) cm^{-1}.

6.4.5 Synthesis of poly-2-tetrahydropyranylethyl methacrylate via CDTSPA-mediated RAFT polymerization

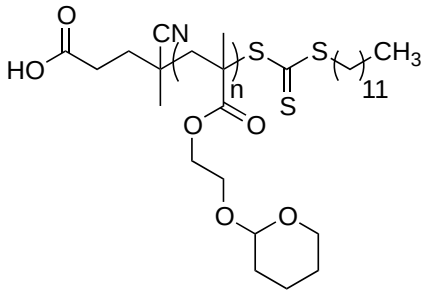

A Schlenk tube equipped with a stirring bar was charged with CDTSPA (0.041 mg, 0.1 mmol), tightly sealed with a rubber septum and CDTSPA was dissolved in 1,4-dioxane (10 mL). To the solution was added THP–HEMA (2.16 mL, 10 mmol) and the mixture was degassed by three freeze-pump-thaw cycles. Next, the mixture was immersed in a pre-heated oil bath (T = 60, 70, 80 °C) and equilibrated for 15 min. To start the polymerization a degassed 0.05 M AIBN stock-solution in 1,4-dioxane (0.5 mL, 0.025 mmol) was syringed into the reaction mixture. After 24 h of stirring, the reaction mixture was cooled down in a water/ice bath and exposed to air to terminate the polymerization. Then, 1,4-dioxane was evaporated at reduced pressure to afford the crude product. The crude product was re-dissolved in THF (≈ 5 mL), precipitated into cold methanol (≈ 40 mL) three times and dried under reduced pressure at 40 °C overnight to afford the product as yellowish solid. (Yield ≈ 80%) **(DMSO-*d*$_6$, 400 MHz):** δ = 4.68–4.57 (m), 4.17–3.94 (m), 3.86–3.70 (m), 3.65–3.40 (m), 1.95–1.40 (m), 1.10–0.75 (m) ppm. **IR (ATR, cm^{-1}):** 2940 (ν_{as} (CH_2, CH_3)), 2870 (ν_s (CH_2, CH_3)), 1719 (ν (C=O)), 1260 (ν (C-O)), 1140 (ν (C-O-C)), 1074 (δ_{as} (C-O)) cm^{-1}. T_g: (3.7 ± 1) °C.

6.4.6 Synthesis of poly-2-tetrahydropyranylethyl methacrylate-*block*-poly-3-(triethoxysilyl) propyl methacrylate

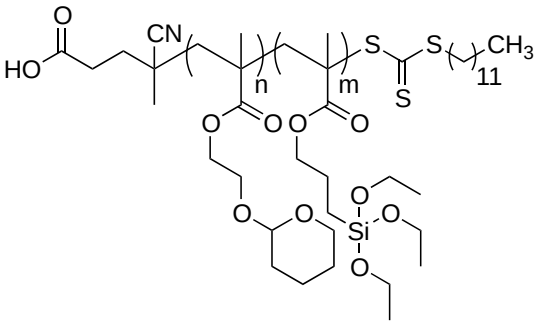

A Schlenk tube equipped with a stirring bar was charged with P(THP–HEMA)-MacroCTA (M_{nNMR} = 20.4 kDa, 695 mg, 0.034 mmol), tightly sealed with a rubber septum and dissolved in 1,4-dioxane (5 mL). TESPMA (1.0 mL, 3.4 mmol, DP_{Target} = 100; 0.5 mL, 1.7 mmol, DP_{Target} = 50; 0.25 mL, 0.85 mmol, DP_{Target} = 25) was added to the solution and the mixture was degassed by three freeze-pump-thaw cycles. Next, the mixture was immersed in a pre-heated oil bath (T = 60, 70, 80 °C) and equilibrated for 15 min. To start the polymerization a degassed 0.05 M AIBN stock-solution in 1,4-dioxane (0.34 mL, 0.017 mmol) was syringed into the reaction mixture. After 24 h of stirring, the reaction mixture was cooled down in a water/ice bath and exposed to air to terminate the polymerization. Then, 1,4-dioxane was evaporated at reduced pressure to afford the crude product. The crude product was re-dissolved in THF (≈ 2.5 mL), precipitated into a cold methanol/water (70/30) mixture (≈ 40 mL) three times and dried under reduced pressure at 40 °C for 2 h to afford the product as yellowish solid. (Yield ≈ 70%) The pure product was stored in anhydrous THF at a concentration of 100 mg mL^{-1} to inhibit the formation of silica aggregates. **($CDCl_3$, 400 MHz):** δ = 4.68–4.57 (m), 4.20–4.02 (m), 3.95–3.77 (m), 3.68–3.46 (m), 2.09–1.48 (m), 1.28–1.17 (m), 1.12–0.76 (m), 0.68–0.54 (m) ppm. **IR (ATR, cm^{-1}):** 2926 (ν_{as} (CH_2, CH_3)), 2880 (ν_s (CH_2, CH_3)), 1726 (ν (C=O)), 1154 (ν (C-O)), , 1074 (δ_{as} (C-O)), 1035/803 (ν (Si-O species)) cm^{-1}.

6.4.7 Synthesis of poly-2-tetrahydropyranylethyl methacrylate-*block*-poly-3-(triisopropoxysilyl) propyl methacrylate

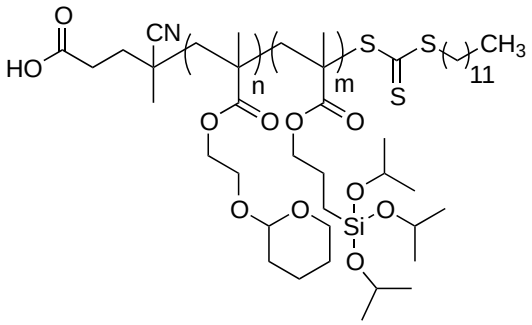

A Schlenk tube equipped with a stirring bar was charged with P(THP–HEMA)-MacroCTA (M_{nNMR} = 20.4 kDa, 695 mg, 0.034 mmol), tightly sealed with a rubber septum and the polymer dissolved in 1,4-dioxane (5 mL). IPSMA (1.20 mL, 3.4 mmol, DP_{Target} = 100; 0.6 mL, 1.7 mmol, DP_{Target} = 50; 0.3 mL, 0.85 mmol, DP_{Target} = 25) was added to the solution and the mixture was degassed by three freeze-pump-thaw cycles. Next, the mixture was immersed in a pre-heated oil bath at 60 °C and equilibrated for 15 min. To start the polymerization a degassed 0.05 M AIBN stock-solution in 1,4-dioxane (0.34 mL, 0.017 mmol) was syringed into the reaction mixture. After 24 h of stirring, the reaction mixture was cooled down in a water/ice bath and exposed to air to terminate the polymerization. Then, 1,4-dioxane was evaporated at reduced pressure to afford the crude product. The crude product was re-dissolved in THF (≈2.5 mL), precipitated into a cold methanol/water (70/30) mixture (≈ 40 mL) three times and dried under reduced pressure at 40 °C for 2 h to afford the product as yellowish solid. (Yield ≈ 70%) The pure product was stored in anhydrous THF at a concentration of 100 mg mL^{-1} to inhibit the formation of silica aggregates. **($CDCl_3$, 400 MHz):** δ = 4.68–4.59 (m), 4.29–4.05 (m), 3.91–3.78 (m), 3.67–3.46 (m), 2.02–1.48 (m), 1.25–1.12 (m) 1.10–0.78 (m), 0.60–0.49 (m) ppm. **IR (ATR, cm^{-1}):** 2926 (ν_{as} (CH_2, CH_3)), 2880 (ν_s (CH_2, CH_3)), 1726 (ν (C=O)), 1214 (ν (C-$(CH_3)_2$), 1154 (ν (C-O)), 1074 (δ_{as} (C-O)), 1035/824/788 (ν (Si-O species)) cm^{-1}.

6.4.6 Synthesis of poly-2-tetrahydropyranylethyl methacrylate-*statistical*-poly-3-(triethoxysilyl) propyl methacrylate

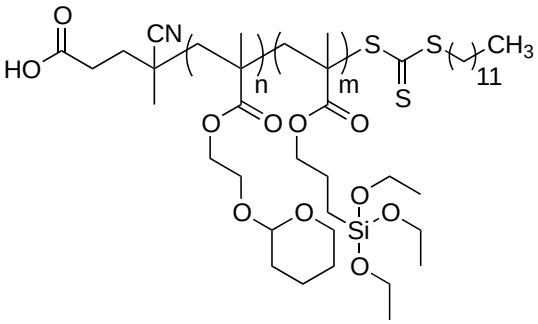

A Schlenk flask equipped with a stirring bar was charged with CDTSPA (40 mg, 0.1 mmol), tightly sealed with a rubber septum and dissolved in 1,4-dioxane (10 mL). THP–HEMA and TESPMA were added to the solution, as detailed in Table 20 and 21, degassed by bubbling argon through the mixture for 30 min at room temperature and immersed in a pre-heated oil bath at 60 °C.

Table 20. Experimental conditions for THP–HEMA.

THP–HEMA:TESPMA	$M_{THP–HEMA}$ (g mol$_{-1}$)	$m_{THP–HEMA}$ (g)	$n_{THP–HEMA}$ (mmol)	$V_{THP–HEMA}$ (mL)
5:1	214.26	1.78	8.33	1.78
3:1	214.26	1.61	7.50	1.60
1:1	214.26	1.07	5.00	1.06
1:3	214.26	0.54	2.50	0.53
1:5	214.26	0.36	1.67	0.35

Table 21. Experimental conditions for TESPMA.

THP–HEMA:TESPMA	M_{TESPMA} (g mol$_{-1}$)	m_{TESPMA} (g)	n_{TESPMA} (mmol)	V_{TESPMA} (mL)
1:5	290.43	2.42	8.33	2.47
1:3	290.43	2.17	7.50	2.22
1:1	290.43	1.45	5.00	1.48
3:1	290.43	0.73	2.50	0.74
5:1	290.43	0.49	1.67	0.49

After 15 min of pre-equilibration, an aliquot of a degassed 0.05 M AIBN stock-solution in 1,4-dioxane (0.5 mL, 0.025 mmol) was added to start the reaction. After 24 h of stirring, the reaction mixture was cooled down in a water/ice bath and exposed to air to terminate the polymerization. Then, 1,4-dioxane was evaporated at reduced pressure to afford the crude product. The crude product was re-dissolved in THF (≈5 mL), precipitated into a cold methanol/water (70/30) mixture (≈ 40 mL) three times and dried under reduced pressure at 40 °C for 2 h to afford the product as yellowish solid. (Yield ≈ 70%) The pure product was stored in anhydrous THF at a concentration of 100 mg mL^{-1} to inhibit the formation of silica aggregates. **($CDCl_3$, 400 MHz):** δ = 4.68–4.57 (m), 4.20–4.02 (m), 3.95–3.77 (m), 3.68–3.46 (m), 2.09–1.48 (m), 1.28–1.17 (m), 1.12–0.76 (m), 0.68–0.54 (m) ppm. **IR (ATR, cm^{-1}):** 2926 (ν_{as} (CH_2, CH_3)), 2880 (ν_s (CH_2, CH_3)), 1726 (ν (C=O)), 1154 (ν (C-O)), 1074 (δ_{as} (C-O)), 1035/803 (ν (Si-O species)) cm^{-1}.

6.4.8 Synthesis of blocky poly-2-tetrahydropyranylethyl methacrylate-*gradient*-poly-3-(triethoxysilyl) propyl methacrylate

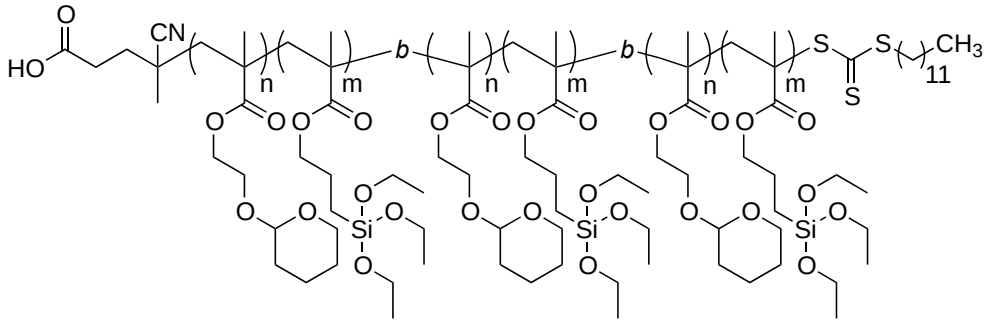

A Schlenk flask equipped with a stirring bar was charged with CDTSPA (40 mg, 0.1 mmol), tightly sealed with a rubber septum and dissolved in 1,4-dioxane (10 mL). To the solution was added THP–HEMA (1.6 mL, 7.5 mmol) and TESPMA (0.74, 2.5 mmol), degassed by bubbling argon through the mixture for 30 min at room temperature and immersed in a pre-heated oil bath at 60 °C. After 15 min of pre-equilibration, was added an aliquot of a degassed 0.05 M AIBN stock-solution in 1,4-dioxane (0.5 mL, 0.025 mmol) to start the reaction. After 3.5 h and 7 h reaction time, a degassed 1 M solution of TESPMA in 1,4-dioxane (2.5 mL, 2.5 mmol) was syringed into the reaction mixture. After 24 h of stirring, the reaction mixture was cooled down in a water/ice bath and exposed to air to terminate the polymerization. Then, 1,4-dioxane was evaporated at reduced pressure to afford the crude product. The crude product was re-dissolved in THF (≈5 mL), precipitated into a cold methanol/water (70/30) mixture (≈ 40 mL) three times and dried under reduced pressure at 40 °C for 2 h to afford the product as yellowish solid. (Yield ≈ 70%) The pure

product was stored in anhydrous THF at a concentration of 100 mg mL^{-1} to inhibit the formation of silica aggregates. **($CDCl_3$, 400 MHz):** δ = 4.68–4.57 (m), 4.20–4.02 (m), 3.95–3.77 (m), 3.68–3.46 (m), 2.09–1.48 (m), 1.28–1.17 (m), 1.12–0.76 (m), 0.68–0.54 (m) ppm. **IR (ATR, cm^{-1}):** 2926 (ν_{as} (CH_2, CH_3)), 2880 (ν_s (CH_2, CH_3)), 1726 (ν (C=O)), 1154 (ν (C-O)), 1074 (δ_{as} (C-O)), 1035/803 (ν (Si-O species)) cm^{-1}.

6.4.9 Synthesis of poly-2-tetrahydropyranylethyl methacrylate-*gradient*-poly-3-(triethoxysilyl) propyl methacrylate

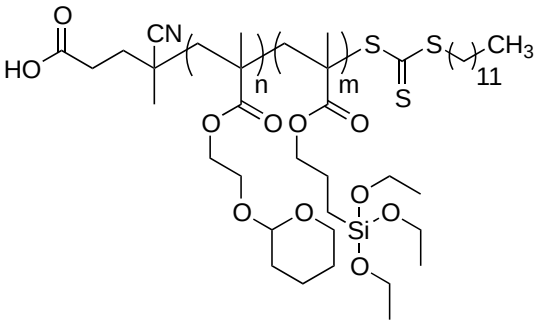

A Schlenk flask equipped with a stirring bar was charged with CDTSPA (40 mg, 0.1 mmol), tightly sealed with a rubber septum and dissolved in 1,4-dioxane (7.5 mL). THP–HEMA (1.6 mL, 7.5 mmol) was added to the solution, degassed by bubbling argon through the mixture for 30 min at room temperature and immersed in a pre-heated oil bath (T = 70 or 80 °C). Using an air tight syringe a degassed 1M solution of TESPMA in 1,4-dioxane (7.5 mL) was transferred and connected via a flexible needle to the Schlenk flask. After addition of an aliquot of a degassed 0.05 M AIBN stock-solution in 1,4-dioxane (0.5 mL, 0.025 mmol), the 1M TESPMA stock solution was continuously added to the copolymerization mixture by using a WPI NE-1000 programmable single syringe pump. After 24 h of stirring, the reaction mixture was cooled down in a water/ice bath and exposed to air to terminate the polymerization. Then, 1,4-dioxane was evaporated at reduced pressure to afford the crude product. The crude product was re-dissolved in THF (≈5 mL), precipitated into a cold methanol/water (70/30) mixture (≈ 40 mL) three times and dried under reduced pressure at 40 °C for 2 h to afford the product as yellowish solid. (Yield ≈ 70%) The pure product was stored in anhydrous THF at a concentration of 100 mg mL^{-1} to inhibit the formation of silica aggregates. **($CDCl_3$, 400 MHz):** δ = 4.68–4.57 (m), 4.20–4.02 (m), 3.95–3.77 (m), 3.68–3.46 (m), 2.09–1.48 (m), 1.28–1.17 (m), 1.12–0.76 (m), 0.68–0.54 (m) ppm. **IR (ATR, cm^{-1}):** 2926 (ν_{as} (CH_2, CH_3)), 2880 (ν_s (CH_2, CH_3)), 1726 (ν (C=O)), 1154 (ν (C-O)), 1074 (δ_{as} (C-O)), 1035/803 (ν (Si-O species)) cm^{-1}.

6.4.7 Acid catalyzed deprotection of P(THP–HEMA)

Into a flask equipped with a stirring bar and a rubber septum PTHP–HEMA (1.00 g, M_{nNMR} = 20.4 kDa) was placed. The deprotection of the THP-moieties was adapted from previously reported procedures as follows:

A) P(THP–HEMA) was dissolved in methanol (10 mL) and PTSA (0.19 g, 1 mmol). was added to the solution. Next, the solution was stirred at room temperature for 24 h.[153]
B) P(THP–HEMA) was dissolved in an AcOH/THF/water mixture (9.5 mL) in a ratio of 4/2/1. Next, the mixture was stirred at 45 °C for 24 h.[154]
C) P(THP–HEMA) was dissolved in ethanol (10 mL) and PPTS (0.25 g, 1 mmol) was added to the solution. Next, the solution was stirred at 55 °C for 24 h.[140]

After stirring, the polymer mixture was transferred into a dialysis tube and dialyzed against ethanol at room temperature over three days. After purification a white solid was obtained. **(DMSO-d_6, 400 MHz):** δ = 4.88–4.77 (m), 4.00–3.82 (m), 3.70–3.51 (m), 2.08–1.67 (m), 1.02–0.68 (m) ppm. **IR (ATR, cm^{-1}):** 3401 (ν (hydrated O-H)), 2945 (ν_{as} (CH_2, CH_3)), 2876 (ν_s (CH_2, CH_3)), 1719 (ν (C=O)), 1248 (ν (C-O)), 1151 (δ_{as} (C-O)) cm^{-1}. T_g: (79.8 ± 1) °C.

6.5 Sol-gel grafting-*onto* spin-coating

Spin-coating was carried out at room temperature by using a SPIN 150i Spin Coater from SPS Europe equipped with a vacuum chuck to mechanically hold the glass substrate. As glass substrates cover slips (size: 18 x 18 mm, thickness: 0.5-0.6 mm) from Menzel Gläser were used.

6.5.1 Glass surface immobilization

The cover slips were immersed in freshly prepared piranha acid for 30 min at room temperature and then, thoroughly washed with deionized water. The wet cover slips were dried at room temperature overnight.

6.5.2 Copolymer solution preparation

From a P(THP–HEMA-*grad*-PTESPMA) (c ≈ 100 mg mL_{-1}) stock solution in anhydrous THF an aliquot (0.5 mL) was taken an aliquot (0.5 mL) and diluted with THF (0.4 mL). To the copolymer solution deionized water (0.1 mL) was added yielding a copolymer concentration of 50 mg mL_{-1}. Next, the copolymer solution was passed through a Mircropur GF syringe filter (pore size: 1.0 µm, filter-∅: 25 mm, vendor: Altmann Analytik) to remove dust and copolymer aggregates from the solution, and to the solution was added 1M HCl or 1M NaOH (2-3 droplets) as catalyst.

6.5.3 General procedure

The immobilized glass substrates were placed in the center of the chuck holder and mechanically fixed by applying vacuum to the substrate. Next, on the center of the glass substrate a droplet of THF (150 µL) was added and the glass substrate was rotated for 60 sec. at 3000 rpm to remove residual impurities from the glass surface. Then, a droplet of freshly prepared copolymer solution (150 µL) was added on the center of the glass substrate and the glass substrate was rotated again for 60 sec. at 3000 rpm. The thin copolymer films were dried at 40 °C overnight.

6.5.4 Acid catalyzed cleavage of THP groups on a glass substrate

The hybrid inorganic/organic copolymer coated glass slide was immersed in a 0.1M PTSA solution in methanol (5 mL) and gently shake at room temperature for 24 h. Next, the coated glass slide was thoroughly washed with deionized water and dried at 40 °C overnight.

6.6 Micromechanical analysis

For the preparation of test samples, spin-coated glass slides were used that were carefully dried before use at room temperature (~ 1 week). Next, between two coated glass slides was placed a 1 mm thick PTFE-foil (18 mm x 18 mm) as spacer to give an epoxy resin volume (V_{Epoxy}) of 90 mm_3 and an epoxy resin area (A_{Epoxy}) of 90 mm_2. The sample was fixed with a stainless-steel clamp and immersed in the low viscosity epoxy resin. Due to capillary forces and adhesive forces the low viscosity epoxy resin was sucked into the cavity between the two glass slides, as shown in Figure 48A. The low viscosity epoxy resin was composed of Hexion EPIKOTE Resin MGS RIM 135 as resin and Hexion EPIKURE CuringAgent MGS RIM H 137 as hardener (resin : hardener = 3.33 : 1 by weight). To prevent the formation of bubbles and other inhomogeneities within the epoxy resin, both

components were slowly mixed with a stirring bar on a magnetic stirrer over 1 h at room temperature. The curing of the epoxy resin was accomplished at 100 °C for 2 h, as reported previously. [147, 148] After curing, the sample was allowed to cool down to room temperature and the PTFE-foil was carefully removed. Then, the sample was mounted between two metal holders by using a UHU Plus 2-K-Epoxide glue, as demonstrated in Figure 48B.

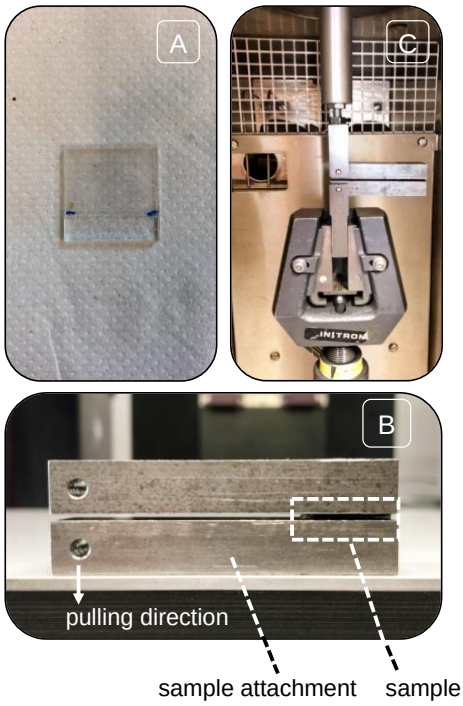

Figure 48. A) Image of glass-model-sample after curing of the epoxy resin. B) Image of the metal holders used to attach the sample to the Zwick 1454 tensile testing set-up. C) Custom-built setup for the measurement of force-displacement-curves on a Zwick 1454 tensile testing machine.

The glue was allowed to cure over three days at room temperature. The mode 1 tensile tests were carried out with a custom-built setup on a Zwick 1454 tensile testing machine under ambient conditions, as demonstrated in Figure 47C. The tensile ramp (υ) was set to 0.5 mm min_{-1} and the maximum displacement to 1 mm. The measurements were recorded under the guidance of Dr. Gerhard Kalinka (BAM 5.3) and Lothar Buchta (BAM 5.3). Three force-displacement-curves for each sample were recorded. Consequently, the F_{max} and τ_{max} values correspond to the average values of these three measurements.

7 Appendix

7.1 NMR Spectra

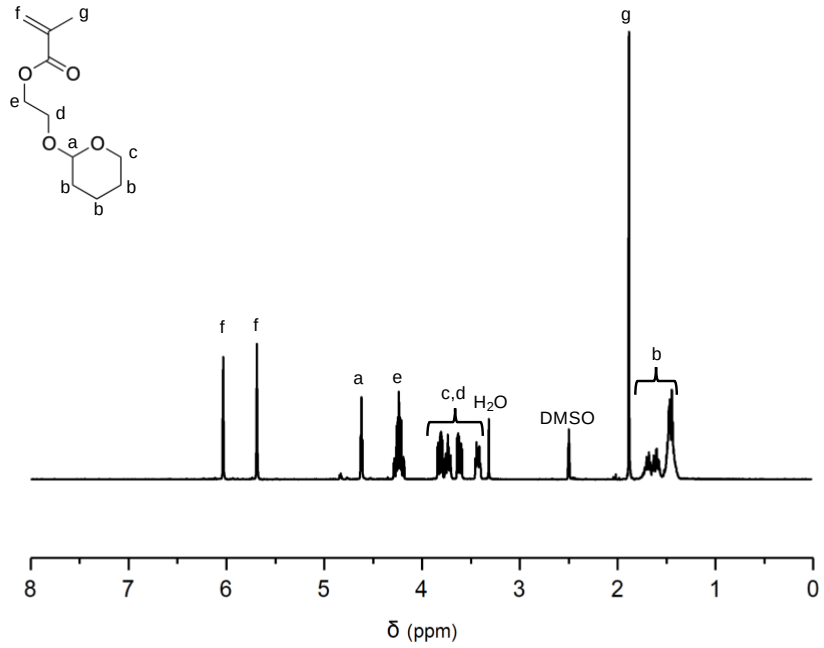

Figure 49. $_1$H NMR spectrum of THP–HEMA in DMSO-*d*$_6$.

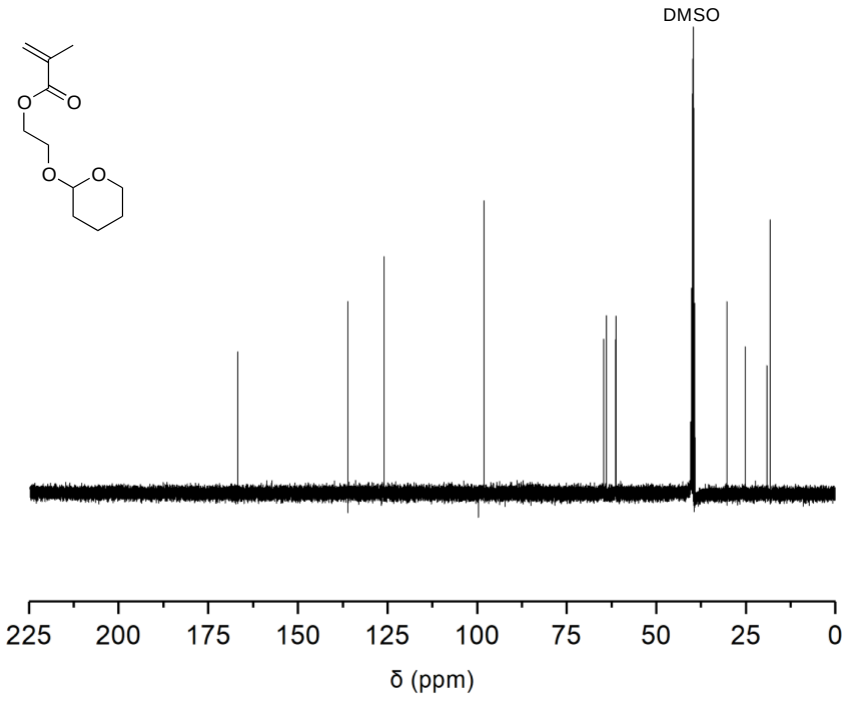

Figure 50. $_{13}$C NMR Spectrum of THP–HEMA in DMSO-*d*$_6$.

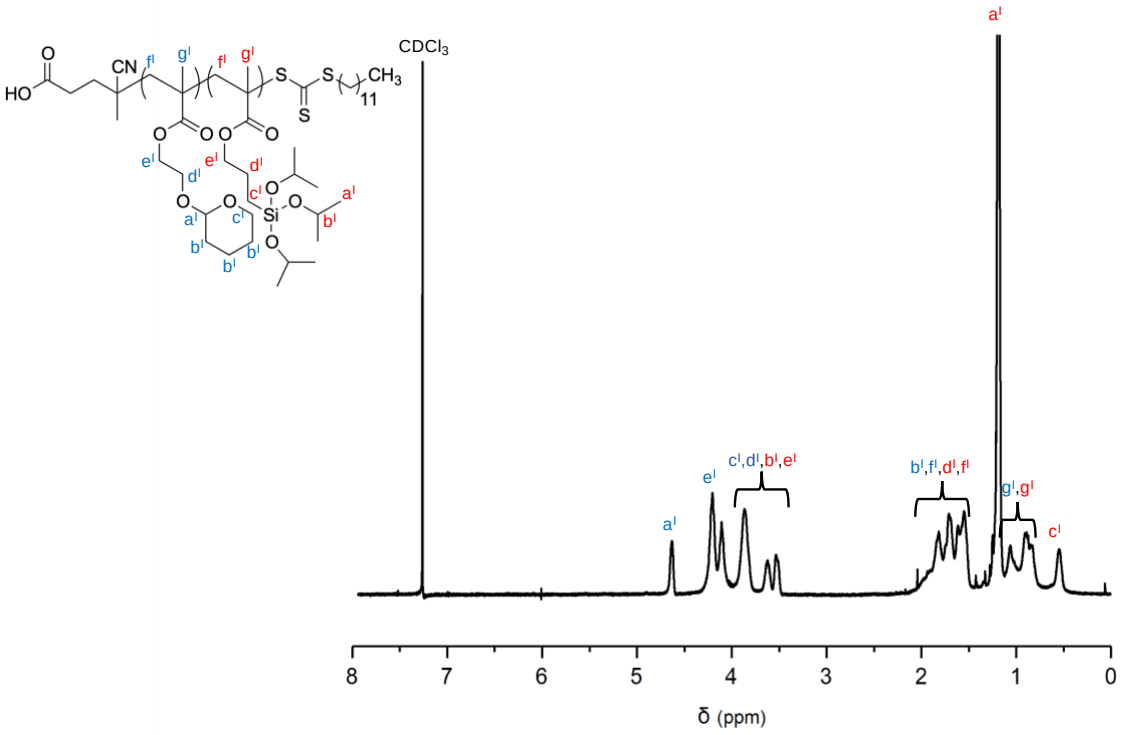

Figure 51. $_{1}$H NMR spectrum of P(THP–HEMA)-*b*-PIPSMA in CDCl$_3$.

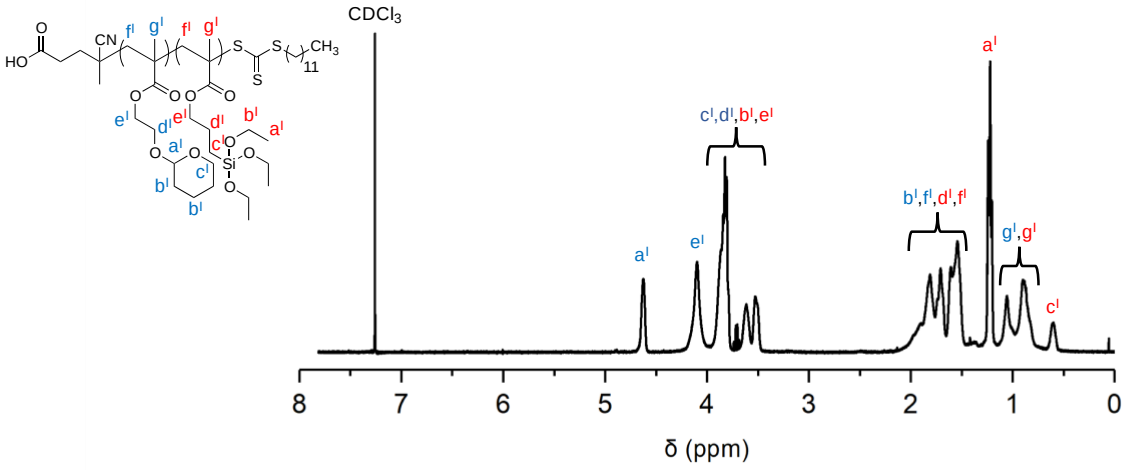

Figure 52. $_{1}$H NMR spectrum of P(THP–HEMA)-*grad*-PTESPMA in CDCl$_3$.

7.2 Mass Spectra

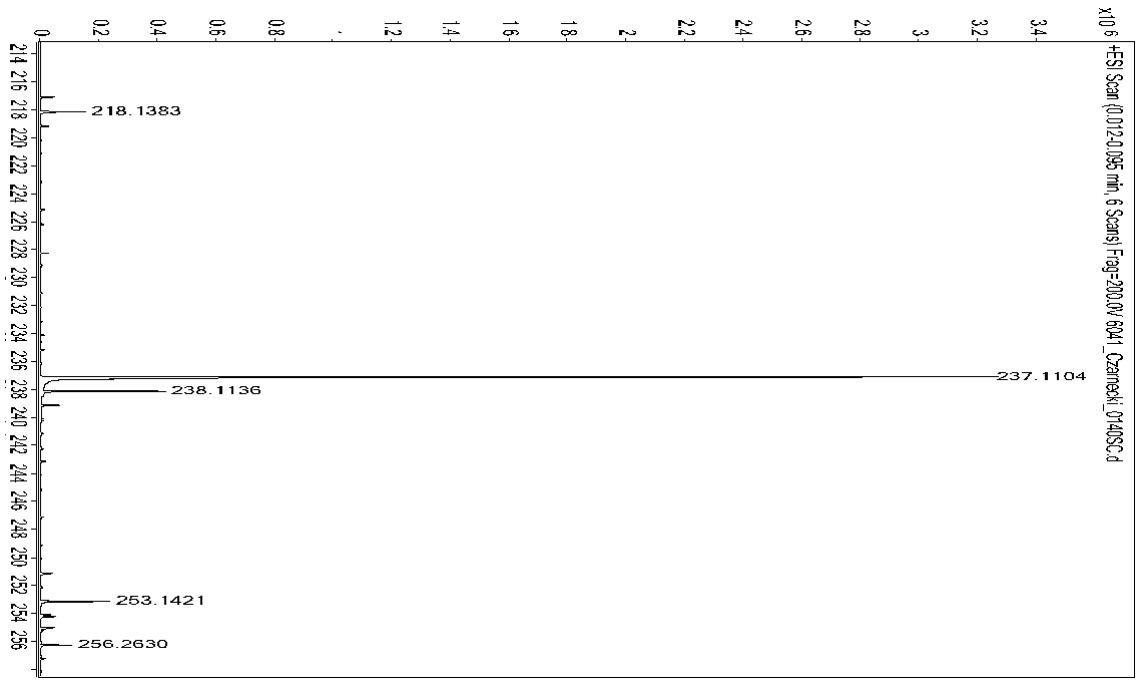

Figure 53. Mass spectrum of THP–HEMA.

7.3 IR spectra

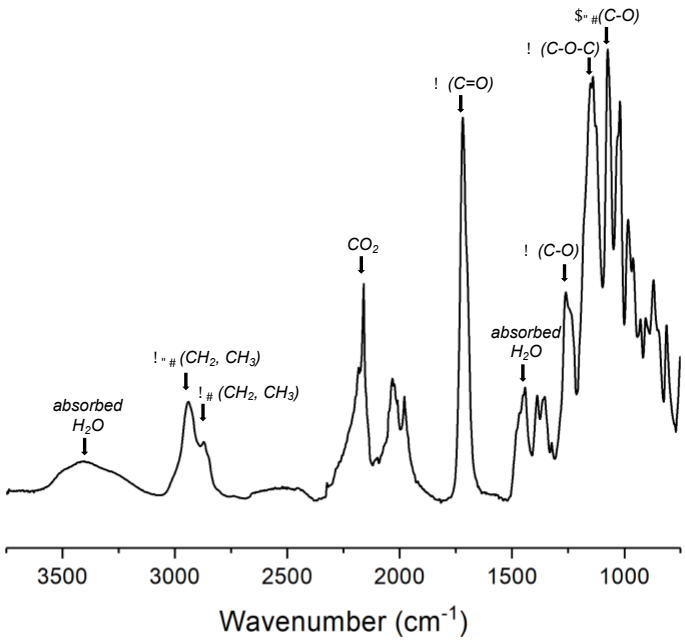

Figure 54. Absorbance IR-ATR spectrum of P(THP–HEMA).

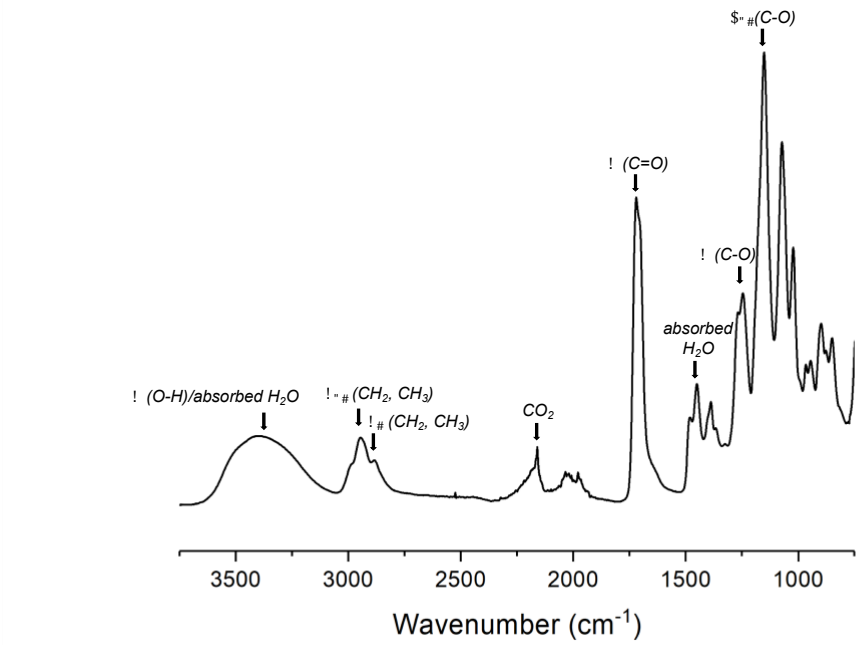

Figure 55. Absorbance IR-ATR spectrum of deprotected P(THP–HEMA).

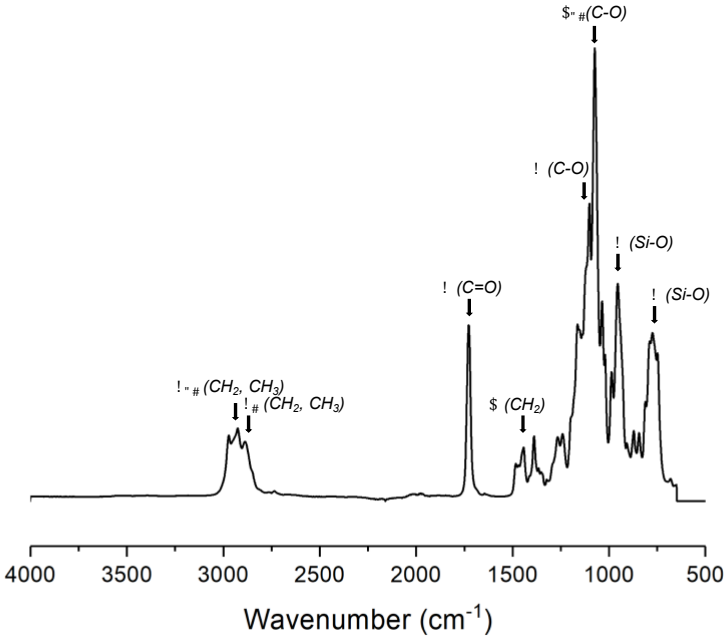

Figure 56. Absorbance IR-ATR spectrum of P(THP–HEMA)-*b*-PTESPMA.

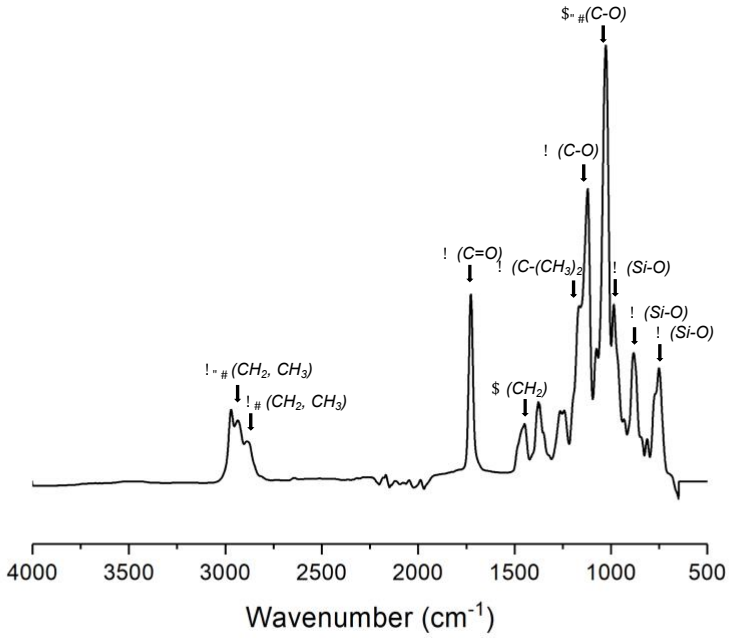

Figure 57. Absorbance IR-ATR spectrum of P(THP–HEMA)-*b*-PIPSMA.

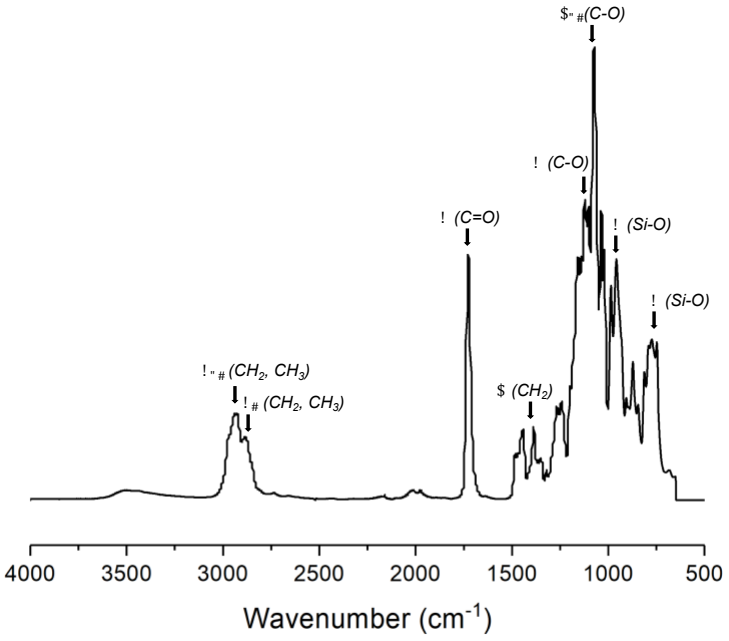

Figure 58. Absorbance IR-ATR spectrum of P(THP–HEMA)-*stat/grad*-PTESP

8 References

1. Singh, J., et al., *Properties of Glass-Fiber Hybrid Composites: A Review.* Polymer-Plastics Technology and Engineering, 2016. **56**(5): p. 455-469.
2. Vaithylingam, R., M.N.M. Ansari, and R.A. Shanks, *Recent Advances in Polyurethane-Based Nanocomposites: A Review.* Polymer-Plastics Technology and Engineering, 2017: p. 1-14.
3. Froes, F.H., *Advanced Materials in Sports Equipment*, in *Handbook of Materials Selection*. 2007, John Wiley & Sons, Inc. p. 1253-1273.
4. Sathishkumar, T.P., S. Satheeshkumar, and J. Naveen, *Glass fiber-reinforced polymer composites – a review.* Journal of Reinforced Plastics and Composites, 2014. **33**(13): p. 1258-1275.
5. Drzal, L.T. *The interphase in epoxy composites*. in *Epoxy Resins and Composites II*. 1986. Berlin, Heidelberg: Springer Berlin Heidelberg.
6. Duchet, J., et al., *Influence of the Deposition Process on the Structure of Grafted Alkylsilane Layers.* Langmuir, 1997. **13**(8): p. 2271-2278.
7. Drown, E.K., H. Al Moussawi, and L.T. Drzal, *Glass fiber 'sizings' and their role in fiber-matrix adhesion.* Journal of Adhesion Science and Technology, 1991. **5**(10): p. 865-881.
8. Shokoohi, S., A. Arefazar, and R. Khosrokhavar, *Silane Coupling Agents in Polymer-based Reinforced Composites: A Review.* Journal of Reinforced Plastics and Composites, 2008. **27**(5): p. 473-485.
9. Feller, J.F. and Y. Grohens, *Coupling ability of silane grafted poly(propene) at glass fibers/poly(propene) interface.* Composites Part A: Applied Science and Manufacturing, 2004. **35**(1): p. 1-10.
10. Trey, S.M., et al., *Glass fiber reinforced high glass transition temperature thiol–ene networks.* Composites Part A: Applied Science and Manufacturing, 2011. **42**(11): p. 1800-1808.
11. Kuttner, C., et al., *Photochemical Synthesis of Polymeric Fiber Coatings and Their Embedding in Matrix Material: Morphology and Nanomechanical Properties at the Fiber–Matrix Interface.* ACS Applied Materials & Interfaces, 2012. **4**(7): p. 3484-3492.
12. Kuttner, C., et al., *Influence of the polymeric interphase design on the interfacial properties of (fiber-reinforced) composites.* ACS Appl Mater Interfaces, 2013. **5**(7): p. 2469-78.
13. Oréfice, R.L., A.E. Clark, and A.B. Brennan, *Bioactive composites with designed interphases based on hyperbranched macromers.* Journal of Applied Polymer Science, 2006. **99**(3): p. 1153-1166.
14. Gupta, H.S., et al., *Nanoscale Deformation Mechanisms in Bone.* Nano Letters, 2005. **5**(10): p. 2108-2111.
15. Dunlop, J.W., et al., *New suggestions for the mechanical control of bone remodeling.* Calcif Tissue Int, 2009. **85**(1): p. 45-54.
16. Wagermaier, W., et al., *Spiral twisting of fiber orientation inside bone lamellae.* Biointerphases, 2006. **1**(1): p. 1-5.
17. Paris, O., I. Burgert, and P. Fratzl, *Biomimetics and Biotemplating of Natural Materials.* MRS Bulletin, 2011. **35**(3): p. 219-225.
18. Cosgrove, D.J., *Growth of the plant cell wall.* Nat Rev Mol Cell Biol, 2005. **6**(11): p. 850-61.
19. Salmén, L. and I. Burgert, *Cell wall features with regard to mechanical performance. A review COST Action E35 2004–2008: Wood machining – micromechanics and fracture.* Holzforschung, 2009. **63**(2).
20. Fratzl, P., I. Burgert, and H.S. Gupta, *On the role of interface polymers for the mechanics of natural polymeric composites.* Physical Chemistry Chemical Physics, 2004. **6**(24).

21. Genin, G.M., et al., *Functional grading of mineral and collagen in the attachment of tendon to bone.* Biophys J, 2009. **97**(4): p. 976-85.
22. Sanchez, C., et al., *Applications of hybrid organic–inorganic nanocomposites.* Journal of Materials Chemistry, 2005. **15**(35-36): p. 3559.
23. Faustini, M., et al., *History of Organic-Inorganic Hybrid Materials: Prehistory, Art, Science, and Advanced Applications.* Advanced Functional Materials, 2018. **28**(27): p. 1704158.
24. Czarnecki, S. and A. Bertin, *Hybrid Silicon-Based Organic/Inorganic Block Copolymers with Sol-Gel Active Moieties: Synthetic Advances, Self-Assembly and Applications in Biomedicine and Materials Science.* Chemistry - A European Journal, 2018.
25. Zhang, K., L. Gao, and Y. Chen, *Organic−Inorganic Hybrid Materials by Self-Gelation of Block Copolymer Assembly and Nanoobjects with Controlled Shapes Thereof.* Macromolecules, 2007. **40**(16): p. 5916-5922.
26. Gamys, C.G., E. Beyou, and E. Bourgeat-Lami, *Micellar behavior of well-defined polystyrene-based block copolymers with triethoxysilyl reactive groups and their hydrolysisâ□“condensation.* Journal of Polymer Science Part A: Polymer Chemistry, 2010. **48**(4): p. 784-793.
27. Gamys, C.G., et al., *SAXS and SANS characterization of gelable polystyrene-b-poly(acryloxy propyl triethoxysilane) (PS-b-PAPTES) diblock copolymer micelles before and after hydrolysis–condensation.* Soft Matter, 2012. **8**(24): p. 6564.
28. Gamys, C.G., et al., *Tunable Morphologies From Bulk Self-Assemblies of Poly(acryloxypropyl triethoxysilane)-b-poly(styrene)-b-poly(acryloxypropyl triethoxysilane) Triblock Copolymers.* Macromolecular Chemistry and Physics, 2012. **213**(1): p. 10-18.
29. Gamys, C.G., et al., *Nanostructured organic-inorganic hybrid films prepared by the sol-gel method from self-assemblies of PS-b-paptes-b-PS triblock copolymers.* Journal of Polymer Science Part A: Polymer Chemistry, 2011: p. n/a-n/a.
30. Gao, L., K. Zhang, and Y. Chen, *Functionalization of shaped polymeric nanoobjects via bulk co-self-assembling gelable block copolymers with silane coupling agents.* Polymer, 2011. **52**(17): p. 3681-3686.
31. Feng, C., et al., *A versatile strategy for uniform hybrid nanoparticles and nanocapsules.* Polym. Chem., 2015. **6**(29): p. 5190-5197.
32. Park, J.-W. and E.L. Thomas, *A Surface-Reactive Rod-Coil Diblock Copolymer: Nano- and Micropatterned Polymer Brushes.* Journal of the American Chemical Society, 2002. **124**(4): p. 514-515.
33. Park, J.-W. and E.L. Thomas, *Anisotropic Micellar Nanoobjects from Reactive Liquid Crystalline Rod−Coil Diblock Copolymers.* Macromolecules, 2004. **37**(10): p. 3532-3535.
34. Park, J.W. and E.L. Thomas, *Multiple Ordering Transitions: Hierarchical Self-Assembly of Rod–Coil Block Copolymers.* Advanced Materials, 2003. **15**(78): p. 585-588.
35. Mellon, V., et al., *Block Copolymers of γ-Methacryloxypropyltrimethoxysilane and Methyl Methacrylate by RAFT Polymerization. A New Class of Polymeric Precursors for the Sol−Gel Process.* Macromolecules, 2005. **38**(5): p. 1591-1598.
36. Chung, J.J., J.R. Jones, and T.K. Georgiou, *Toward Hybrid Materials: Group Transfer Polymerization of 3-(Trimethoxysilyl)propyl Methacrylate.* Macromol Rapid Commun, 2015. **36**(20): p. 1806-9.
37. Huang, H., et al., *Synthesis and comparison of two poly (methyl methacrylate-b-3-(trimethoxysilyl)propyl methacrylate)/SiO2 hybrids by "grafting-to" approach.* J Colloid Interface Sci, 2014. **433**: p. 133-40.
38. Koh, K., et al., *Synthesis of well-defined polymers with protected silanol groups by atom transfer radical polymerization and their use for the fabrication of polymeric nanoparticles.* European Polymer Journal, 2004. **40**(12): p. 2665-2670.
39. Xiong, D., G. Liu, and E.J. Scott Duncan, *Robust amphiphobic coatings from bi-functional silica particles on flat substrates.* Polymer, 2013. **54**(12): p. 3008-3016.
40. Xiong, D., G. Liu, and E.J. Duncan, *Simultaneous coating of silica particles by two diblock copolymers.* ACS Appl Mater Interfaces, 2012. **4**(5): p. 2445-54.

41. Li, W., et al., *Amphiphilic Hybrid Nano Building Blocks with Surfactant-Mimicking Structures.* ACS Macro Letters, 2015. **4**(7): p. 736-740.
42. Teo, G.H., et al., *Self-assembly of block copolymers with an alkoxysilane-based core-forming block: A comparison of synthetic approaches.* Journal of Polymer Science Part A: Polymer Chemistry, 2017.
43. Teo, G.H., et al., *Polymer-inorganic hybrid nanoparticles of various morphologies via polymerization-induced self assembly and sol–gel chemistry.* Polym. Chem., 2016. **7**(43): p. 6575-6585.
44. Teo, G.H., P.B. Zetterlund, and S.C. Thickett, *Interfacial crosslinking of self-assembled triblock copolymer nanoparticles via alkoxysilane hydrolysis and condensation.* Journal of Polymer Science Part A: Polymer Chemistry, 2018.
45. Zhou, J., et al., *Preparation of organic/inorganic hybrid nanomaterials using aggregates of poly(stearyl methacrylate)-b-poly(3-(trimethoxysilyl) propyl methacrylate) as precursor.* European Polymer Journal, 2007. **43**(5): p. 1736-1743.
46. Zhou, J., et al., *Preparation of organic/inorganic hybrid nanomaterials using aggregates of star block copolymer consisting of poly(stearyl methacrylate) and poly(3-(trimethoxysilyl) propyl methacrylate) as precursor.* Journal of Applied Polymer Science, 2008. **108**(3): p. 2010-2016.
47. Huang, Y., et al., *A Versatile Approach to Different Colored Photonic Films Generated from Block Copolymers and Their Conversion into Polymer-Grafted Nanoplatelets.* J. Mater. Chem. C, 2017.
48. Junfeng, Z., et al., *Preparation of organic/inorganic hybrid nanoballs using aggregates of PTMSPMA-b-PSMA-Fc-PSMA-b-PTMSPMA block copolymers as precursors.* Nanotechnology, 2006. **17**(11): p. 2745.
49. Han, M., et al., *Surface-Grafted Rodlike Polymers: Adaptive Self-Assembled Monolayers and Rapid Photo-Patterning of Surfaces.* Chemistry of Materials, 2011. **23**(15): p. 3517-3524.
50. Xiong, D., et al., *Superamphiphobic Diblock Copolymer Coatings.* Chemistry of Materials, 2011. **23**(19): p. 4357-4366.
51. Macoretta, D., et al., *Clear antismudge unimolecular coatings of diblock copolymers on glass plates.* ACS Appl Mater Interfaces, 2014. **6**(23): p. 21435-45.
52. Grozea, C.M., et al., *Coating of silica particles by fluorinated diblock copolymers and use of the resultant silica for superamphiphobic surfaces.* Polymer, 2015. **64**: p. 153-162.
53. Shi, Z., et al., *Preparation of water-repellent cotton fabrics from fluorinated diblock copolymers and evaluation of their durability.* Polymer, 2013. **54**(23): p. 6406-6414.
54. Sun, Y. and W. Liu, *Preparation and properties of an organic–inorganic hybrid materials based on fluorinated block copolymer.* Journal of Materials Science, 2011. **47**(4): p. 1803-1810.
55. Rabnawaz, M., et al., *Synthesis of poly(dimethylsiloxane)-block-poly[3-(triisopropyloxysilyl) propyl methacrylate] and its use in the facile coating of hydrophilically patterned superhydrophobic fabrics.* RSC Adv., 2015. **5**(49): p. 39505-39511.
56. Wu, W.-C., et al., *Theoretical and Experimental Studies on the Surface Structures of Conjugated Rod−Coil Block Copolymer Brushes.* Langmuir, 2007. **23**(5): p. 2805-2814.
57. Wang, R., et al., *Controlled Radical Synthesis of Fluorene-Based Blue-Light-Emitting Copolymer Nanospheres with Core−Shell Structure via Self-Assembly.* Macromolecules, 2009. **42**(14): p. 4993-5000.
58. Du, J. and Y. Chen, *Atom-Transfer Radical Polymerization of a Reactive Monomer: 3-(Trimethoxysilyl)propyl Methacrylate.* Macromolecules, 2004. **37**(17): p. 6322-6328.
59. Du, J. and Y. Chen, *Hairy Nanospheres by Gelation of Reactive Block Copolymer Micelles.* Macromolecular Rapid Communications, 2005. **26**(6): p. 491-494.
60. Du, J., et al., *Organic/Inorganic Hybrid Vesicles Based on A Reactive Block Copolymer.* Journal of the American Chemical Society, 2003. **125**(48): p. 14710-14711.
61. Du, J. and Y. Chen, *Preparation of Organic/Inorganic Hybrid Hollow Particles Based on Gelation of Polymer Vesicles.* Macromolecules, 2004. **37**(15): p. 5710-5716.

62. Du, J. and Y. Chen, *Organic-inorganic hybrid nanoparticles with a complex hollow structure.* Angew Chem Int Ed Engl, 2004. **43**(38): p. 5084-7.
63. Xiong, M., Y. Chen, and M. Maskos, *Functionalization of Crosslinked Vesicles by Co-Self-Assembly of a Gelable Diblock Copolymer and Mercaptosilane.* Macromolecular Rapid Communications, 2008. **29**(16): p. 1368-1371.
64. Xiong, M., K. Zhang, and Y. Chen, *ATRP of 3-(triethoxysilyl)propyl methacrylate and preparation of "stable" gelable block copolymers.* European Polymer Journal, 2008. **44**(11): p. 3835-3841.
65. Li, W., et al., *Synthesis and Self-Assembly of Amphiphilic Hybrid Nano Building Blocks via Self-Collapse of Polymer Single Chains.* Macromolecules, 2014. **47**(17): p. 5932-5941.
66. Chen, H., et al., *Biocompatible polysiloxane-containing diblock copolymer PEO-b-PgammaMPS for coating magnetic nanoparticles.* ACS Appl Mater Interfaces, 2009. **1**(10): p. 2134-40.
67. Jia, F., F. Liang, and Z. Yang, *Janus Mesoporous Nanodisc from Gelable Triblock Copolymer.* ACS Macro Letters, 2016. **5**(12): p. 1344-1347.
68. Liu, M., et al., *Tunable Pickering Emulsions with Environmentally Responsive Hairy Silica Nanoparticles.* ACS Appl Mater Interfaces, 2016. **8**(47): p. 32250-32258.
69. Zou, P., G.-Y. Shi, and C.-Y. Pan, *Large-compound vesicle-encapsulated multiwalled carbon nanotubes: A unique route to nanotube composites.* Journal of Polymer Science Part A: Polymer Chemistry, 2009. **47**(14): p. 3669-3679.
70. Zhang, Q., et al., *Soft-nanocoupling between silica and gold nanoparticles based on block copolymer.* Reactive and Functional Polymers, 2017. **110**: p. 30-37.
71. Koh, K., et al., *Precision synthesis of organic/inorganic hybrid nanocapsules with a silanol-functionalized micelle template.* Angew Chem Int Ed Engl, 2003. **42**(35): p. 4194-7.
72. Yuan, J., et al., *Water-soluble organo-silica hybrid nanowires.* Nat Mater, 2008. **7**(9): p. 718-22.
73. Müllner, M., et al., *Water-Soluble Organo−Silica Hybrid Nanotubes Templated by Cylindrical Polymer Brushes.* Journal of the American Chemical Society, 2010. **132**(46): p. 16587-16592.
74. Yuan, B., et al., *Copolymer coatings consisting of 2-methacryloyloxyethyl phosphorylcholine and 3-methacryloxypropyl trimethoxysilane via ATRP to improve cellulose biocompatibility.* ACS Appl Mater Interfaces, 2012. **4**(8): p. 4031-9.
75. Zhang, K., et al., *Onionlike Spherical Polymer Composites with Controlled Dispersion of Gold Nanoclusters.* Chemistry of Materials, 2008. **20**(1): p. 23-25.
76. Gao, L., et al., *Core extractable nano-objects: Manipulating triblock copolymer micelles.* Journal of Polymer Science Part B: Polymer Physics, 2012. **50**(5): p. 323-327.
77. Zhang, K., et al., *Functional sandwich-like organic/inorganic nanoplates from gelable triblock terpolymers.* Journal of Materials Chemistry, 2009. **19**(21): p. 3482.
78. Zhang, K., L. Gao, and Y. Chen, *Organic/inorganic nanoobjects with controlled shapes from gelable triblock copolymers.* Polymer, 2010. **51**(13): p. 2809-2817.
79. Huang, J., et al., *Nonleaching Antibacterial Glass Surfaces via "Grafting Onto": The Effect of the Number of Quaternary Ammonium Groups on Biocidal Activity.* Langmuir, 2008. **24**(13): p. 6785-6795.
80. Yao, D., et al., *Shaped core/shell polymer nanoobjects with high antibacterial activities via block copolymer microphase separation.* Polymer, 2013. **54**(14): p. 3485-3491.
81. Du, J. and S.P. Armes, *pH-Responsive Vesicles Based on a Hydrolytically Self-Cross-Linkable Copolymer.* Journal of the American Chemical Society, 2005. **127**(37): p. 12800-12801.
82. Chang, C., et al., *Construction of mixed micelle with cross-linked core and dual responsive shells.* Polymer Chemistry, 2011. **2**(4): p. 923.
83. Zhang, Y., S. Luo, and S. Liu, *Fabrication of Hybrid Nanoparticles with Thermoresponsive Coronas via a Self-Assembling Approach.* Macromolecules, 2005. **38**(23): p. 9813-9820.

84. Macon, A.L., et al., *RAFT Polymerization of N-[3-(Trimethoxysilyl)-propyl]acrylamide and Its Versatile Use in Silica Hybrid Materials.* Macromol Rapid Commun, 2015. **36**(23): p. 2060-4.
85. Wei, H., et al., *Construction of temperature responsive hybrid crosslinked self-assemblies based on PEG-b-P(MMA-co-MPMA)-b-PNIPAAm triblock copolymer: ATRP synthesis and thermoinduced association behavior.* Journal of Polymer Science Part A: Polymer Chemistry, 2011. **49**(8): p. 1809-1820.
86. Chang, C., et al., *Temperature and pH Double Responsive Hybrid Cross-Linked Micelles Based on P(NIPAAm-co-MPMA)-b-P(DEA): RAFT Synthesis and "Schizophrenic" Micellization.* Macromolecules, 2009. **42**(13): p. 4838-4844.
87. Chang, C., et al., *Fabrication of thermoresponsive, core-crosslinked micelles based on poly[N-isopropyl acrylamide-co-3-(trimethoxysilyl)propylmethacrylate]-b-poly{N-[3-(dimethylamino)propyl]methacrylamide} for the codelivery of doxorubicin and nucleic acid.* Journal of Applied Polymer Science, 2015. **132**(15): p. n/a-n/a.
88. Hervault, A., et al., *Doxorubicin loaded dual pH- and thermo-responsive magnetic nanocarrier for combined magnetic hyperthermia and targeted controlled drug delivery applications.* Nanoscale, 2016. **8**(24): p. 12152-61.
89. Dunn, A.E., et al., *Spatial and temporal control of drug release through pH and alternating magnetic field induced breakage of Schiff base bonds.* Polym. Chem., 2014. **5**(10): p. 3311-3315.
90. Jones, J.R., *Review of bioactive glass: from Hench to hybrids.* Acta Biomater, 2013. **9**(1): p. 4457-86.
91. Chung, J.J., et al., *Biodegradable inorganic-organic hybrids of methacrylate star polymers for bone regeneration.* Acta Biomater, 2017. **54**: p. 411-418.
92. Chung, J.J., et al., *Tailoring Mechanical Properties of Sol–Gel Hybrids for Bone Regeneration through Polymer Structure.* Chemistry of Materials, 2016. **28**(17): p. 6127-6135.
93. Chung, J.J., et al., *Effect of Comonomers on Physical Properties and Cell Attachment to Silica-Methacrylate/Acrylate Hybrids for Bone Substitution.* Macromol Rapid Commun, 2017. **38**(15).
94. Chen, X., et al., *A facile synthesis of thermo-responsive Au–polymer hybrid microgels through temperature-induced co-aggregation and self-crosslinking.* Polymer Chemistry, 2015. **6**(33): p. 5989-5992.
95. Pardal, F., V. Lapinte, and J.-J. Robin, *Kinetics of cotelomerization of 3-(trimethoxysilyl)propyl methacrylate and perfluorodecylacrylate.* European Polymer Journal, 2009. **45**(4): p. 1198-1207.
96. Pardal, F., V. Lapinte, and J.-J. Robin, *Modification of silica nanoparticles by grafting of copolymers containing organosilane and fluorine moities.* Journal of Polymer Science Part A: Polymer Chemistry, 2009. **47**(18): p. 4617-4628.
97. Roh, D.K., et al., *Nanocomposite proton conducting membranes based on amphiphilic PVDF graft copolymer.* Macromolecular Research, 2010. **18**(3): p. 271-278.
98. Grubbs, R.B. and R.H. Grubbs, *50th Anniversary Perspective: Living Polymerization—Emphasizing the Molecule in Macromolecules.* Macromolecules, 2017.
99. Nicolas, J., et al., *Nitroxide-mediated polymerization.* Progress in Polymer Science, 2013. **38**(1): p. 63-235.
100. Krys, P. and K. Matyjaszewski, *Kinetics of Atom Transfer Radical Polymerization.* European Polymer Journal, 2017. **89**: p. 482-523.
101. Matyjaszewski, K. and N.V. Tsarevsky, *Macromolecular engineering by atom transfer radical polymerization.* J Am Chem Soc, 2014. **136**(18): p. 6513-33.
102. Perrier, S., *50th Anniversary Perspective: RAFT Polymerization—A User Guide.* Macromolecules, 2017. **50**(19): p. 7433-7447.
103. Hill, M.R., R.N. Carmean, and B.S. Sumerlin, *Expanding the Scope of RAFT Polymerization: Recent Advances and New Horizons.* Macromolecules, 2015. **48**(16): p. 5459-5469.

104. Pearson, S., et al., *Opportunities for dual RDRP agents in synthesizing novel polymeric materials.* Polym. Chem., 2017.
105. Barner-Kowollik, C., et al., *Mechanism and kinetics of dithiobenzoate-mediated RAFT polymerization. I. The current situation.* Journal of Polymer Science Part A: Polymer Chemistry, 2006. **44**(20): p. 5809-5831.
106. Moad, G., *Mechanism and Kinetics of Dithiobenzoate-Mediated RAFT Polymerization - Status of the Dilemma.* Macromolecular Chemistry and Physics, 2014. **215**(1): p. 9-26.
107. Barner-Kowollik, C. and G.T. Russell, *Chain-length-dependent termination in radical polymerization: Subtle revolution in tackling a long-standing challenge.* Progress in Polymer Science, 2009. **34**(11): p. 1211-1259.
108. Keddie, D.J., et al., *RAFT Agent Design and Synthesis.* Macromolecules, 2012. **45**(13): p. 5321-5342.
109. Mayo, F.R. and F.M. Lewis, *Copolymerization. I. A Basis for Comparing the Behavior of Monomers in Copolymerization; The Copolymerization of Styrene and Methyl Methacrylate.* Journal of the American Chemical Society, 1944. **66**(9): p. 1594-1601.
110. Fineman, M. and S.D. Ross, *Linear method for determining monomer reactivity ratios in copolymerization.* Journal of Polymer Science, 1950. **5**(2): p. 259-262.
111. Kelen, T. and F. TÜds, *Analysis of the Linear Methods for Determining Copolymerization Reactivity Ratios. I. A New Improved Linear Graphic Method.* Journal of Macromolecular Science: Part A - Chemistry, 1975. **9**(1): p. 1-27.
112. Tüdos, F., et al., *Analysis of Linear Methods for Determining Copolymerization Reactivity Ratios. III. Linear Graphic Method for Evaluating Data Obtained at High Conversion Levels.* Journal of Macromolecular Science: Part A - Chemistry, 2006. **10**(8): p. 1513-1540.
113. Keddie, D.J., *A guide to the synthesis of block copolymers using reversible-addition fragmentation chain transfer (RAFT) polymerization.* Chem Soc Rev, 2014. **43**(2): p. 496-505.
114. Zaremski, M.Y., D.I. Kalugin, and V.B. Golubev, *Gradient copolymers: Synthesis, structure, and properties.* Polymer Science Series A, 2009. **51**(1): p. 103-122.
115. Beginn, U., *Gradient copolymers.* Colloid and Polymer Science, 2008. **286**(13): p. 1465-1474.
116. Steinhauer, W., et al., *Block and Gradient Copolymers of 2-Hydroxyethyl Acrylate and 2-Methoxyethyl Acrylate via RAFT: Polymerization Kinetics, Thermoresponsive Properties, and Micellization.* Macromolecules, 2013. **46**(4): p. 1447-1460.
117. Steinhauer, W., et al., *Copolymerization of 2-Hydroxyethyl Acrylate and 2-Methoxyethyl Acrylate via RAFT: Kinetics and Thermoresponsive Properties.* Macromolecules, 2010. **43**(17): p. 7041-7047.
118. Guo, Y., et al., *Tailor-made compositional gradient copolymer by a many-shot RAFT emulsion polymerization method.* Polym. Chem., 2014. **5**(10): p. 3363-3371.
119. Figueira, R., et al., *Hybrid Sol-Gel Coatings: Smart and Green Materials for Corrosion Mitigation.* Coatings, 2016. **6**(1): p. 12.
120. Danks, A.E., S.R. Hall, and Z. Schnepp, *The evolution of 'sol–gel' chemistry as a technique for materials synthesis.* Mater. Horiz., 2016. **3**(2): p. 91-112.
121. Moore, J.C., *Gel permeation chromatography. I. A new method for molecular weight distribution of high polymers.* Journal of Polymer Science Part A: General Papers, 1964. **2**(2): p. 835-843.
122. Izunobi, J.U. and C.L. Higginbotham, *Polymer Molecular Weight Analysis by1H NMR Spectroscopy.* Journal of Chemical Education, 2011. **88**(8): p. 1098-1104.
123. Coats, A.W. and J.P. Redfern, *Thermogravimetric analysis. A review.* Analyst, 1963. **88**(1053): p. 906-924.
124. Chiu, M. and E. Prenner, *Differential scanning calorimetry: An invaluable tool for a detailed thermodynamic characterization of macromolecules and their interactions.* Journal of Pharmacy And Bioallied Sciences, 2011. **3**(1): p. 39-59.

125. Kwok, D.Y., et al., *Contact Angle Measurements and Contact Angle Interpretation. 1. Contact Angle Measurements by Axisymmetric Drop Shape Analysis and a Goniometer Sessile Drop Technique.* Langmuir, 1997. **13**(10): p. 2880-2894.
126. Fowkes, F.M., *ATTRACTIVE FORCES AT INTERFACES.* Industrial & Engineering Chemistry, 1964. **56**(12): p. 40-52.
127. Owens, D.K. and R.C. Wendt, *Estimation of the surface free energy of polymers.* Journal of Applied Polymer Science, 1969. **13**(8): p. 1741-1747.
128. Wenzel, R.N., *RESISTANCE OF SOLID SURFACES TO WETTING BY WATER.* Industrial & Engineering Chemistry, 1936. **28**(8): p. 988-994.
129. Cassie, A.B.D. and S. Baxter, *Wettability of porous surfaces.* Transactions of the Faraday Society, 1944. **40**(0): p. 546-551.
130. Mironov, V., *Fundamentals of Scanning Probe Microscopy*. 2014.
131. Oswald, S., *X-Ray Photoelectron Spectroscopy in Analysis of Surfaces Update based on the original article by Steffen Oswald, Encyclopedia of Analytical Chemistry, © 2000, John Wiley & Sons, Ltd.* Encyclopedia of Analytical Chemistry, 2013.
132. Yoshinobu, J., *Infrared Reflection–Absorption Spectroscopy*, in *Compendium of Surface and Interface Analysis*, J. The Surface Science Society of, Editor. 2018, Springer Singapore: Singapore. p. 295-299.
133. Anderson, T.L. and T.L. Anderson, *Fracture Mechanics: Fundamentals and Applications, Third Edition*. 2005: Taylor & Francis.
134. Hirn, U. and R. Schennach, *Fiber-Fiber Bond Formation and Failure: Mechanisms and Analytical Techniques*. 2017.
135. Awaja, F., et al., *Adhesion of polymers.* Progress in Polymer Science, 2009. **34**(9): p. 948-968.
136. Kumar, B., et al., *Tetrahydropyranyl ether (THPE) formation in hydroxyl group protection and conversion to other useful functionalities.* RSC Adv., 2014. **4**(40): p. 21121-21130.
137. Klaikherd, A., C. Nagamani, and S. Thayumanavan, *Multi-Stimuli Sensitive Amphiphilic Block Copolymer Assemblies.* Journal of the American Chemical Society, 2009. **131**(13): p. 4830-4838.
138. Yildirim, T., et al., *Dual pH and ultrasound responsive nanoparticles with pH triggered surface charge-conversional properties.* Polym. Chem., 2017. **8**(8): p. 1328-1340.
139. Yildirim, T., et al., *Polymersomes with Endosomal pH-Induced Vesicle-to-Micelle Morphology Transition and a Potential Application for Controlled Doxorubicin Delivery.* Biomacromolecules, 2017. **18**(10): p. 3280-3290.
140. Miyashita, M., A. Yoshikoshi, and P.A. Grieco, *Pyridinium p-toluenesulfonate. A mild and efficient catalyst for the tetrahydropyranylation of alcohols.* The Journal of Organic Chemistry, 1977. **42**(23): p. 3772-3774.
141. Çaykara, T., et al., *Thermal behavior of poly(2-hydroxyethyl methacrylate-maleic acid) networks.* Polymer Degradation and Stability, 2003. **80**(2): p. 339-343.
142. Ji, X.L., et al., *Structure and properties of hybrid poly(2-hydroxyethyl methacrylate)/SiO2 monoliths.* Journal of Applied Polymer Science, 2003. **88**(14): p. 3168-3175.
143. Huang, S.-L., W.-K. Chin, and W.P. Yang, *Structural characteristics and properties of silica/poly(2-hydroxyethyl methacrylate) (PHEMA) nanocomposites prepared by mixing colloidal silica or tetraethyloxysilane (TEOS) with PHEMA.* Polymer, 2005. **46**(6): p. 1865-1877.
144. Feldermann, A., et al., *Reversible addition fragmentation chain transfer copolymerization: influence of the RAFT process on the copolymer composition.* Polymer, 2004. **45**(12): p. 3997-4007.
145. Favier, A., et al., *Synthesis of N-acryloxysuccinimide copolymers by RAFT polymerization, as reactive building blocks with full control of composition and molecular weights.* Polymer, 2004. **45**(23): p. 7821-7830.
146. Luo, Q., et al., *Facile synthesis of well-defined pH-liable Schiff-base-type photosensitive polymers via visible-light-activated ambient temperature RAFT*

polymerization. Journal of Polymer Science Part A: Polymer Chemistry, 2009. **47**(23): p. 6668-6681.
147. Duemichen, E., et al., *Analyzing the network formation and curing kinetics of epoxy resins by in situ near-infrared measurements with variable heating rates.* Thermochimica Acta, 2015. **616**: p. 49-60.
148. Erdmann, M., et al., *Cure conversion of structural epoxies by cure state analysis and in situ cure kinetics using nondestructive NIR spectroscopy.* Thermochimica Acta, 2017. **650**: p. 8-17.
149. Gutowski, W.S., *Interface/Interphase engineering of polymers for adhesion enhancement: Part I. Review of micromechanical aspects of polymer interface reinforcement through surface grafted molecular brushes.* The Journal of Adhesion, 2010. **79**(5): p. 445-482.
150. Gutowski, W.S., et al., *Interface/interphase engineering of polymers for adhesion enhancement: Part II. Theoretical and technological aspects of surface-engineered interphase-interface systems for adhesion enhancement.* The Journal of Adhesion, 2010. **79**(5): p. 483-519.
151. Henn, G., et al., *Chain End Effects and Dewetting in Thin Polymer Films.* Macromolecules, 1996. **29**(12): p. 4305-4313.
152. Liu, Y., et al., *Synthesis of High-Density Grafted Polymer Layers with Thickness and Grafting Density Gradients.* Langmuir, 2005. **21**(25): p. 11806-11813.
153. Corey, E.J., H. Niwa, and J. Knolle, *Total synthesis of (S)-12-hydroxy-5,8,14-cis,-10-trans-eicosatetraenoic acid (Samuelsson's HETE).* Journal of the American Chemical Society, 1978. **100**(6): p. 1942-1943.
154. Corey, E.J., et al., *Stereospecific total synthesis of gibberellic acid. A key tricyclic intermediate.* Journal of the American Chemical Society, 1978. **100**(25): p. 8031-8034.

9 Curriculum Vitae

For reasons of data protection, the curriculum vitae is not published in the electronic version.